

## **Ph.D. THESIS**

# **The mechanism of ultra-short (femtosecond) and nanosecond laser ablation of biological tissue: mass spectrometry of ionic and neutral species.**

Realized to obtain the title of Ph. D. in Technical Science under the supervision of

a. o. Prof. Dr. W. Husinsky

Institut für Allgemeine Physik

E 134

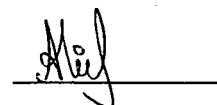
Submitted at the Technical University Vienna  
Technical and Natural Science Faculty

By

Mag. Albena Daskalova  
9727145

Donaufelderstrasse /54  
1210 Wien, Austria

Vienna, 01.10.2003



# **DISSERTATION**

## **The mechanism of ultra-short (femtosecond) and nanosecond laser ablation of biological tissue: mass spectrometry of ionic and neutral species.**

Ausgeführt zum Zwecke der Erlangung des akademischen Grades eines  
Doktors der technischen Wissenschaften unter der Leitung  
von

a. o. Prof. Dr. W. Husinsky

Institut für Allgemeine Physik

Inst. Nr. 134

eingereicht an der Technischen Universität Wien  
Technisch – Naturwissenschaftliche Fakultät

Von

Mag. Albena Daskalova  
9727145

Donaufelderstrasse /54  
1210 Wien, Österreich

Wien, am 01.10.2003

---

## *Abstract*

In the intensity range  $10^{12} W/cm^2 - 10^{14} W/cm^2$  a very wide field of application of femtosecond lasers is the precision microstructuring ranging from metals, dielectrics to biological tissues. The overall goal of this research was to gain a deeper understanding of the processes involved in laser ablation of hard biological tissue material with ultra-short femtosecond laser radiation. An investigation into the mechanism of laser ablation of biological tissue is a complicated problem due to the complexity of the examined organic material. Furthermore, the pulse characteristics of the ultrashort lasers place it in a unique temporal regime. The combination of pulse duration of  $\approx 30fs$  and peak intensity of  $10^{15} W/cm^2$  presents the possibility of producing interactions with minimal ablation damage. Based on the acquired knowledge, the appropriate experimental parameters will be found.

The resulting processes arisen due to the interaction of ultrashort femtosecond laser pulses with tooth and bone samples are analyzed with Laser Ablation-Time of flight-Mass Spectrometry. A complete set of measurements were performed in order to investigate in details the ablation mechanism. More specific the mass spectra of ablated neutral and ion particles from organic matter were studied.

A more detailed view was taken by investigating the ablation dynamics at several wavelengths. The precise examination of the mass spectra of laser ablation with  $193nm$  and  $800nm$  introduces the way of altering the chemical composition of the ablated tissue. No molecular ions were observed for any of the biological targets for both wavelengths. The results indicate that the peptide bond is the main target in the molecule of collagen. It was suggested that the fragmentation pathway for the amino acid molecules is initiated by  $\alpha$ -cleavage reaction which results in formation of decarboxylated ion.

The fluence dependence, for ablation with ultra-short and nanosecond laser pulses, was obtained and was determined very precisely the ablation threshold for organic material.

In general, it was found that ablation with ultra-short (femtosecond) pulses at  $800nm$  radiation yields the highest number of characteristic ions. The results also show the molecule dependent optimum intensity of laser ablation required to produce the highest yield of characteristic ions.

The high peak powers which are typical for the femtosecond pulses, give rise to ionization pathways distinct from resonant excitation processes. From the analysis of the post-ionization mass spectra the coupling mechanism between the intense laser pulse and the molecules can be deduced. The ionization mechanism of molecular species interacting with intense laser pulses was examined in order to gain more inside into the fragmentation pathways. We suggested that the mechanism of coupling between the intense IR radiation field and molecule can be explained with the Keldysh theory, which

gives the qualitative criterion (the Keldysh parameter) for field ionization. It has been successfully applied to atoms and molecules.

At high intensities in the photoionization mass spectra at  $800nm$  doubly charged species were obtained which indicate the onset of considerable Coulomb repulsion. This results in explosion of the atom (molecule) and formation of stable ions. It was demonstrated that multiply charged species were produced for ionization laser intensities approaching  $10^{14} W/cm^2$ .

## **ZUSAMMENFASSUNG**

Die meist verbreitete Anwendung von Femtosekundenlaser im Intensitätsbereich von  $10^{12} \text{ W/cm}^2$  -  $10^{14} \text{ W/cm}^2$  ist die präzise Mikrostrukturierung von Metallen, Nichtleitern und biologischen Geweben. Das Hauptziel war, die Prozesse der Laserablation von biologischen Geweben durch die Strahlung eines Femtosekundenlaser, eingehend zu untersuchen. Die Untersuchung des Mechanismus von Laserablation biologischer Gewebe stellt wegen der Komplexität des untersuchten biologischen Stoffs eine komplizierte Aufgabe dar. Die Kombination einer Impulsdauer von ca.  $30 \text{ fs}$  und einer Spitzenintensität in Höhe von  $10^{15} \text{ W/cm}^2$  ermöglicht eine Wechselwirkung bei minimalen Schaden durch die Ablation.

Die Prozesse, die infolge der Wechselwirkung von Femtosekundenlaserimpulsen und Zahn- und Knochen material entstehen, werden mit Laserablations-Flugzeit Massenspektrometer analysiert. Ein vollständiger Vermessungssatz wurde ausgeführt, um den Ablationsmechanismus ausführlich zu untersuchen. Es wurden besonders die Massenspektren von ablatierten neutralen und geladen Teilchen organischer Stoffe detektiert

Die Dynamik der Ablationsprozesse wurde im Detail für mehrere Wellenlängen der Laserstrahlung untersucht. Die präzise Untersuchung der Massenspektren der Laserablation mit  $193 \text{ nm}$  und  $800 \text{ nm}$  leitet ein Verfahren zur Änderung der chemischen Zusammensetzung des ablatierten Gewebes ein. Bei keinem von den biologischen Objekten wurden Molekülionen für die beiden Wellenlängen festgestellt.

Die Ergebnisse zeigen, dass im Kollagenmolekül das Ziel die Peptidbindung ist. Es wurde angenommen, dass der Fragmentationsweg von den Molekülen der Aminosäure durch die  $\alpha$ -Spaltungsreaktion eingeleitet wird, die die Entstehung eines dekarboxylierten Ions zur Folge hat.

Es wurde die Abhängigkeit des Flusses für die Ablation mit Ultrakurz- und Nanosekundenlaserimpulsen erforscht und es wurde die Ablationsschwelle für organische Stoffe bestimmt.

Generell wurde festgestellt, dass die Ablation mit Ultrakurzimpulsen (Femtosekundenimpulsen) bei Strahlungen mit einer Wellenlänge von  $800 \text{ nm}$  die größte Menge von charakteristischen Ionen liefert. Die Ergebnisse zeigen auch die von den Molekülen abhängigen optimale Intensität der Laserablation, die für den größte Ausbeute von charakteristischen Ionen erforderlich ist. Die hohen Spitzenleistungen, die für Femtosekundenimpulse typisch sind verursachen Ionisierungswege, die sich von deren gewöhnliche Resonanzanregung unterscheiden. Von der Analyse der Post-Ionisierungsmassenspektren kann der Kopplungsmechanismus zwischen den intensiven Laserimpulsen und den Molekülen hergeleitet werden. Es wurde der Mechanismus für die Ionisierung von Molekülspezies, die mit den intensiven Laserimpulsen in Wechselwirkung stehen, untersucht, um eine genaue Information über die Fragmentation

zu bekommen. Wir nehmen an, dass der Kopplungsmechanismus zwischen der intensiven Infrarotstrahlung und den Molekülen mit der Theorie von Keldysh beschrieben kan, die das Kriterium (Keldysh Parameter) für das Ionisierungsfeld bestimmt, dem die Atome und Moleküle unterworfen sind.

Bei hohen Intensitäten wurden in der Photoionisierungsmassspektra bei  $800\text{nm}$  doppelt geladene Spezies gebildet, die wesentlichen Coulomb-Abstossenkräften unterworfen sind. Das führt zur Explosion des Atoms (des Moleküls) und Entstehung von stabilen Atomen. Es wurde gezeigt, dass bei Intensitäten von der Grösse bis  $10^{14} \text{ W/cm}^2$ , mehrfach geladene Teilchen gebildet wurden.

## *Contents*

Chapter 1	7
1. Introduction	7
1.1 Laserablation	9
1.1.1 UV laser ablation	10
1.1.2 UV laser ablation of polymers	11
1.1.3 Medical application of UV laser ablation	12
1.2 Mechanism of Laser-Tissue interaction	14
1.3 The properties of ultra-short laser matter-interaction	17
1.4 Electronic transitions in molecules	19
1.4.1 High intensity field interactions with molecular systems	20
1.4.2 Ablation of metals and dielectrics	23
1.4.3 Ionization mechanism of dielectrics	25
Chapter 2	27
2. Experimental setup	27
2.1 Timing of the experiment	30
2.2 The TOF mass spectrometer	32
2.3 Ultra-short pulse generation	34
2.3.1 Specification of the experimental laser system	36
2.3.2 Pulse width measurements	40
2.3.3 The excimer laser	49
2.4 The SNMS method	51

Chapter 3	52
3. Results and discussion	52
3.1 Optical properties of biological tissue	53
3.1.1 Composition of biological samples	54
3.2 Ultra-short laser ablation mass spectra	60
3.2.1 Laser ablation mass spectra at 193nm	68
3.2.2 SIMS mass spectra	72
3.3 Laser intensity dependence measurements	75
3.4 SNMS measurements	82
Summary	93
Abbreviations	94
Bibliography	95
Acknowledgements	100
Curriculum vitae	101



# Chapter 1

## 1. Introduction

Since invention of the first ruby laser in 1960 by Maiman the advance of laser technology has lead to a new class of lasers capable of generating light pulses in the order of a few femtoseconds ( $1\text{fs} = 1 \cdot 10^{-15}\text{s}$ ) pulse duration and intensities of  $10^{12} - 10^{16}\text{W/cm}^2$ . The development of ultra-short lasers discovers new areas of applications of high-intensity laser radiation: femtochemistry, nonlinear imaging, nanotechnology, microsurgery, laser ablation.

In the last 10-15 years *Laser Ablation* became very popular for the analysis of solid samples. The study of Laser-matter interaction processes, in different time scales – nano, pico, femto, and their application in different fields, developed a thorough knowledge of the fundamental laws involved in this process.

During the last years it was found that the use of picosecond and femtosecond laser pulses for laser ablation, provide distinct advantages over laser pulses with longer durations mainly due to their efficient, fast and localized energy deposition; low deformation and ablation thresholds, large ionization efficiencies, small fragmentation and minimal thermal and mechanical damage. In comparison with longer pulses the interaction of femtosecond pulses with the matter result in minimized heat-affected zones. Another advantage of ultra short laser pulses which favor their use is the high achievable control over the ablation depth. Knowing these advantages, first attempts were performed to concentrate the attention to the investigation of laser radiation interaction with organic Biological systems. Knowledge of this has been gained so far with the examination of ionization and fragmentation dynamics of laser ablated species. In particular successive femtosecond photoionization experiments have been already performed on aliphatic and aromatic amino acids [vorsa99], dipeptides [sun, lock99]; large organic molecules, cyclic aromatic hydrocarbons [dewitt95], polycyclic aromatic hydrocarbons [robs02],  $(\text{H}_2\text{O})_n$  and  $(\text{D}_2\text{O})_n$  [radi99] etc.

Recently *Laser ablation* is being used in a large variety of applications in medicine (dentistry, surgery, neurosurgery and ophthalmology), science (material processing, micromachining, thin film deposition). Successive femtosecond ablation experiments have been performed on hard and soft tissue with precise and minimal invasive structuring, more controlled material removal, less collateral damage. The application of femtosecond lasers in dentistry has reached an advanced state due to absence of pain, mechanical stress, absence of thermal side effect in the surrounding areas. In contrast the state of the art of conventional methods like drilling machines, Er:Yag ablation, is every time accompanied with generation of shock waves and micro cracks in the enamel of the tooth which leads to the development of new caries. More recent studies have proved the

potential of ultra-short lasers for applications in cornea shaping and ear surgery. Not direct application of femtosecond pulses in medicine was found in the structuring of medical implants (stents), which are used to replace blocked by the plaque arteries, so called bypass operation. The stents can be structured from stainless steel but also from resorbable, biological material (*Figure 1*).

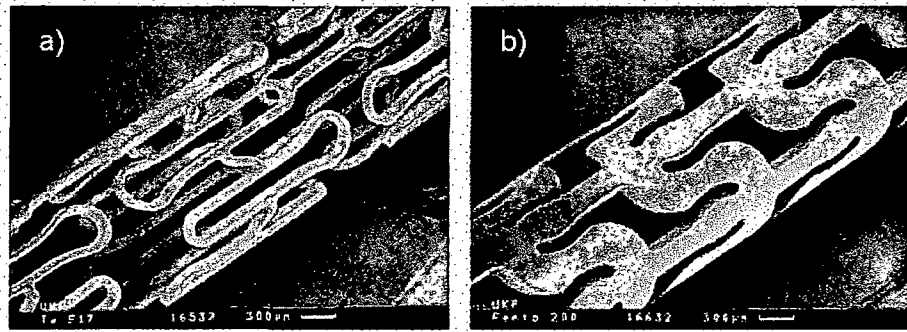


**Figure 1:** Femtosecond machining of high quality stents: a) metals, b) biologic material [from korte99].

The latest examination in the subject of ultra-short laser-matter interaction reveals that almost every material can be processed and structured successfully with a degree of very high-precision (submicrometer structures). For example when ultrashort laser pulses are tightly focused into the bulk of a transparent glass or crystal, optical waveguides can be fabricated. The laser energy is deposited inside the material, leading to permanent refractive index modifications inside a small focal volume (*Figure 2*).

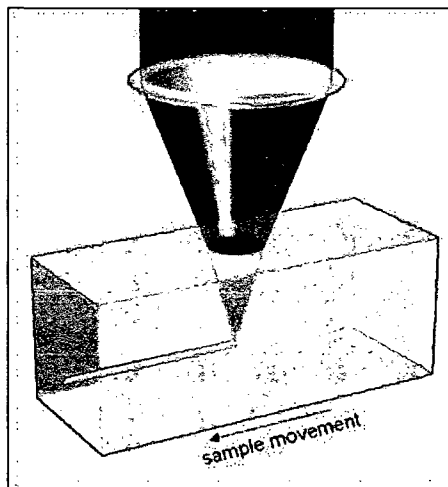


**Figure 2:** Fabrication of three-dimensional photonic structures in transparent materials [from korte00].

The potential of using ultra-short pulses to make very clear and sharp structures in metals (for example Au, Ag, Cu, stainless steel) has obtained considerable attention. For example one can produce sub-diffraction limited holes in thin metal films. Deep drilling of holes in metals by ultra-short laser pulses can be achieved with minimal damage and high order of reproducibility (*Figure 3*).

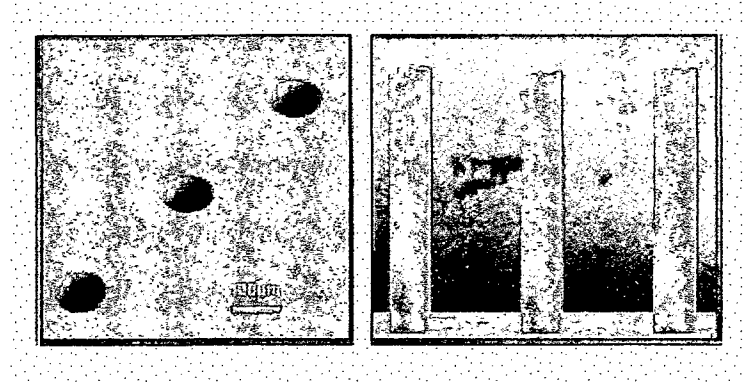


**Figure 3:** SEM pictures of holes drilled by femtosecond pulses in stainless steel plate [from osten03].

A reliable knowledge has been gained about the physics of the interaction process of ultra-short laser pulses with metals, dielectrics, polymers. For making possible a precise examination of the *Laser ablation* process *Laser post-ionization* method combined with *TOF* (time-of-flight) mass spectroscopy has proven to be a very sensitive technique for surface analysis. This technique allows detection and trace analysis of atoms and molecules ablated from the material. After post-ionization the particles are detected and mass separated with *TOF* mass spectrometer. It is believed that the high intensity ultra-short laser pulses are able to ionize any class of molecule reducing the probability of fragmentation. This statement will be one of the goals of the current thesis.

## 1.1 Laser Ablation

The definition of *Laser ablation* can be formulated as *removal of macroscopic amounts of matter from the surface of the material* [linde99]. The parameters which are of great importance to the ablation process are the *wavelength*, the *pulse duration* and the *intensity* of the laser.

As a basic understanding of the process of Laser ablation it is postulated that the laser pulse interacts first with the electronic state of valence of the examined system. After redistribution of the energy in the system, the process continues with (depending on the

pulse duration) bond breaking, material expansion, generation of plasma. The necessary time for the relaxation of the energy in the system is called *relaxation time*. Another important constant is also the time necessary for carrying away the ablated material – *ablation time*, it is defined by the velocity of the mass transport.

An important parameter in laser ablation is the *ablation threshold*, which can be formulated as the minimum applied energy fluence required initiating the removal of the material. Depending of the material structure and properties the ablation threshold varies from material to material. It depends mainly on ionization potential of the examined material, pulse duration and the wavelength.

The term *ablation efficiency* is the ratio of the ablated matter volume to laser pulse energy. Knowing these parameters and varying them in a regulated mode, very precise and detailed examination of the ablation process can be performed at various photons wavelengths.

### 1.1.1 UV laser ablation

Surface ablation with laser pulses in the UV nanosecond time scale, was an important subject of examination for the scientists, since it was discovered the convenience of utilizing the UV laser light in many applications in the medicine and in the material processing.

Thus it was found that the mechanism of interaction of the UV photons with different materials is governed by different laws depending on the material: metals, semiconductors, organic and inorganic compounds. As a basic understanding the interaction of photons with solids induces electronic transitions from the bulk valence band, from occupied surface and defect states, and from free conduction band states *Figure 4*.

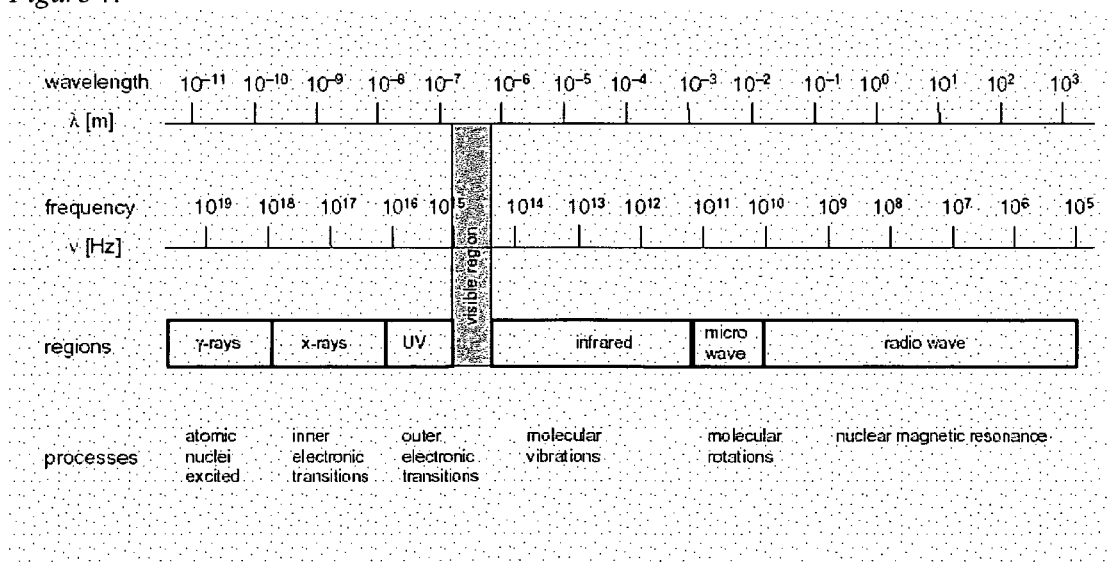


*Figure 4: The electromagnetic spectrum.*

## 1.1.2 UV laser ablation of Polymers

Due to the rising applications of polymers in microelectronics, in thin film deposition, and the fast development of laser systems, it was established a necessity of performing an investigations to give a real model for interaction of the UV laser light with the organic polymers.

The interaction of UV photons with polymers was studied by means of:

- Photoionization time of flight mass spectroscopy
- Laser-induced polymerization
- Laser-induced surface modification (in the thin film formation)

Experiments on ablating polymers were performed by various groups, for different types of polymers. Polymers with strong, moderate and weak absorption were mainly examined, in the range of  $193\text{nm}$  (ArF),  $248\text{nm}$  (KrF),  $308\text{nm}$  (XeCl),  $351\text{nm}$  (XeF).

The nature of the interaction is believed to be predominantly Photochemical. It is stated that the photochemical process exists when the UV photon has an energy which covers the bond energy of the polymer material and is resulting in bond breaking (due to electronic excitation). The Photothermal process coexists and produces temperature rise in the material - the bonds are thermally broken.

In addition in the case of photochemical process it was observed a development of shockwave followed by surface swelling. In the thermal regime the shock wave is not distinct.

It is as well observed that the interaction of the UV photons with the polymers is causing etching of the surface to a depth of  $0.1\mu\text{m}$ .

It was suggested the etched depth per pulse to be written as:

$$I_{f,\text{total}} = I_{f,\text{photo}} + I_{f,\text{thermal}} \quad (\text{Equation 1})$$

$I_{f,\text{photo}}$  - photochemical ablation

$I_{f,\text{thermal}}$  - photothermal ablation

The observation of thermal processes at low fluences is negligible; increasing the fluence it reaches a limiting value and triggers the photochemical reaction.

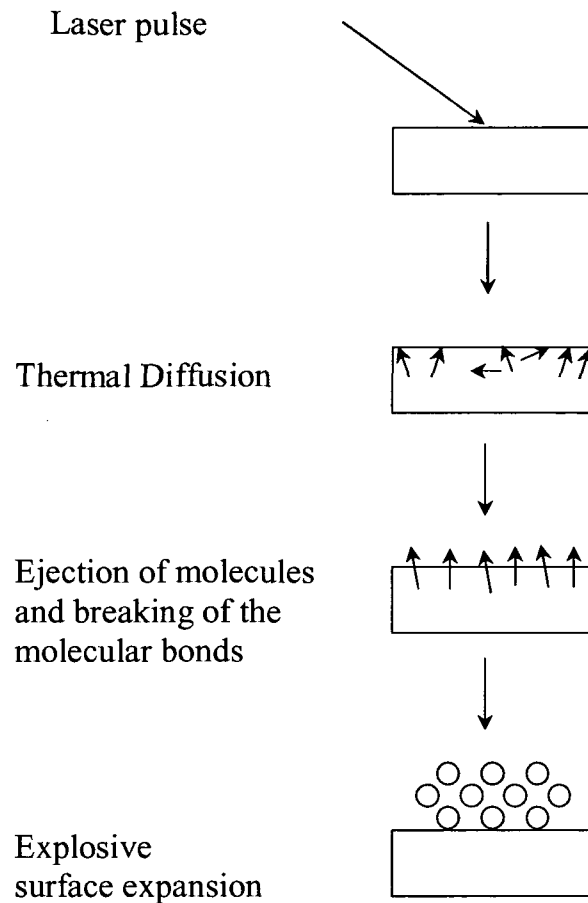


*Figure 5: Block diagram of the model of UV laser ablation.*

### 1.1.3 Medical Application of UV ablation

The advantages of the application of excimer lasers in medicine are numerous. In particular successful application has been established in corneal surgery.

A widespread method is *Photorefractive keratectomy (PRK)*. *PRK* was the first surgical procedure developed to reshape the cornea (*Figure 6*) in order to modify its refracting index. As a result the cornea surface is flattened by ablation with excimer laser. Ablating with  $193\text{nm}$  and photon energy of  $6.4\text{eV}$  the absorption by the corneal tissue is high and the process results in breaking of the protein bonds (binding energy of the protein bonds  $\approx 3.5\text{eV}$ ). Thus is assured very rapid ejection of the fragments and not a trace of damaged underlying tissue. The conclusion is that this type of method has proven to be very successful and it is effectively used to treat myopia (near sightedness), hyperopia

(farsightedness), and astigmatism (an uneven curvature of the cornea). The complications after the treatment are mostly negligible.

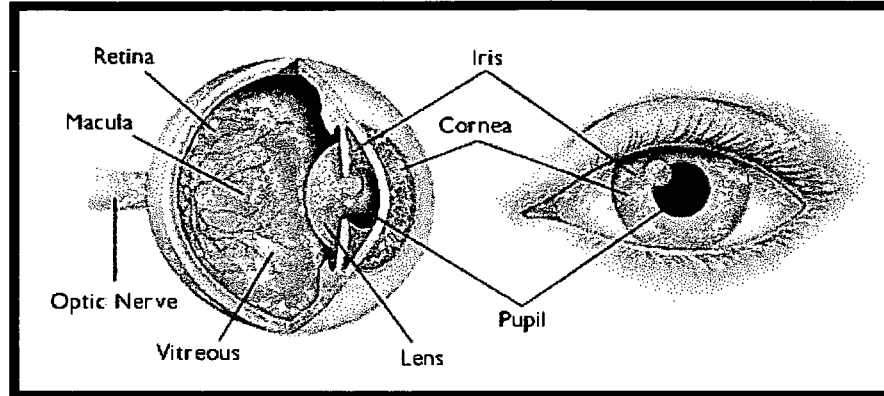


*Figure 6: Structure of the human eye.*

Another procedure, called *LASIK*- in-situ keratomileusis, was developed. The method represents the following: first lifting of a thin layer of the cornea connected at one side only and after that for 1 minute treatment of the eye with the laser. In *PRK*, the top layer of the cornea, called the epithelium, is scraped away to expose the stromal layer (the middle layer of the cornea) underneath. In *LASIK* (Figure 7) a flap is cut in the stromal layer and the flap is folded back.

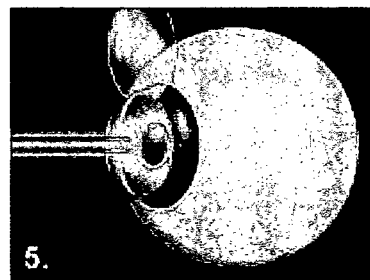


*Figure 7: Principle of the LASIK method.*

Another aspect in which the excimer laser is used is the treatment of Glaucoma. The procedure is called *Excimer Laser Trabeculotomy (ELT)*. The laser beam opens the fluid channels of the eye, helping the drainage system to work better. The laser light is

transmitted through a tiny needle to the trabecular meshwork. This method has proved its effectiveness by reducing the intraocular pressure significantly and with its minimal invasion.

The excimer laser is also used in dermatology for treatment of a variety of dermatologic diseases like psoriasis (red, scaly skin plaques), vitiligo and leukoderma as well. The 308nm XeCl excimer laser therapy has proved its success to treat the symptoms of psoriasis.

The procedure called *ELANA (Excimer Laser Assisted Nonocclusive Anastomosis)* enables the creation of a bypass in a major cerebral vessel without occluding the recipient vessel. The meaning of a bypass is that the blood vessels are joined artificially.

## 1.2 Mechanisms of Laser - Tissue interaction

The interaction mechanism of laser radiation with biological material is dependent from the specific characteristics of the tissue and from the laser parameters (wavelength, exposure time, applied energy, focal spot size, and power density).

The classification of the different types of laser interactions can be summarized as follows:

- *Photochemical interaction*: results when the light is absorbed by molecules present or added to the tissue
- *Thermal interactions*: it is an effect of deposition of energy into the tissue. They are characterized with increase in local temperature.
- *Photoablation*: it is described as photo-dissociation process of the molecular bonds of the tissue.
- *Plasma-induced ablation*: arises when applying very high power densities more than  $10^{11} \text{W/cm}^2$ . Ablation due to ionizing plasma formation.
- *Mechanical*: usually is associated with high laser fluence rates. Occur breakdown of the tissue, formation of plasma and generation of shock wave.

A typical example of *photochemical interaction* is the *Photodynamic therapy (PDT)*. It is based on injection of spectrally adapted chromophores (photosensitizer) into the body. After irradiation with monochromatic light (a wavelength is used which is well absorbed by the drug) the photochemical reaction is triggered. The photosensitizer performs several simultaneous decays, which result in intramolecular transfer reaction. After being excited by absorption of photon, the drug returns to its ground state and transfers energy to ambient oxygen, which is transformed to singlet oxygen. The singlet oxygen is very



toxic substance and oxidizes all the tissue constituents. This method is used mainly for treating cancer cells.

Another type of photochemical interaction is *biostimulation*. It takes place at very low laser powers ( $1-5\text{mW}$ ).

The *thermal interactions* results from conversion of light to heat. It is very important to be stated, that the deposition of laser energy depends from the wavelength, power density, spot size, exposure time, repetition rate and also from the optical and thermal tissue properties, such as absorption, scattering coefficients; heat capacity, thermal conductivity.

For thermal decomposition of tissue it is necessary to adjust the duration of the laser pulse in order to minimize thermal damage to surrounding tissue. For this reason thermal relaxation time is defined, which measures thermal susceptibility of the tissue.

Case 1:

$\tau < 1\mu\text{s}$  For nano- and picosecond pulses heat diffusion during the laser pulse is negligible

Case 2:

$\tau > 1\mu\text{s}$  Thermally damaged zone is broader.

At microscopic level, thermal effects can be outlined as a two step process:

Absorption:  $A + h\nu \rightarrow A^*$

Deactivation:  $A^* + M(E_{kin}) \rightarrow A + M(E_{kin} + \Delta E_{kin})$

Depending on the degree and duration of the heating of the tissue can be distinguished several phases.

Coagulation – usually coagulated tissue appears darker than the other tissue, and during this process the temperatures reach  $60^\circ\text{C}$ .

Vaporization – leads to increase in pressure, water tries to expand in volume as it vaporizes and thus leads to microexplosions. The result is thermal decomposition.

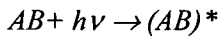
Carbonization – effect of carbonization of tissue, due to drastically increase in the temperature. At temperatures above  $150^\circ\text{C}$  the tissue starts to carbonize (carbon is released) leading in blackening in color. This reduces the visibility during surgery.

Melting – it is characterized with a significant increase in the temperature (few hundred degrees Celsius).

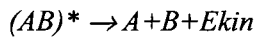
The *photoablative effect* can be described as an ablation of the material without thermal lesions. Because of the dissociation, the molecular bonds are broken and the tissue components are vaporized without heat generation. This effect is associated with lasers operating in the UV range (ArF, KrF, XeCL). The energy of single UV photon is enough for dissociation of the former bound molecule. The decomposing of the material happens when exposing to high intense laser irradiation ( $10^7 - 10^8 \text{ W/cm}^2$ ) in the nanosecond range pulse duration.

The photoablation is a two step process:

Step 1: Excitation



Step 2: Dissociation



To trigger the photoablation it is necessary to apply certain threshold intensity. Above this threshold a well defined depth is ablated.

It is very important to draw attention at the difference between photoablation and ablative photodecomposition. In the case of photoablation the energy of single UV photon is enough for dissociation of the former bound molecule AB, however in thermal interaction the photon energy is not high enough for the molecule to reach a repulsive state, it is promoted only to a vibrational state within the ground level, the absorbed energy then dissipates to heat and the molecule returns to its ground state.

*Plasma-induced ablation* proceeds with well defined removal of the tissue, without thermal or mechanical damage. The characteristic parameter for plasma-induced ablation is the local electric field  $E$ .

$$I(r, z, t) = \frac{1}{2} \epsilon_0 c E^2 \quad (\text{Equation 2})$$

If  $E$  exceeds a certain threshold (the applied electric field forces the ionization of molecules and atoms) than the breakdown occurs. It is established that Q-switch and mode-locked pulses in pico- and femtosecond time domain could initiate localized microplasma. The difference is in the mechanism of generation of free electrons. By the Q-switched pulses it is a *thermoionic emission*, but in the case of mode-locked pulses is *multi-photon ionization* (several photons provide the energy for ionization).

The *Mechanical effect* leads to fragmentation and cutting of tissue by mechanical forces (cavitation, jet formation and e.t.c). These effects take place at different time scale. Photodisruption starts with optical breakdown. Shock wave generation starts during the expansion of plasma then it propagates into adjacent tissue and leaves the focal volume.

Cavitation starts 50-150ns after the laser pulse and occurs when focusing the laser beam into the tissue. Cavitation bubbles content is a gaseous vapor, like water vapors and carbon oxides.

<i>Types of lasers</i>	<i>Applications</i>
<i>Ion lasers: Ar, Kr</i>	<i>Photocoagulation, dermatology, retinal detachment, laser-induced thermotherapy</i>
<i>CO laser (10.6μm)</i>	<i>Dermatology, neurosurgery, dentistry, retinal detachment, laser-induced thermotherapy</i>
<i>HeNe laser (633nm)</i>	<i>Biostimulation</i>
<i>Diode laser (850nm)</i>	<i>Biostimulation, PDT, retinal detachment, laser-induced thermotherapy</i>
<i>Solid state laser-Nd:Yag (532nm, 355nm), Nd:Ylf Ti:S</i>	<i>Surgery, urology, retinal detachment, laser-induced thermotherapy, refractive corneal surgery, caries therapy, lens fragmentation, lithotripsy</i>
<i>Excimer laser UV</i>	<i>Radial keratotomy, refractive corneal surgery</i>
<i>Dye laser (400-1000nm)</i>	<i>PDT</i>

*Table 1: Different types of lasers and their medical applications.*

### 1.3 The properties of ultra-short laser-matter interaction

In the previous sections it was briefly pointed on the importance of choosing the pulse duration when is concerning the laser-matter interaction. Although that the character of interaction of nanosecond laser pulses was discovered to suite a big variety of applications, still exists some materials (metals) for which precise microstructuring is asking for very delicate material processing. Thus in the recent years the subject of examination of laser-matter interaction was devoted to pulses in the femtosecond time scale.

Generally summarized the most important features of the femtosecond interaction overcoming the nanosecond and picosecond interaction are:

- *reduced ablation thresholds*
- *negligible heat diffusion into the material*
- *minimized energy loss*
- *minimized heat affected zones*
- *almost absent mechanical damage*
- *absence of molten zones*
- *absence of liquid phase*
- *reduced molecular fragmentation*

The thermal side-effect is reduced when the sample is ablated with lasers operating in the fs time scale. At this point it is necessary to be emphasized on the thermal component of the interaction process, in the sense of making a distinction between ablation in the femtosecond and ablation in the nano/microsecond regime.

As the pulse duration gets shorter than the thermal diffusion time, there will be not enough time during the pulse for heat conduction to occur. Because of the short pulse duration higher intensities can be reached, in the case of femtosecond interaction, and the ultrashort pulse will cause much lower heat load in to the sample. The laser pulse terminates before the energy is completely distributed in the matter, so the energy is deposited without laser-plasma interaction. The thermal side-effects are restricted to the penetration depth of the laser pulse.

In contrast to the femtosecond pulse ablation, the ablation with nanosecond pulses and longer pulses results in relatively slow heat flow. CW lasers and pulsed lasers working in the microsecond range show very strong thermal side – effects, they generate too much heat during the ablation process.

Another advantage of ultrashort laser pulses which favor their use is the high achievable control over the ablation depth.

The comparison of different investigations of laser ablation process of metals with nano-, pico- and femtosecond pulses definitely indicates a different behavior of the plasma formation mechanism. With femtosecond laser ablation there is no trace of a molten material, with nanosecond pulses there is an evidence of a molten layer formation. This can be explained by the dependence of the process of plasma generation by the ablation regime used.

With nanosecond laser ablation the presence of a liquid phase leads to unstable drilling, there is enough time for the thermal wave to propagate and form a molten layer, in this case target material is removed in vapor and liquid phases. In contrast, with fs laser

pulses there is a rapid formation of vapor and plasma phases and an absence of liquid phase, which contributes to a better control of the drilling process.

The process of plasma formation can be avoided if the laser fluence is kept below the threshold of the plasma generation. The transition from the solid phase to the gas phase occurs stepwise: melting of the solid and evaporation of the liquid, boiling (occurs when the vapor pressure of the liquid phase exceeds the ambient pressure) and finally when the laser radiation is of sufficiently high intensity the ionization process develops and the solid material transforms into plasma.

Ablation is created when the laser fluence is above certain threshold fluence.

## 1.4 Electronic transitions in molecules

The interaction of molecules with intense radiation is focused on the processes of dissociation, ionization, multiple ionization. The action of photon absorption by a molecule is followed by photoionization, in which an electron is expelled from a molecule. The photoionization method is applied for investigation of the structure, composition, and properties of the examined surfaces.

The necessary energy of a photon to change the electron distribution in a molecule is in the order of several electron volts. After the change of the electron distribution different forces will influence the nuclei of the molecule and the molecule will start to vibrate.

According to the *Frank-Condon* principle:

*"The electronic transition is most likely to occur without changes in the position of the nuclei in the molecular entity and its environment. The resulting state is called Franck-Condon state, and the transition involved a vertical transition. The quantum mechanical formulation of this principle is that the intensity of a vibronic transition is proportional to the square of the overlap integral between the vibrational wave functions of the two states that are involved in the transition. "*

The nuclei experience new force field due to the transition of the electron density and start to vibrate. The most intensive vibronic transition occurs when it is made from the ground vibrational state to the upper vibrational state lying exactly above it.

The vibrational excitation is accompanied by rotation.

There exist two cases in which the molecule can decay its excitation:

- radiative decay – the molecule discards its excitation through a photon
- nonradiative decay – the excess energy is transferred to vibration, rotation or translation of the neighboring molecules.

### 1.4.1 High intensity field interactions with molecular systems

Early efforts have been performed on examining of di-, tri-...atomic molecules by means of energetic ion bombardment or nanosecond lasers. This type of experiments gained a considerable success in increasing the overall ion yield. However the rate of fragmentation of the molecular species remains high due to internal conversion and fast dissociation processes.

The main aim of investigation of molecular systems consists in the effort to minimize the decomposition of the molecules and to ionize them successfully. Studies with femtosecond laser pulses have revealed that the dissociation can be avoided. The high peak powers, common for the femtosecond pulses, give rise to ionization paths different from the resonant excitation processes. In high-intensity fields it is believed that the molecular fragmentation occurs due to multiphoton ionization (tunnel and barrier suppression ionization). In 1964, Keldysh proposed that the field ionization can compete with the multiphoton ionization for atoms.

High intensity laser-matter interaction is described by three parameters the Ponderomotive energy, the Keldysh parameter and the Laser strength parameter.

In the case of ionization of polyatomic molecules the ultrashort pulse permits excitation to the ionization state on a time scale which competes with nuclear motion.

The electric field generated by the laser pulse is given by the formula:

$$E_0 = \left( \frac{2I}{\epsilon_0 c} \right)^{\frac{1}{2}} \quad (\text{Equation 3})$$

Where:

$E_0$  - is the electric field strength

$I$  - is the intensity of the laser beam

$\epsilon_0$  - is the permittivity of the free space

$c$  - is the speed of light

Thus the calculation shows that the electric field strength corresponds to  $8.7 \text{ V \AA}^{-1}$  so the laser intensity is sufficient enough to ionize most of the molecules.

A semiquantitative treatment of the problem of ultrahigh intensity ionization regime gives the possibility to identify the ionization mechanism involved in the process. The derivation of the Keldysh parameter can be described as an electron tunneling through a barrier created by the electric field of the laser. It compares the ionization energy with the ponderomotive energy.

The Keldysh adiabaticity parameter is given by:

$$\gamma = \frac{\omega_0}{\omega_t} = \sqrt{\frac{2IPm_e\omega_0^2}{e^2E_0^2}} \quad (\text{Equation 4})$$

Where  $\omega_0$  stands for the laser frequency,  $\omega_t$  is the tunnel frequency,  $IP$  is the ionization potential,  $m_e$  is the electron mass. The ponderomotive energy is described by:

$$U_p = \left( \frac{e^2 E_0^2}{4m\omega^2} \right) (1 + \alpha^2) \quad (\text{Equation 4.1})$$

When the Keldysh parameter  $\gamma \ll 1$ ,  $IP < U_p$ , then the process is in the field ionization regime, the multiphoton ionization governs the process when  $\gamma \gg 1$ ,  $IP > U_p \gg \hbar\nu_0$ . When  $\gamma < 0.5$  it is believed that tunneling ionization occurs. The two mechanisms for coupling high intensity laser field to the atoms are schematically shown on the (Figure 8).

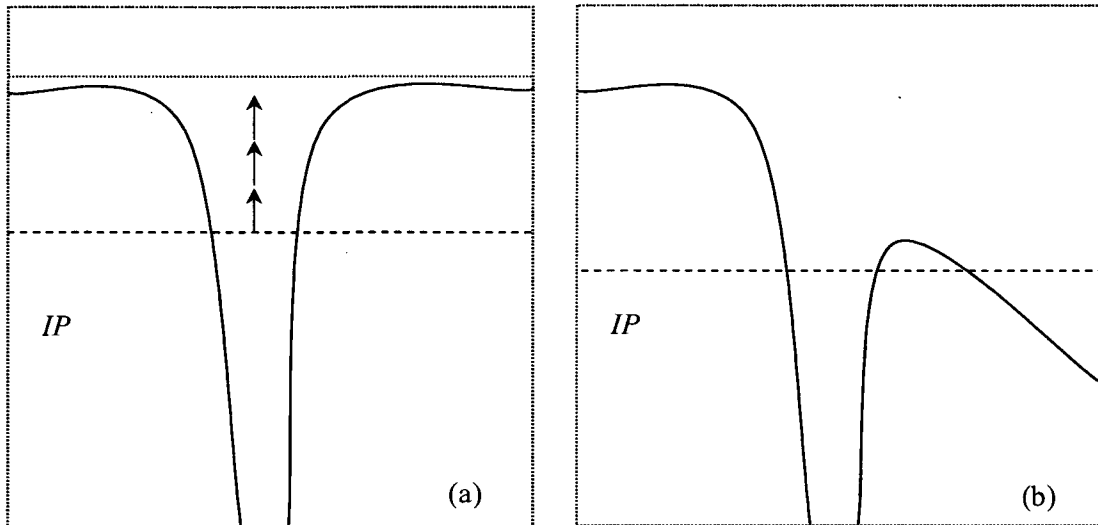


**Figure 8:** Diagrams of interaction of atoms with high intensity laser field: (a)- multiphoton ionization mechanism, (b)-tunnel ionization.

When the Laser electrical field strength reaches the critical value the barrier for ionization is lowered so much that the electron can escape without tunneling this process can be addressed to *barrier suppression ionization (BSI)*. The tunnel ionization and barrier suppression mechanisms were applied for atoms, recently these models were good incorporated for molecular systems as well.

To establish an intact ionization of molecules two regimes can be distinguished. The first regime is the so called -“ladder switching mechanism”- *absorption-dissociation-ionization (ADI)*, for which is valid the schema: dissociation of the molecule and then absorbing of additional photons by the fragments to establish ionization (*Figure 9*). In the case of femtosecond pulses the *ADI* regime is almost suppressed, because the time to undergo substantial nuclear motion in the molecule is very small.

The second type of ionization regime is called -“ladder climbing mechanism”- *absorption-ionization-dissociation (AID)*, the molecule undergoes first ionization and the resulted ion dissociates by absorption of additional photons in a very short time scale.

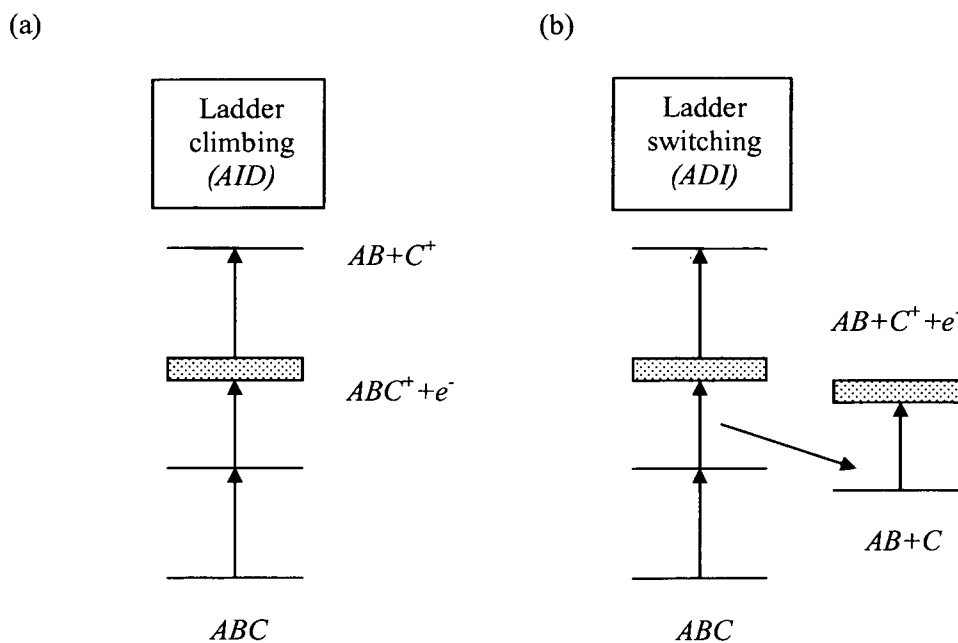


**Figure 9:** Mechanisms of photodissociation: a) AID, b) ADI.



## 1.4.2 Ablation of metals and dielectrics

In this section will be discussed the main features involved in the process of high-intensity ( $10^{16} \text{ W/cm}^2$ ) laser-matter interaction. At intensities ( $10^{13} \text{ W/cm}^2$ - $10^{14} \text{ W/cm}^2$ ) ionization of almost every type of material occurs.

The necessary condition to remove an atom from a solid surface (by means of laser interaction) is to apply a photon energy exceeding the binding energy of that atom. In order to gain more information of the ablation process on the fs time scale the theory of interaction of fs pulses with metals and dielectrics will be outlined.

It is believed that when a femtosecond pulse strikes the surface of a metal the energy, which it is depositing, is absorbed by free electrons. The electrons thermalize in the electron subsystem by electron-electron collisions and form an electron gas. The energy transfer and thermal diffusion to the lattice is created due to electron-phonon coupling. The final phase consists of bond breaking and material expansion (ablation). It was considered that the ablation process itself takes place after the relaxation of the electrons by ultra-short pulse excitation. The theoretical description of the ultra-short laser ablation is expressed below through the energy conservation equations, Newton's law and continuity equation. This model is called two temperature diffusion model.

$$C_e \frac{dT_e}{dt} = -\frac{\partial Q(x)}{\partial x} - \gamma(T_e - T_i) + S - P_e \frac{\partial u}{\partial x}, \quad (\text{Equation 5})$$

$$\text{where } Q(x) = -\frac{k_e(T_e)\partial T_e}{\partial x}, \text{ defines the heat flux.} \quad (\text{Equation 5.1})$$

$k_e$  - electron thermal conductivity

$$\text{The term } S = I(t)A\alpha e^{(-\alpha x)}, \quad \text{defines the laser heat source.} \quad (\text{Equation 5.2})$$

$I(t)$  - laser intensity,  $A$  - surface absorptivity,  $\alpha$  - material absorption coefficient

$$C_i \frac{dT_i}{dt} = \gamma(T_e - T_i) - (P_i + P_e) \frac{\partial u}{\partial x} \quad (\text{Equation 6})$$

$$\rho \frac{du}{dt} = -\frac{\partial}{\partial x}(P_e + P_i + P_c) \quad (\text{Equation 7})$$

$$\frac{\partial \rho}{\partial t} + \frac{\partial \rho u}{\partial x} = 0 \quad (\text{Equation 8})$$

In these equations with  $x$  is defined the direction perpendicular to the surface. The electron and lattice temperatures are assigned with  $T_e$  and  $T_i$ ,  $C_e$  and  $C_i$  are the corresponding heat capacities,  $P_i$  and  $P_e$  are the thermal ion and electron pressures,  $P_c$  is the elastic pressure. The parameter  $\gamma$  defines the electron-lattice coupling,  $\rho$  defines the density of the evaporated material,  $u$  defines the velocity of the evaporated material.

So are described theoretically the spatial and temporal evolution of the electron and lattice temperatures in metals. However in this theoretical model exist some unknowns like the lack of information about the equations of state, which can be desirable for describing of  $P_i$ ,  $P_e$  and  $P_c$ ; the lack of information about electron relaxation rates. Because of this, it will be suitable to neglect material expansion, this approximation helps further for the analysis of ultra-short pulse ablation. Ablation occurs when in (Equation 8),  $P_e$  starts to dominate and exceeds the binding force which can be derived through the gradient of  $P_c$ . When  $P \geq P_{\text{threshold}}$  the atoms overcome the potential barrier and are released completely.

Furthermore three time scales can be distinguished: the electron cooling time ( $\tau_e$ ), the lattice heating time ( $\tau_i$ ) and the duration of the laser pulse ( $\tau_l$ ).

$$\tau_e = \frac{C_e}{\gamma}, \quad \tau_i = \frac{C_i}{\gamma}, \quad \tau_l$$

These times are defining three ablation regimes. When  $\tau_l \leq \tau_e, \tau_i$ , the process develops with precise material processing. In this case the electron-lattice coupling can be neglected. In picosecond ablation regime  $\tau_e \ll \tau_l \ll \tau_i$ . In nanosecond regime  $\tau_l \gg \tau_i$  and the electron and lattice temperature are equal.

Several groups had investigated the ablation of sapphire ( $Al_2O_3$ ) due to its useful applications in technology. Its mechanical, optical and electrical properties make it very well suited for pulsed laser structuring. In particular was discovered that laser ablation of  $Al_2O_3$ , which is also valid for all wide band gap materials, can proceed with two phases, so called "gentle" and "strong". The first one is characteristic for low laser

fluences ( $I < 3\text{--}5\text{J/cm}^2$ ) and is described with removal of a few *nm* from the surface of the material. In this regime was not observed the formation of the “corona” (typical for nanosecond ablation). The “gentle” phase is very efficient for patterning. The “strong” phase ( $I > 10\text{J/cm}^2$ ) is characterized with high ablation rate, it develops plasma emission and generates phase explosion [hen99, hert01]. However the “strong” regime gives opportunity for fast high-quality processing like cutting, drilling holes. Suitable choice of pulse width and laser fluence makes possible the tuning of the process of ablation in respect with the purpose to be fulfilled.

### 1.4.3 Ionization mechanism in dielectrics

Many technologies are using dielectric materials such as polymers, optical glasses, oxide ceramics and silica aerogels for microfabrication. This type of materials exhibit minimal absorption at low laser fluences and deposition of sufficient energy is very important during material processing for the optical breakdown to occur. The ionization process in dielectrics is governed by avalanche ionization and multiphoton ionization. Avalanche ionization is typical for long pulse durations (nanosecond range) and is caused when free electrons absorb the laser energy through inverse bremsstrahlung [fan01]. The free carriers absorb laser photons and impact with other bound carriers during the inverse bremsstrahlung lasts. Thus ionization by impact with other molecules is reached, and new free electrons are created, the density of free electrons increases and avalanche ionization starts to develop (Figure 10); [fan01, lenz99, hert01, sun00]. These newly formed electrons start to transfer the energy to the lattice and ions and the material begun to heat and vaporize. So is initiated the laser ablation.

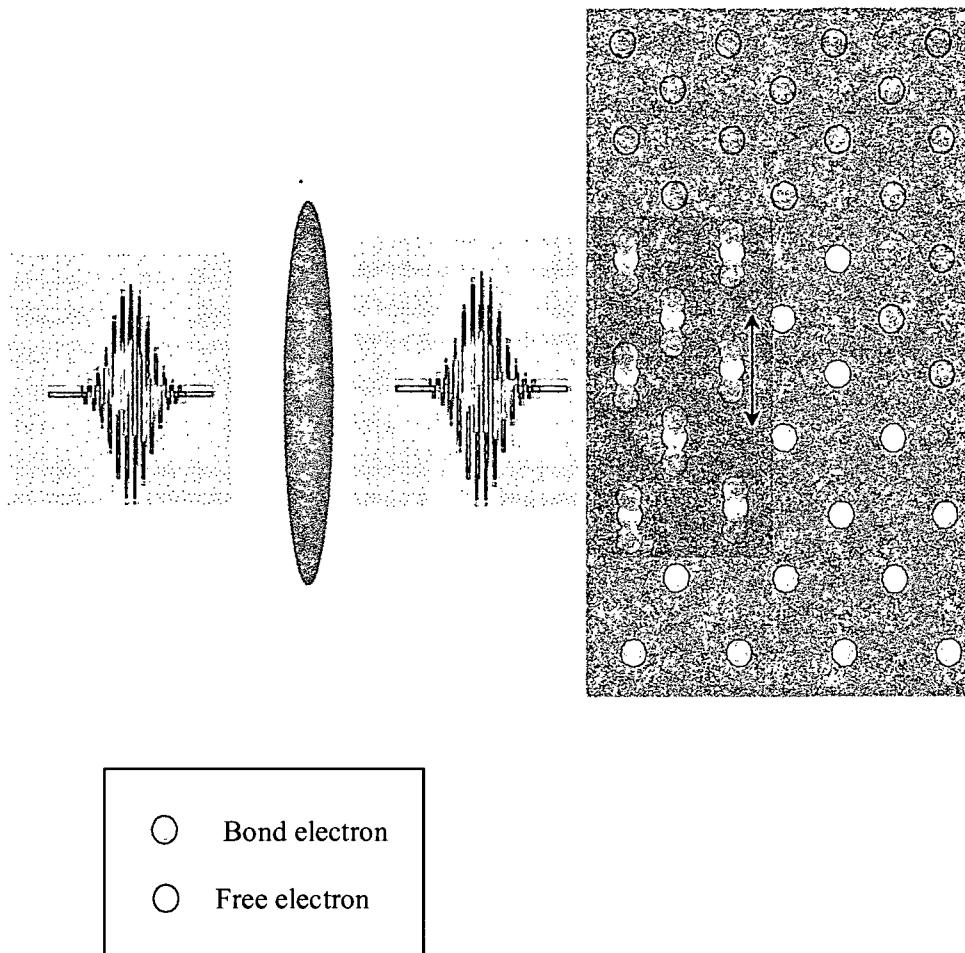


**Figure 10:** Avalanche ionization.

*Multi-photon ionization (MPI)* dominates for extremely short pulses ( $<50\text{fs}$ ). The absorption of several photons simultaneously leads to ionization of the molecule. The both processes (*MPI* and avalanche ionization) required threshold intensity to trigger the optical breakdown

## Chapter 2

### 2. Experimental Setup

In the present thesis was emphasized on the examination of the interaction mechanism of the high intensity femtosecond laser pulses with organic material (tooth, bones), and also interaction with metals in order to gain a detailed information of the underlying processes. The intention was to determine the general features of different ablation processes (ns, fs). The aim was to perform a complete set of measurements of different target materials by means of Mass spectrometry studies. The method which was used is post-ionization of the neutral particles and Time-of-Flight Spectroscopy. The experiments were carried out under UHV conditions with a base pressure  $10^{-10}$  Torr. The experimental laser system comprises femtosecond mode-locked mirror-dispersion controlled Ti:sapphire oscillator (Laser Source Pro HP) pumped by diode pumped Verdi laser, 9-pass CPA Ti:sapphire amplifier (Omega Pro) pumped by Nd:Ylf laser and ArF Excimer laser (193nm) for post – ionization was used. The UHV chamber was equipped with reflectron type TOF mass spectrometer for detection and Ion gun [schmidt02], [hus 96], [hus 93], [wurz 91].

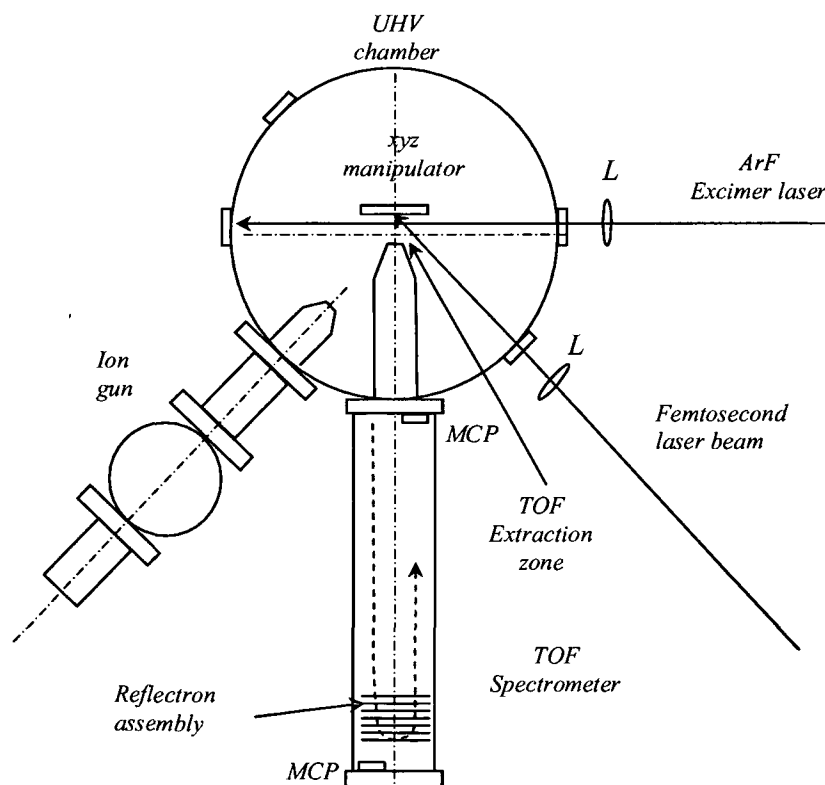


**Figure 11:** The schematic diagram of the experimental system: L-lens, MCP-Micro channel plate detector, TOF-Time-of-Flight spectrometer.

The UHV chamber has a diameter of 35cm. The chamber itself has an independent pumping stage which comprises a prevacuum pump (*Pfeifer-Balzars*) and a turbomolecular pump (*Leybold Turbovac 360*).

On this chamber are mounted the Time-of-Flight mass spectrometer, the ion gun and the high precision xyz target manipulator. The pumping system of the spectrometer and the ion gun comprises a prevacuum pump (*Alcatel*) and turbomolecular pumps for each device. The whole vacuum system is baked out (for experiments with metal samples) for 24 hours thus the contaminants are released from the surfaces of the recipients and thus the vacuum conditions are in the order of  $10^{-10}$ Torr.

As target materials metal targets (aluminum, copper, and silver) and biological samples (tooth, bones) were examined.

The ion source generates beams of xenon ions. They are accelerated to 9kV  $Xe^+$  ions, guided by an assembly of electrooptical lenses and deflection plates and focused to a spot of a few mm in diameter.

As it was mentioned above the system is equipped with Time-of-Flight mass spectrometer which has two modes of operation (depending on the experiment to be performed): linear and reflectron mode. Employing the second mode has the advantage that the secondary ions are electrostatically suppressed. The reflectron is an ion mirror consisting of a series of grids.

After the particles are created they are extracted and accelerated into the drift region ( $U_d = 2kV$ ). Details about the theory of mass separation by TOF method will be introduced in paragraph 2.2.

- *Ultra-short laser ablation experiments*

For the ablation experiments the amplified laser beam was focused into the chamber with 30mm focal length lens into a spot of 50 $\mu$ m diameter. The laser beam was incident to the target under an angle of 45°. For the experiments performed with organic samples the pressure in the chamber was in the order of  $10^{-8}$ Torr. In order not to affect the composition of the organic material the UHV chamber was not baked out.

The targets were mounted on a xyz target manipulator this allows to translate the target and thus to expose each pulse to a virgin spot. The organic samples were cut with diamond saw. The tooth samples were cut perpendicularly to the longest sides into 1mm thick slices and were mechanically polished. In order to prevent charging of the organic sample copper wires were mounted around the surface of the sample to suppress the charging effect.

- *US-LSNMS experiments*

The post-ionizing laser beam was armed to fire at a programmable time delay of  $1\mu s$  later in respect to the ablation beam. The post-ionizing laser beam intersects the ionization volume at a distance  $\approx 2mm$  above the target surface, where was detected the optimal signal. The distance (target→laser beam) was measured (accurately as possible) by translating the target holder until it intersects the laser beam and a slight trace on the surface of the target is visible.

The effective ionization volume was controlled by translating the focusing lens.

The sample was ablated with femtosecond laser and the ablated particles were post-ionized with an ArF ( $193nm$ ) excimer laser which delivers pulses of  $\approx 20ns$  duration.

- *SIMS and SNMS experiments*

For the SIMS experiments the ion beam was incident on the target surface under an angle of  $45^\circ$  regarding the target normal. The working gas was Xe. The beam diameter was  $\approx 1mm$ . The ion gun can be operated in two modes: continuous or pulsed. The first one was used mainly to clean the target surface, and the second was operated when the data was acquired.

The ions signal was detected with a *micro-channel-plate assembly (MCP)* and after this is sent to a *LeCroy* transient recorder whose output is transferred through a GPIB interfacing to a computer for storage and further manipulation.

The femtosecond laser system delivers pulses in the order of  $30 fs$ , when optimized the pulse duration can go down to  $25 fs$ . However due to the propagation through all optical elements (lens, quartz mirrors) we estimated that the pulse duration can widen to  $35fs-40fs$  (with two quartz mirrors) due to the undesirable *GVD*. This can be compensated by readjusting the overall compressor dispersion.

The pulse duration was measured with an autocorrelator (*Femtometer*). A 0.5% beamsplitter was inserted in the beam line, prior to enter in the chamber, to reflect a part of the laser intensity to the autocorrelator. This arrangement allows us also to switch fast to measurement of the laser intensity, which is of crucial importance for the measurements. The power measurements were performed with a pyro-electrical energy measuring device (*PEM*).

## 2.1 Timing of the experiment

The whole laser system is triggered at 1 KHz repetition frequency provided by a frequency generator (*Takt generator*). The source trigger is a TTL signal split in two. One output of the *Takt* generator triggers the *Q*-switch driver of the *Nd:YIF* laser. The second one is sent to *LeCroy 4222* (DG) and split in two signals which are sent to the *LeCroy 2323* module (*ChA* and *ChB*).

The acquisition chain consists of several modules:

- The *LeCroy 4222* Gate and Delay Generator have 4 channels which are capable to introduce a programmable time delay
- The *LeCroy 8828* Waveform Digitizer is digitizing and recording high frequency signals. This module can be operated in two modes: normal and burst mode. In the burst mode it is possible to record the signals only if it is present a burst control signal.
- The memory module *LeCroy 8104* provides 32 ksamples of memory at 200MHz digital bandwidth
- The *LeCroy 6010* controller - the data are transferred through *IEEE-488* interface bus.
- The *LeCroy 2323* is a programmable gate and delay generator with two channels. It provides a TTL and ECL outputs.



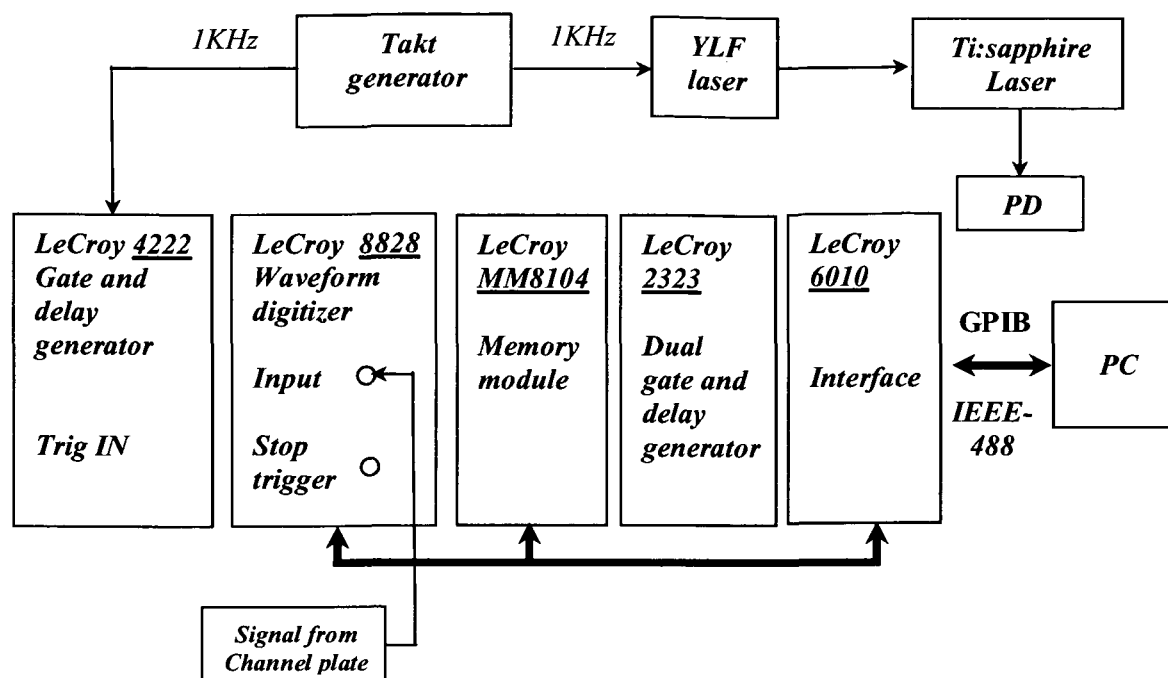


**Figure 12:** Trigger and acquisition setup of the experiment.

The post-ionizing laser (excimer laser) is set to fire at a delay time  $t_d \approx 1\mu\text{s} - 5\mu\text{s}$  (depending of the material to be examined) after the ablation laser impact (Figure 13).

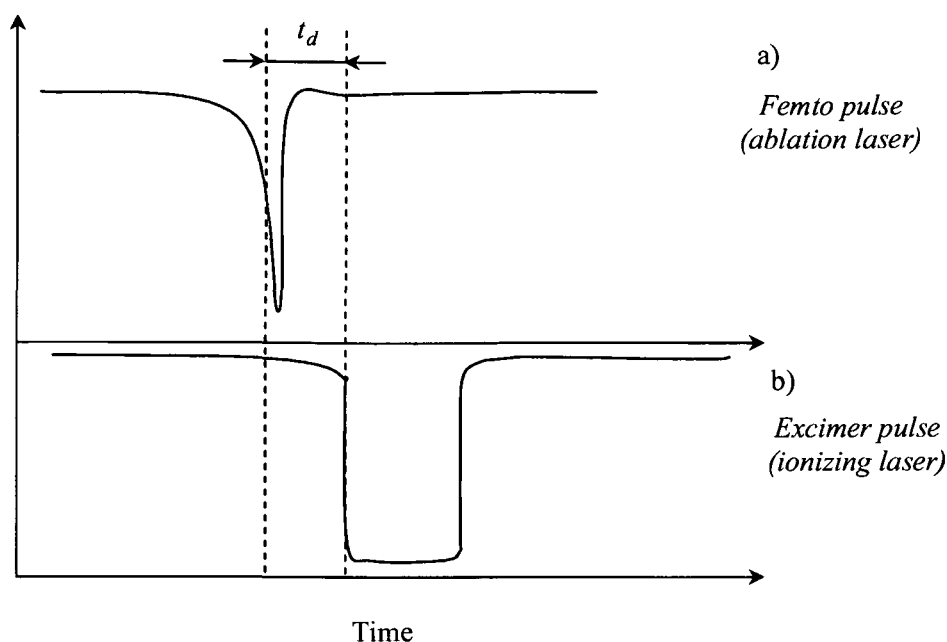


**Figure 13:** Timing diagram of the US-LSNMS measurements: a) photodiode signal of the laser pulse from the Ti: sapphire laser; b) photodiode signal of the laser pulse from the Excimer laser. The time difference between the two negative slopes determines the time delay ( $t_d$ ) for the post-ionizing laser (Excimer) in correspondence to the ablation laser pulse (Ti: sapphire).

The excimer laser operates at 16Hz frequency and the trigger pulse has to be +15V and duration between 10 and 100 $\mu$ s.

## 2.2 The TOF mass spectrometer

The basic idea of the TOF method is that ions with the same kinetic energy will move with different velocities depending of the  $m/z$  value. The advantage of this method consists in the possibility for simultaneous registration of the whole mass spectrum of the ablated species. The ablated particles are accelerated, mass separated into the drift tube and detected with a micro channel plate detector according to their mass-to-charge ratio.

The kinetic energy of an ion due to an applied potential is given by the relation (Equation 9):

$$U = zeV \quad (\text{Equation 9})$$

Where:

$U$  – kinetic energy of the ion

$V$  – applied charge

$z$  – charge

The kinetic energy is related to the velocity through relation (Equation 9.1):

$$U = \frac{1}{2}mv^2 \quad (\text{Equation 9.1})$$

This relation can be rearranged in equation (Equation 9.2):

$$v = \sqrt{\frac{2zeV}{m}} \quad (\text{Equation 9.2})$$

Equation (Eq.6.2) is expressing the ion velocity following the acceleration pulse  $V$ . If the distance from the point of ion formation to the detector is  $D$ , then the formula for the time-of-flight can be derived (Equation 9.3):

$$t = \frac{D}{v} = D \times \sqrt{\frac{m}{2zeV}} \quad (\text{Equation 9.3})$$

From equation (Eq.6.3) can be made the conversion of the flight time to mass (Equation 9.4):

$$\frac{m}{z} = 2eV \left( \frac{t}{D} \right)^2 \quad (\text{Equation 9.4})$$

Thus when the dimension of the drift tube and the applied potential are known  $m/z$  value can be defined. In most cases when we have two known masses the calibration of

the experimental TOF data can be performed by fitting the time-of-flight data in to (Equation 9.5).

$$\frac{m}{z} = at^2 + b \quad (\text{Equation 9.5})$$

The calibration constants (a, b) are defined with a least-squares regression.

## 2.3 Ultra-short pulse generation

I will start the introduction to the laser system with a short discussion of the ultra-short laser theory.

Three main points have to be considered for efficient amplification of short pulses.

1. *For high gain amplification the amplifying medium must exhibit sufficient bandwidth to support the seed pulse bandwidth.*
2. *The amplifier must be operated near the saturation fluence of the gain medium for efficient extraction of the energy stored in the amplifier.*
3. *The peak intensity must be kept low in order to avoid optically induced damage.*

In the past years the  $Ti : Al_2O_3$  crystal was discovered to suite very well the field of ultrashort light generation. In the structure of the sapphire crystal the  $Ti^{3+}$  ion substitutes the  $Al^{3+}$  ion. It is very efficient broadly tunable material. The tuning covers the diapason from  $680nm$  to  $1100nm$ . The absorption band in the blue-green part of the spectrum is very wide. The emission bands are shifted towards low energies ( $750nm$ ). The  $Ti : Al_2O_3$  can be efficiently pumped by frequency doubled Nd lasers an Ar lasers.

In general light amplification can be established only if the gain of the medium exceeds the losses. Let us consider a laser cavity in which are established several modes lasing simultaneously and summed with random phases. In this case the intensity distributions of the pulses will be also random. To obtain a stable pulse train the phases must be adjusted so to be held constant (locked), thus the peak power will increase. Two main ideas are developed for forcing thousands of modes to operate simultaneously.

- Passive mode-locking: is based on the insertion of saturable absorber for making the selection of one single pulse.

- Active mode-locking: external modulation of the cavity losses or the gain of the amplifying medium.

- Self-Locking (Kerr lens mode-locking): the Kerr effect implies the fact that the refractive index of a nonlinear medium is intensity dependent:

$$n = n_0 + n_2 I \quad (\text{Equation 10})$$

Thus the Gaussian wave will suffer the nonhomogeneity of the refractive index as it passes through the amplifying medium. When  $n_2$  is positive the refraction increases in the axis of the beam and the medium acts as a converging lens (self-focusing effect). The self-focusing effect is stronger for high intensities.

When the laser is operated in its usual regime it oscillates simultaneously over all resonance frequencies of the cavity for which the gain exceeds the losses. These modes are called longitudinal modes. In order to change to a pulsed regime, power fluctuations must be created which will establish strong Kerr lens effect. By initiating a perturbation in the optical length in the cavity one can very easily obtain the transition from continuous to pulsed mode.

After the pulse is formed two other mechanisms are affecting the fs pulse length and structure, they are the self-phase modulation (SPM) and the group-velocity dispersion (GVD).

The change of the refractive index due to the Kerr lens effect is small at the leading and trailing edges of the pulse but in the center of the pulse is large. So some part of the pulse moves faster and are affecting the pulse shape and causing the self-phase modulation effect. The refractive index determines the phase velocity of the material, and it is also wavelength dependent. The first derivative of the refractive index determines the group velocity of a wave packet. The second derivative defines the GVD; it influences the phase changes in the different frequency components. The different frequency components are possessing different phase velocities, so the pulse experiences modulation which results in reshaping of the pulse and introducing a "chirp" – change in frequency with time. To avoid the "chirp" effect, the positive GVD has to be compensated. For this reason has to be inserted in the cavity an optical element which is introducing a negative dispersion.

In summary the GVD introduces spectral dephasing and SPM introduces temporal dephasing and creates new frequencies redder (in comparison to the pulse central frequency) in the leading edge of the pulse and bluer in the trailing edge. So a very large spectrum is established however the pulse can not be shortened by itself. That is the reason why after the SPM a dispersive element must be inserted after which the frequencies are rephased.

As an example of such an element a pulse compressor can be composed of a pair of prisms. By varying the optical path between the prisms, the dispersion compensation can be achieved.

### 2.3.1 Specifications of the experimental laser system

The Amplifier used in the present experiment is seeded by a broadband femtosecond pulses (10fs duration) established in a passively mode-locked  $Ti:Al_2O_3$  oscillator. The oscillator system is pumped by a 5W diode pumped *Verdi* laser. The mirror-dispersion-controlled (MDC) oscillator contains set of chirped mirrors for broadband intra-cavity group-delay-dispersion (GDD) control in the Ti:Sapphire oscillator and low-dispersion quarter-wave mirrors for coupling the pump beam into and mode-locked pulse out of the resonator. The configuration of the resonator has an x-shape view. The resonator has two cavity arms: short (d1) and a long cavity arm (d2).

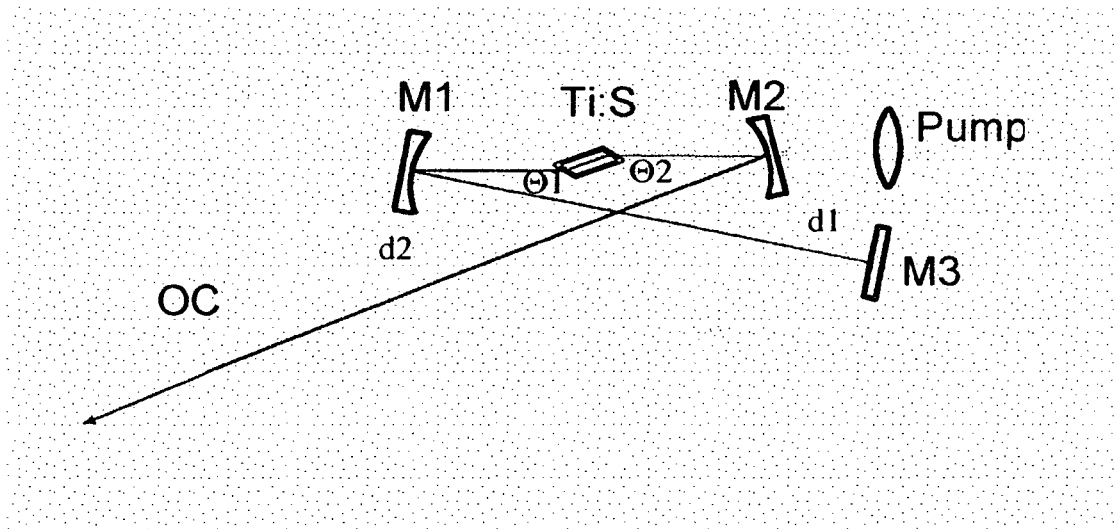


**Figure 14:** Layout of the oscillator cavity.

In order to have a stable operation of the cavity, the term stability range is necessary to be defined. This is the range of distances between mirrors M1 and M2 for which the cavity is stable, in another words the oscillation is possible. It is expedient to introduce the parameters  $\delta = d - 2f$ , where  $d$  is the optical distance between mirrors M1 and M2 and  $f$  stands for the focal length of the focusing mirror. The stability range consists of two discrete regions with a gap in between. The width of the gap increases with the cavity asymmetry factor  $\gamma = \frac{\delta_2}{\delta_1}$ .

The presented oscillator utilizes the KLM technique for mode-locking. Self focusing introduced by the optical Kerr effect in the gain medium changes the confocal parameter of the cavity mode. The mode-locking in the experimental set up is started by realizing a small perturbation of the cavity length.

### MDC Oscillator

<i>Parameters</i>	<i>Specifications</i>
<i>Pulse duration</i>	<i>12fs</i>
<i>Spectral width</i>	<i>75nm FWHM, centered at 800nm</i>
<i>Output power</i>	<i>300mW</i>
<i>Peak power</i>	<i>400kW</i>
<i>Pump power</i>	<i>5W</i>

**Table 2:** Specifications of the MDC oscillator.

The typical mode-locked spectra of the  $Ti:Al_2O_3$  oscillator is shown on (Figure 15)

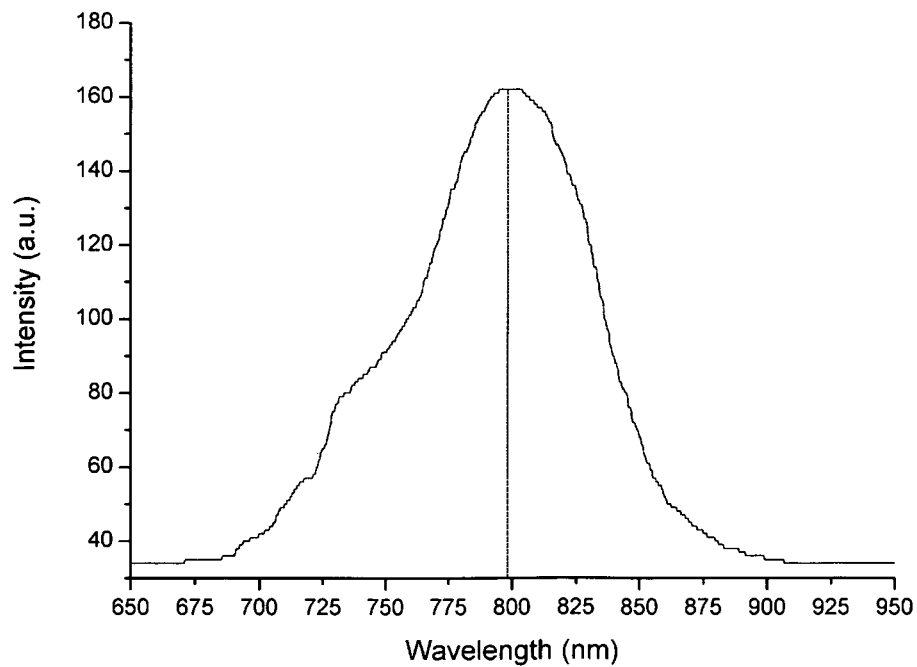


**Figure 15:** Oscillator output spectrum.

The femtosecond multipass amplifier system provides 30fs pulses at 1 kHz repetition rate and laser intensity  $10^{15} \text{ W/cm}^2$ , peak wavelength 800 nm, 1mJ pulse energy and photon energy  $\approx 1.5 \text{ eV}$ . The pump laser for the amplifier is a frequency doubled Multi-KHz Nd:YLF laser emitting at 527nm (Figure 16). The amplifier chain is seeded by broadband ( $\Delta\lambda=100\text{nm}$ ) femtosecond pulses from MDC Titanium:sapphire oscillator and it consists of two stages: amplifier and compressor.

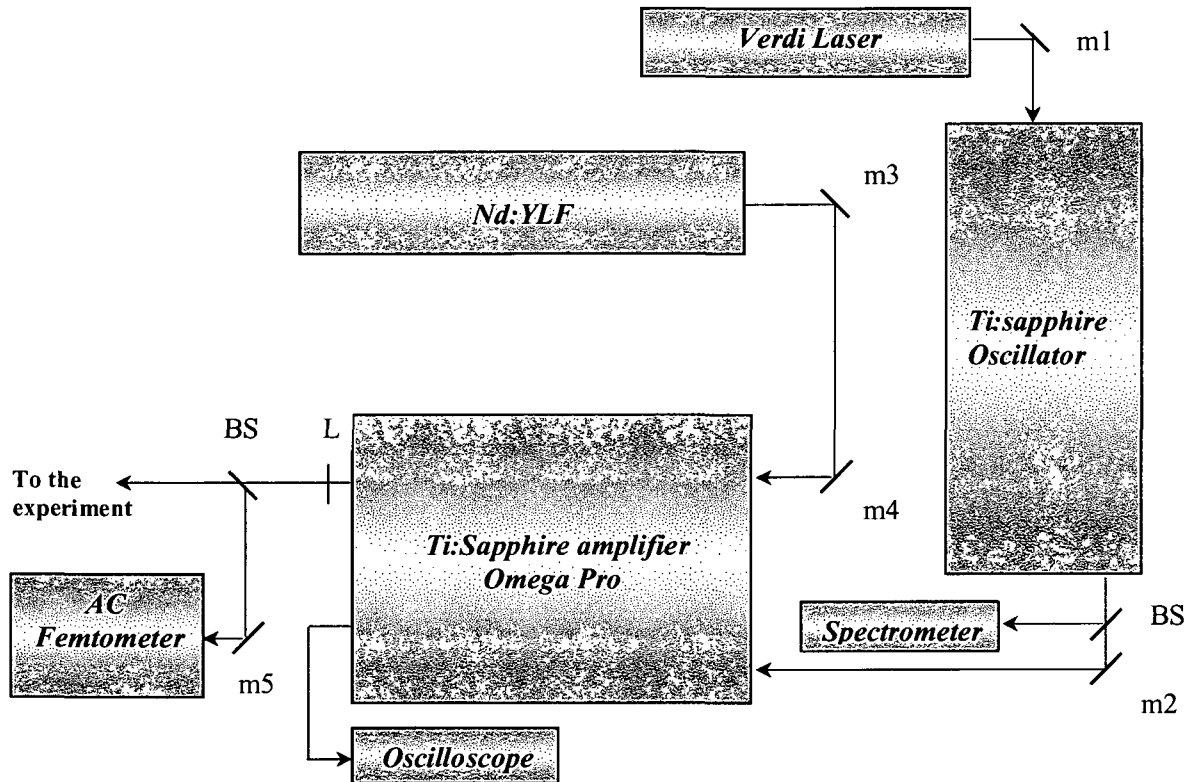


Figure 16: Block diagram of the Femtosecond laser system.

Before to direct the seed pulses to the amplifier, the intensity must be reduced by stretching the pulses to a safe value. The multipass amplifier uses a modified version of chirp pulse amplification (CPA). The modification of the CPA is expressed in the moving of the pulse selection to a place where the pulses are already amplified to a pulse train with the envelope of the pump laser. The priority of this is the reduced energy content of amplified spontaneous emission (ASE) in the output pulse train. In the present system the main stretching is achieved mainly in the faraday isolator. The amplifier has a 9-pass arrangement of the seed beam, which focuses in 2.7 mm long, Ti:sapphire crystal.

The amplifier comprises a prism compressor mounted on a translation stage. Changing the position of the prisms the amount of glass in the path of the beam is



different and can be achieved control over the overall compressor dispersion. This can prolong the pulses up to  $100\text{fs}$ .

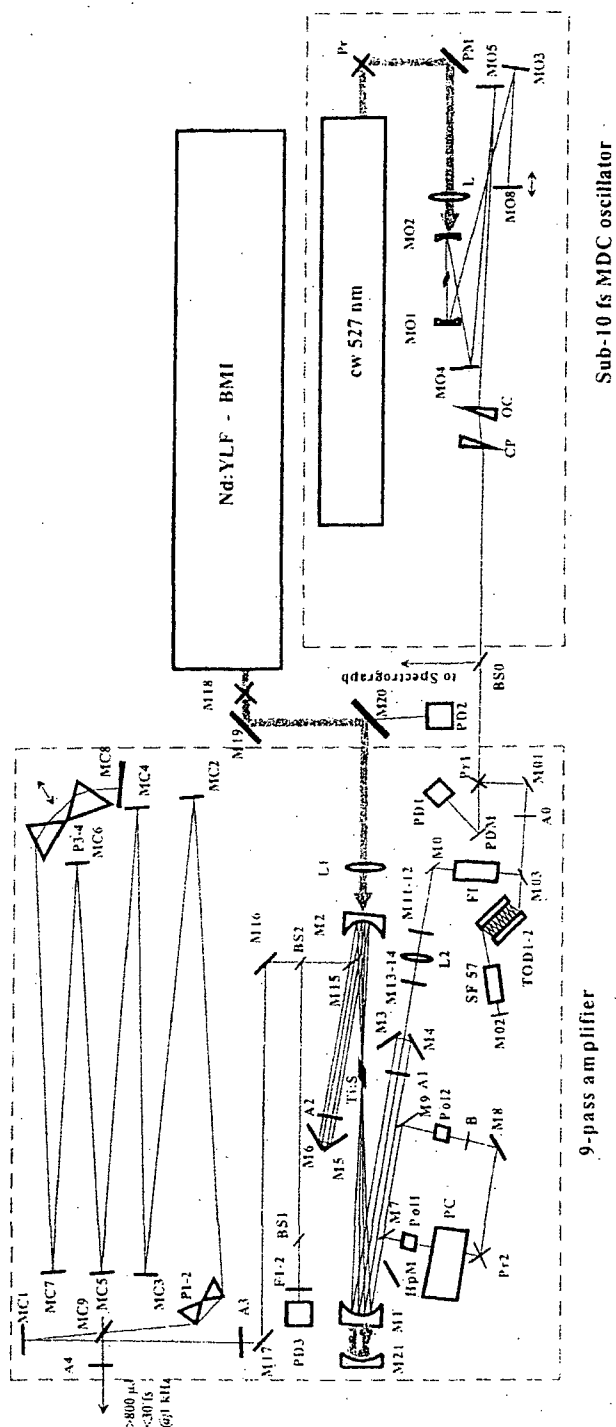


Figure 17: Schematic layout of the Amplifier system.

In summary the main features representative for the amplifier system are:

1. *The seed pulses are stretched in front of the amplifier upon traversing optical components in order to prevent any damage of the optical elements.*
2. *The gain narrowing is reduced due to the 9-pass arrangement of the seed beam.*
3. *The use of a vacuum chamber for the Ti:sapphire crystal makes possible to avoid pollution of the crystal surfaces, thus increasing the efficiency of the amplifier performance.*
4. *Chirped pulse amplification scheme.*

<i>Parameters</i>	<i>Specifications</i>
<i>Pulse duration</i>	<i>&lt;30fs</i>
<i>Spectral width</i>	<i>&gt;45nm FWHM, centered at <math>800 \pm 10\text{nm}</math></i>
<i>Output power</i>	<i>&gt;800mW</i>
<i>Pulse energy</i>	<i>&gt;800 <math>\mu\text{J}</math></i>
<i>Peak power</i>	<i>&gt;30GW</i>
<i>Pump power</i>	<i>BMI 621, &gt;12mJ, 527nm, pulse duration 100-500ns</i>

*Table 3: Specifications of the amplifier (Omega Pro).*

### 2.3.2 Pulse width measurements

Light is a transverse, electromagnetic wave characterized by time-varying electric and magnetic fields. These fields in the expression of semiclassical treatment are characterized by the Maxwell equations.

When dealing with electromagnetic pulses, a complex representation of the electric field is very convenient. For such kind of representation it is possible to neglect the spatial dependence of the electric field.

$$E(x, y, z, t) = E(t) \quad (\text{Equation 11})$$

The complex spectrum of the field strength  $\tilde{E}(\Omega)$  can be defined through the complex Fourier transform ( $F$ ) [diels95].

$$\tilde{E}(\Omega) = F\{E(t)\} = \int_{-\infty}^{\infty} E(t) e^{-i\Omega t} dt = |\tilde{E}(\Omega)| e^{i\Phi(\Omega)} \quad (\text{Equation 12})$$

where  $|\tilde{E}(\Omega)|$  stands for the spectral amplitude and  $\Phi(\Omega)$  is the spectral phase. Since  $E(t)$  is real:

$$\tilde{E}(\Omega) = \tilde{E}^*(-\Omega) \quad (\text{Equation 13})$$

Given  $\tilde{E}(\Omega)$ , the time dependent electric field is obtained through the inverse Fourier transform ( $F^{-1}$ ):

$$E(t) = F^{-1}\{\tilde{E}(\Omega)\} = \frac{1}{2\pi} \int_{-\infty}^{\infty} \tilde{E}(\Omega) e^{i\Omega t} d\Omega \quad (\text{Equation 14})$$

In practice it is not convenient to use functions, which are non-zero for negative frequencies. This can be avoided by introducing the electric field as:

$$\tilde{E}^+(t) = \frac{1}{2\pi} \int_0^{\infty} \tilde{E}(\Omega) e^{i\Omega t} d\Omega \quad (\text{Equation 15})$$

The  $\tilde{E}^+(t)$  and  $\tilde{E}^+(\Omega)$  are related to each other by the equations:

$$\tilde{E}^+(t) = \frac{1}{2\pi} \int_{-\infty}^{\infty} \tilde{E}^+(\Omega) e^{i\Omega t} d\Omega \quad (\text{Equation 16})$$

and

$$\tilde{E}^+(\Omega) = \int_{-\infty}^{\infty} \tilde{E}^+(t) e^{-i\Omega t} dt \quad (\text{Equation 17})$$

The real electrical field and its complex Fourier transform can be expressed by equations:

$$E(t) = \tilde{E}^+(t) + \tilde{E}^-(t) \text{ and } \tilde{E}(\Omega) = \tilde{E}^+(\Omega) + \tilde{E}^-(\Omega) \quad (\text{Equation 18})$$

It can be also shown that  $\tilde{E}^+(t)$  can be derived through analytic continuation of  $E(t)$

$$\tilde{E}^+(t) = E(t) + iE'(t) \quad (\text{Equation 19})$$

The complex electric field  $\tilde{E}^+(t)$  is usually represented by a product of an amplitude function and a phase term:

$$\tilde{E}^+(t) = \frac{1}{2} \varepsilon(t) e^{i\varphi(t)} \quad (\text{Equation 20})$$

In most practical cases the spectral amplitude is centered around a mean frequency  $\omega_l$ . In time domain this suggests introducing of carrier frequency  $\omega_l$  and writing the  $\tilde{E}^+(t)$  in the following way:

$$\tilde{E}^+(t) = \frac{1}{2} \varepsilon(t) e^{i\varphi(t)} e^{i\omega_l t} = \frac{1}{2} \tilde{\varepsilon}(t) e^{i\omega_l t} \quad (\text{Equation 21})$$

In (Equation 21)  $\varphi(t)$  is the time dependent phase, and  $\tilde{\varepsilon}(t)$  is the complex field envelope, and  $\varepsilon(t)$  is the field envelope. This description of the field is more general, however some special cases exist where the usefulness of the concept of an envelope and carrier frequency is limited, when the bandwidth is a small fraction of the carrier frequency:

$$\frac{\Delta\omega}{\omega_l} \ll 1 \quad (\text{Equation 22})$$

Given the spectral description of the signal,  $\tilde{E}^+(t)$  the complex envelope  $\tilde{\varepsilon}(t)$  is the inverse transform of the translated electric field:

$$\tilde{\varepsilon}(t) = \frac{1}{2\pi} \int_{-\infty}^{\infty} 2\tilde{E}^+(\Omega + \omega_l) e^{i\Omega t} d\Omega \quad (\text{Equation 23})$$

Spectral translation of Fourier transforms is a standard technique to reconstruct the envelope of interference patterns.

The related quantities which are important to us are: power, energy and intensity. The pulse power can be derived from the Poynting theorem:

$$P(t) = \epsilon_0 c n \int_A dS \frac{1}{T} \int_{t-\frac{T}{2}}^{t+\frac{T}{2}} E^2(t') dt' \quad (\text{Equation 24})$$

where the  $\int_A dS$  stands for integration over the beam cross section. A temporal integration of the power gives the energy:

$$W = \int_{-\infty}^{\infty} P(t') dt' \quad (\text{Equation 25})$$

The corresponding quantities per unit area are the intensity ( $\text{W}/\text{cm}^2$ ):

$$I(t) = \epsilon_0 c n \frac{1}{T} \int_{t-\frac{T}{2}}^{t+\frac{T}{2}} E^2(t') dt' = \frac{1}{2} \epsilon_0 c n E^2(t) = 2 \epsilon_0 c n \tilde{E}^+(t) \tilde{E}^-(t) = \frac{1}{2} \epsilon_0 c n \tilde{E}(t) \tilde{E}^*(t) \quad (\text{Equation 26})$$

The given characterization of the electric field in this paragraph simplifies further explanations concerning the nature of femtosecond pulses.

A way to describe the pulse width is the intensity autocorrelation function given by the formula:

$$A_{\text{int}}(\tau) = \int_{-\infty}^{\infty} I(t) I(t - \tau) dt \quad (\text{Equation 27})$$

The pulse duration can be defined as the full width at a half maximum (FWHM) of the intensity profile and the spectral width as the FWHM of the spectral intensity. It is also necessary to be noted that the intensity autocorrelation function contains no information about the pulse phase. To calculate the pulse duration from the intensity autocorrelation the most useful way is to assume a  $\text{sech}^2$  pulse shape and determine the ratio between the FWHM of the autocorrelation and that of the pulse.

Let us consider that an incident pulse train is split into two beams, which have equal intensity  $I_1(t)$  and  $I_2(t)$ . The two beams travel different path lengths, and adjustable

optical delay is imparted to one of the beams. The delay time between the two beams is  $\tau = \Delta s/c$ , where  $\Delta s = s_1 - s_2$ .

The real field on the detector, resulting from the interferences of  $E_1$  and  $E_2$  is:

$$E = E_1(t - \tau) + E_2(t) \quad (\text{Equation 28})$$

The intensity at the output is given by the formula:

$$\begin{aligned} I(t, \tau) &= \varepsilon_0 c n \frac{1}{T} \int_{t-\frac{T}{2}}^{t+\frac{T}{2}} [E_1(t - \tau) + E_2(t)]^2 dt = 2\varepsilon_0 c n [\tilde{E}_1^+(t - \tau) + \tilde{E}_2^+(t)] [\tilde{E}_1^-(t - \tau) + \tilde{E}_2^-(t)] \\ &= \frac{1}{2} \varepsilon_0 c n \{ \tilde{\mathcal{E}}_1^2(t - \tau) + \tilde{\mathcal{E}}_2^2(t) + \tilde{\mathcal{E}}_1^*(t - \tau) \tilde{\mathcal{E}}_2(t) e^{i\omega_l \tau} + \tilde{\mathcal{E}}_1(t - \tau) \tilde{\mathcal{E}}_2^*(t) e^{-i\omega_l \tau} \} \end{aligned}$$

$$(\text{Equation 29})$$

Here  $c$  is the velocity of light in vacuum. The field is again decomposed in an amplitude function  $\tilde{\mathcal{E}}$  and a phase function centered around an arbitrary average frequency of the radiation,  $\omega_l$ .

The output signal can be measured by a detector (photodiode, photomultiplier), and the actual recorded signal is the intensity,  $\bar{I}$ , averaged over the response time  $\tau_{res}$  of the detector. In the case of ultrashort pulses  $\tau_{res} \gg \tau_p$  holds and what is being measured is the time integral:

$$\int_{-\infty}^{\infty} I(t', \tau) dt' \quad (\text{Equation 30})$$

Assuming that all fluctuations are averaged out by the detector's slow response, the measured signal (Equation 29) reduces to the following expression [5]:

$$\begin{aligned} \bar{I}(\tau) &= \frac{\varepsilon_0 c n}{4} \{ \langle \tilde{\mathcal{E}}_1^2 \rangle + \langle \tilde{\mathcal{E}}_2^2 \rangle + \langle \tilde{\mathcal{E}}_1^*(t - \tau) \tilde{\mathcal{E}}_2(t) e^{i\omega_l \tau} + \tilde{\mathcal{E}}_1(t - \tau) \tilde{\mathcal{E}}_2^*(t) e^{-i\omega_l \tau} \rangle \} \\ &= \varepsilon_0 c n \{ A_{11}(0) + A_{22}(0) + \tilde{A}_{12}^+(\tau) + \tilde{A}_{12}^-(\tau) \} \end{aligned} \quad (\text{Equation 31})$$

This equation involves the electric field rather than the intensities. The two complex functions correspond to positive and negative spectral components of a correlation function  $A_{12}(\tau) = \tilde{A}_{12}^+(\tau) + \tilde{A}_{12}^-(\tau)$  where the positive frequency component is defined as:

$$\begin{aligned}\tilde{A}_{12}^+(\tau) &= \frac{1}{4} \langle \tilde{\mathcal{E}}_1^*(t-\tau) \tilde{\mathcal{E}}_2(t) e^{i\omega_1 \tau} \rangle = \\ &= \frac{1}{2} \tilde{A}_{12}(\tau) e^{i\omega_1 \tau}\end{aligned}\quad (\text{Equation 32})$$

The Fourier transform is:

$$\tilde{A}_{12}^+(\Omega) = \int_{-\infty}^{\infty} \tilde{A}_{12}^+(\tau) e^{-i\Omega \tau} d\tau = \frac{1}{4} \tilde{\mathcal{E}}_1^*(\Omega - \omega_1) \tilde{\mathcal{E}}_2(\Omega - \omega_1) = \tilde{E}_1^*(\Omega) \tilde{E}_2(\Omega) \quad (\text{Equation 33})$$

Up to now we have defined the field correlation measured by the autocorrelator as:

$$G_1(\tau) = \tilde{A}_{12}^+(\tau) + c.c. = \frac{1}{4} \int_{-\infty}^{\infty} \tilde{\mathcal{E}}_1(t) \tilde{\mathcal{E}}_2^*(t-\tau) e^{i\omega_1 \tau} dt + c.c. \quad (\text{Equation 34})$$

If we put in front of the detector a second harmonic generating crystal and a filter to block the fundamental the detected signal will be proportional to the function:

$$G_2(\tau) = \int_{-\infty}^{\infty} \left[ E_1(t-\tau) + E_2(t) \right]^2 dt \quad (\text{Equation 35})$$

Substituting for the fields the usual amplitude and phase dependence, the following expression can be derived:

$$G_2(\tau) = A(\tau) + \text{Re}\{4\tilde{B}(\tau)e^{i\omega_1 \tau}\} + \text{Re}\{2\tilde{C}(\tau)e^{2i\omega_1 \tau}\}, \quad (\text{Equation 36})$$

which shows the decomposition of the second order correlation.

In the above equation

$$A(\tau) = \int_{-\infty}^{\infty} dt \left\{ \mathcal{E}_1^4(t-\tau) + \mathcal{E}_2^4(t) + 4\mathcal{E}_1^2(t-\tau)\mathcal{E}_2^2(t) \right\} \quad (\text{Equation 37})$$

$$\tilde{B}(\tau) = \int_{-\infty}^{\infty} dt \left\{ \mathcal{E}_1(t-\tau)\mathcal{E}_2(t) \left[ \mathcal{E}_1^2(t-\tau) + \mathcal{E}_2^2(t) \right] e^{i[\varphi_1(t-\tau) - \varphi_2(t)]} \right\} \quad (\text{Equation 38})$$

$$\tilde{C}(\tau) = \int_{-\infty}^{\infty} dt \left\{ \varepsilon_1^2(t-\tau) \varepsilon_2^2(t) e^{2i[\varphi_1(t-\tau) - \varphi_2(t)]} \right\} \quad (\text{Equation 39})$$

The decomposition shows that the correlation has three frequency components centered on zero,  $\omega_i$  and  $2\omega_i$  frequency. In general it can be said that optical autocorrelators measure the correlation between the field amplitude  $E(t)$  or the intensity  $I(t)$  at the time  $t$  and its values  $E(t+\tau)$  or  $I(t+\tau)$  at a later time. The process of pulse shape identification is simplified if a set of typical test functions is available. Getting in more details it is necessary to explain the meaning of the (Equation 36).

Let us consider that  $E_1 = E_2 = E$ . The peak value of the function  $A(\tau)$  in (Equation 37) at  $\tau = 0$  will be  $6 \int \varepsilon^4(t) dt$  (Equation 40).

For large delays, the cross product term disappears leaving a background of  $A(\infty) = 2 \int \varepsilon^4 dt$  (Equation 41)

Measurement leading to  $A(\tau)$  are generally called intensity autocorrelation. When pulses are characterized by the intensity autocorrelation no information can be extracted about the phase, because the phase information is averaged out. The peak-to-background ratio (ratio of the peak value of the auto correlation function to its background value) in that case must be in the order of 3 to 1.

If the measurement is performed with interferometric accuracy, second-order autocorrelations provide much more contrasted pattern. All terms of the auto correlation (Equation 37-39) are recorded and the constructive interference terms at zero delay add to  $16 \int \varepsilon^4(t) dt$  (Equation 42)

The peak-to-background ratio in that case is 8 to 1. The intensity autocorrelation does not carry any phase information and thus the coherent pulses can not be distinguished from incoherent ones. In contrast the interferometric autocorrelation can provide phase information and is more sensitive to the pulse shape comparing to the intensity autocorrelation. Usually such kinds of correlations are exploited for:

- Testing the absence or presence of phase modulation
- Quantitatively measure the linear chirp
- Determination of the pulse shape and phase using fitting procedures



Characterization of the fs pulses in the current experiment was performed with a commercial autocorrelator (Femtometer). The precise knowledge of the pulse width is of crucial importance for the experiments. The incident beam is split into two parts with 50% beamsplitter, one part of the beam is sent to a variable-piezo-driven delay stage (connected with a frequency generator) in order to introduce a time delay. After this the two beams recombine again and are focused by a parabolic gold-coated mirror to a BBO crystal to generate a second harmonic. The obtained signal is detected with a photodiode and send to a computer for acquisition. The measured signal depends of the combined light intensity, which is a function of the time delay between the two pulses and the temporal pulse width of the laser. The autocorrelator is designed to switch easily from background free (non-collinear) to interferometric (collinear) mode. Examples of an interferometric and intensity autocorrelation obtained with the femtometer are shown below.

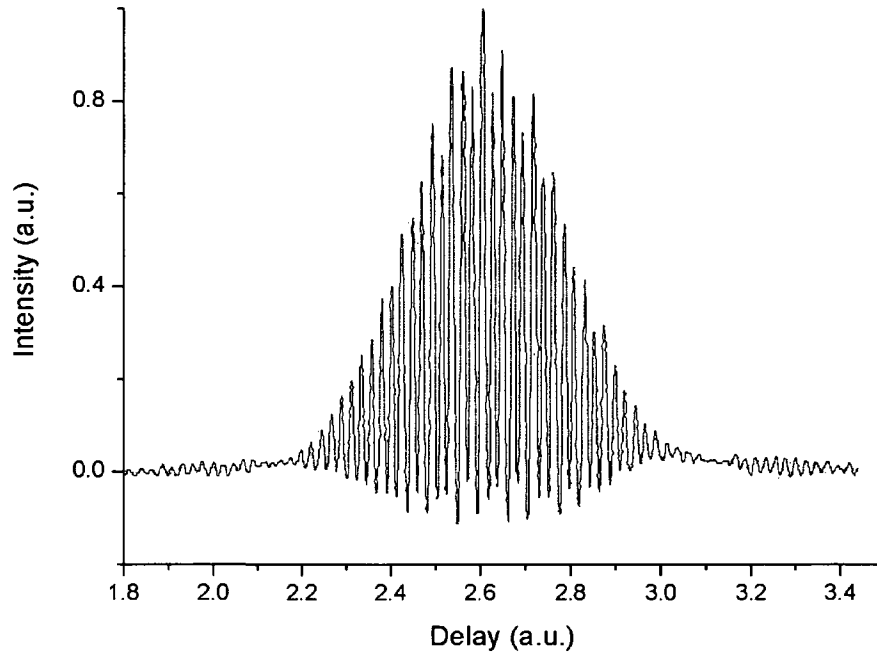


**Figure 18:** Interferometric autocorrelation: calculated fs pulse duration  $\approx 30$ fs.

The calculation is performed by estimating  $\Delta\tau = \lambda_0 / c$ . The recorded output amplifier spectrum (Figure 19) has a center wavelength  $790\text{nm}$ . So the fringe spacing ( $\Delta\tau$ ) is  $\approx 2.63\text{fs}$ . Counting the number of fringes ( $N$ ) above the 50% line (in proportion peak to background ratio 1:8) and after that estimating the deconvolution factor ( $B = 1.89$ ) assuming a  $\text{sech}^2$  profile, one can evaluate the pulse duration which is given by the formula

$$\text{Pulse duration} = N \cdot \Delta\tau / B$$

(Equation 43)

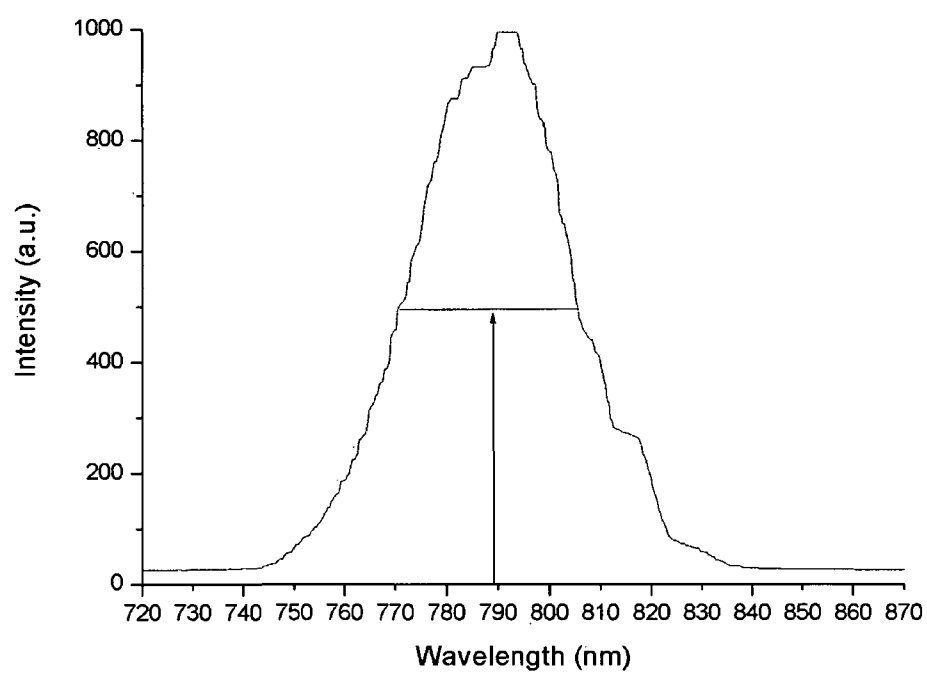


*Figure 19: Amplifier output spectrum.*

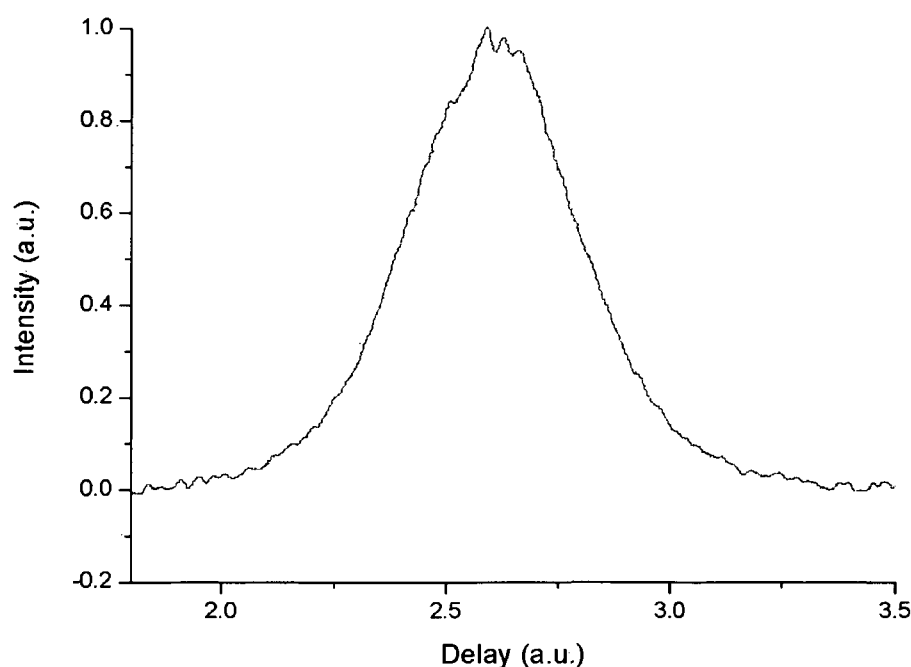


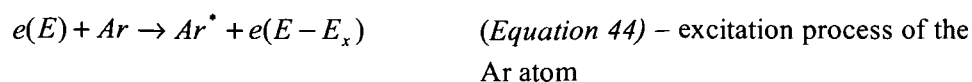
**Figure 20:** Intensity (non-collinear) autocorrelation corresponding to 30fs pulse duration.

### 2.3.3 The Excimer laser

The post-ionization experiments were performed with ArF excimer laser (*Lambda Physik EMG101-104 MSC*), operated at 193nm and  $\tau_{pulse} = 20ns$ . The laser beam is positioned at a distance of  $\approx 2mm$  above the target surface.

The name “excimer” gains its roots from the compilation “excited dimer”. The excimers exists only in excited states for a limited time, in their ground state they are unstable. The excimers are formed by applying high voltage to the gas mixture.

The reactions which occur during the excitation are:



$Ar^+ + F^- + Ar \rightarrow (Ar^+F^-)^* + Ar$  (Equation 45) – formation of the excimer molecule

$Ar^* + F_2 \rightarrow (Ar^+F^-)^* + F$  (Equation 46) – reaction between excited Ar atom and its Fluorine donor

$e + F^- \rightarrow F + 2e$  (Equation 47) -generation of an additional electrons due to knock out of extra electrons from the fluorine atom.

$e(E) + (Ar^+F^-) \rightarrow Ar + F + e(E + E_{excimer})$  (Equation 48) - resulting dissociation process of the excimer after its formation

We was using a gas mixture of Ar, F, He. The typical gas fill comprises 0.1-0.3% of halogen diluted in He (97%) and 2-3% rare gas (Ar).

The excitation of the rare gas atom (Ar) results in transition of an electron, located in the outer shell from the nucleus, to next higher energy level. Thus the excited argon atom very easily reacts with the Fluorine.

The pumping in this type of lasers is achieved by high-voltage sources or discharge. The present excimer laser utilizes a Thyatron - the main high voltage switch in the laser head. It is a grounded cathode thyatron.

The post-ionization experiments were performed at 30-60mJ output energy. The laser operates at 16Hz pulse repetition rate. The ArF excimer laser has single photon energy in the order of 6.4 eV.

## 2.4 The SNMS method

The method of Laser Secondary Neutral Mass Spectroscopy (LSNMS) is established since early 1980s. In our research we have used the post-ionization method because of the high sensitivity of the detection and analysis of molecules and atoms.

In the present experiment the technique incorporates two steps: ablation of neutral molecules, atoms from the sample surface and post-ionization of the ablated particles with UV, 193nm ArF excimer laser pulses. This separate mode of exploring the method allows the ablation and the post-ionization steps to be optimized separately thus is achieved maximum sensitivity. In this study the method is applied for analysis of polypeptides and proteins.

It can be distinguished three types of photon excitation which lead to ionization of neutral atom or molecule: Single Photon Ionization (SPI), Resonant Multiphoton Ionization (RMPI) and Nonresonant Multiphoton Ionization (NRMPI).

The Single Photon Ionization (SPI) means that the absorption of one photon will be enough for promoting the electron into the ionization continuum.

When the atomic system is brought into the ionic continuum through simultaneous absorption of several photons the ionization process is called Multiphoton Ionization. Depending of the spectral parameters of the radiation and of the atomic states two cases of MPI can be distinguished. The Resonant Multiphoton Ionization (RMPI) is a multi-step process where an electron is promoted to intermediate electronic state through absorption of a photon and the subsequent absorption of a photon of the same energy initiates the ionization.

The typical power density required for RMPI is in the order of  $10^6 \text{ W/cm}^2$ . The neutrals are intersected by a pulsed laser beam of high flux density of photons.

The other case of MPI is the NRMPI, and can be encountered when the multiphoton absorption occurs even when the electronic intermediate state is not excited. Power densities exceeding  $10^9 \text{ W/cm}^2$  are required to achieve saturation in the ion yield. High power pulsed ultra violet lasers are used for this type of ionization.

The majority of the emitted particles (sputtered due to energetic ion bombardment or ablated, desorbed due to interaction with laser beam) from a solid surface are neutral in charge but it also exists a small proportion of positively and negatively species.

The crucial parameter for the post-ionization experiments is the energy necessary for ionization of the neutral species. The ionization efficiency depends strongly from the precise timing of the laser pulses and from the geometrical overlap of the focus of the post-ionizing laser beam with the emitted particle cloud.

## Chapter 3

### 3. Results and Discussion

In this chapter the obtained experimental results will be presented and the underlying reaction mechanism will be discussed. The primary aim was to analyze the laser - induced ablation process and to compare the results obtained under variation of different parameters.

The main difficulties were met in the identification of the ablation products due to the complexity of the examined biological material. Special emphasis is put on the post-ionization experiments since it is expected to give a more complete characterization of the ionization channel.

Successful efforts have been attained to examine many organic biological molecules with matrix-assisted laser desorption ionization (MALDI) which produces intact molecular ions. In MALDI analysis the analyte is crystallized with large molar excess of matrix compound. The matrix serves to efficiently absorb the laser light and thus causing the vaporization of the analyte [lewis00], [medzih00], [schiller00], [sarver00], [counter03].

The development of the new class, high power, ultra-short lasers the approach of photoionization of neutral species with ultra-short pulses is a topic of considerable interest due to the unique ionization mechanism. In the current research study the femtosecond laser mass spectrometry is applied to the analysis of laser ablated polypeptides and proteins since they represent considerable part of the organic composition of the biological samples and the examination of them is prerequisite for understanding of the biological function in molecular level.

It is of main importance to succeed to establish efficient ionization of these organic molecules with minimal fragmentation. In some biological systems the fragmentation is unavoidable due to the fast internal conversion and dissociation mechanisms. In order to determine the mechanism of fragmentation the post-ionization mass spectra of the organic molecules at 193 nm and 800nm was examined.

Several important parameters have been shown to influence the ablation process: the pulse duration, the laser wavelength, the laser fluence. To gain more insight of the influence of the laser intensity on the yield of the ablated ions, intensity dependence measurements were performed.

Of special interest is to compare the degree of fragmentation which is observed with ion beam desorbed and ablated with nanosecond pulses molecules with that obtained with femtosecond ablation.

Finally, ionization yields of various photoproducts are compared to ionization yields with SIMS to demonstrate the analytical capabilities of both approaches.

### 3.1 Optical properties of biological tissue

Laser light propagation in biological tissue is dependent on the specific optical properties of the media like *absorption, scattering, reflection*.

The absorption of light by molecule is associated with the promotion of the electron from the ground state to one of higher energy.

However: *"a given molecule can only absorb photons of certain wavelengths because, as is required by the law of conservation of energy, the energy difference between the two states must exactly match the energy of the absorbed photon"*.

The **Beer-Lambert law** describes the amount of light which is absorbed by the media at certain wavelength:

$$A = \log \frac{I_0}{I} = \epsilon cb \quad (\text{Equation 49})$$

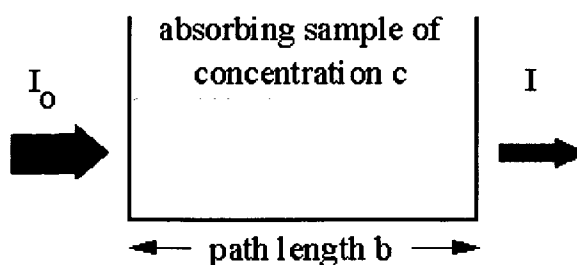


Figure 21: Beer-Lambert absorption law.

$A$  - absorbance  
 $I_0$  - incident intensity  
 $I$  - transmitted intensity  
 $c$  - molar concentration of the sample  
 $\epsilon$  - molar extinction coefficient

*b*- length of the light path

The optical absorption is a function of wavelength and chromophore. The chromophores are absorber substances in the tissue. They represent a group of atoms in the molecule that includes an unsaturated chemical group (for example C=C), the chromophore is responsible for the color of the compound.

Organic molecules show strong absorption in the UV range, in contrast wavelengths between 600 and 1200nm (red and near infra-red) are weakly absorbed and penetrate deep in the tissue. Amino acids show strong absorption in the UV. Water, fat and hemoglobin absorbs intensively in the near IR. The absorption spectrum of water is high from 200nm-935nm, it drops beyond 1000nm. For lipids the absorption is strong at 930nm.

Optical scattering occurs when the direction of the incident rays is changed by the molecules present in the tissue. The consequence of the scattering is the effect which it imposes on the properties of the laser beam, after propagating a certain length (few mm in tissue) the laser beam changes its characteristics: the coherence and the collimation, it becomes incoherent and isotropic. Scattering is wavelength dependent.

The optical reflection, determines in what proportion the input beam will penetrate in the tissue. This knowledge of the reflectivity is necessary because it can reach high values, for example the argon beam is reflected 40%-50% from the skin.

### 3.1.1 Composition of the biological samples

It is very important to have knowledge of the composition of the ablated material, in order to make chemical and physical analysis. The content of the ablated flux of material varies in correspondence to the laser wavelength, pulse duration, repetition rate of the pulses, absolute laser fluence. In our experiments measurements were performed on examining biological targets such as tooth, bones.

The structure of human tooth contains several layers (*Figure 22*).

Enamel - 95% hydroxyapatite,  $Ca_{10}(PO_4)_6(OH)_2$ , 4% water, 1% organic matter. The crystal lattice can contain some impurity like  $Cl^-$ ,  $Na^+$ ,  $K^+$ ,  $F^-$ ,  $Mg^{2+}$ . The hydroxyapatite is a mineralized compound.

Dentin - it contains about 70%  $Ca_{10}(PO_4)_6(OH)_2$ , 20% organic matter (collagen fibers), 10% water. The internal structure of dentin is with small canals which are essential for the growth of the tooth.

Pulp - contains only blood vessels, nerve fibers, cells and is not mineralized. The pulp is



connected by the root canal with the peripheral blood vessels.

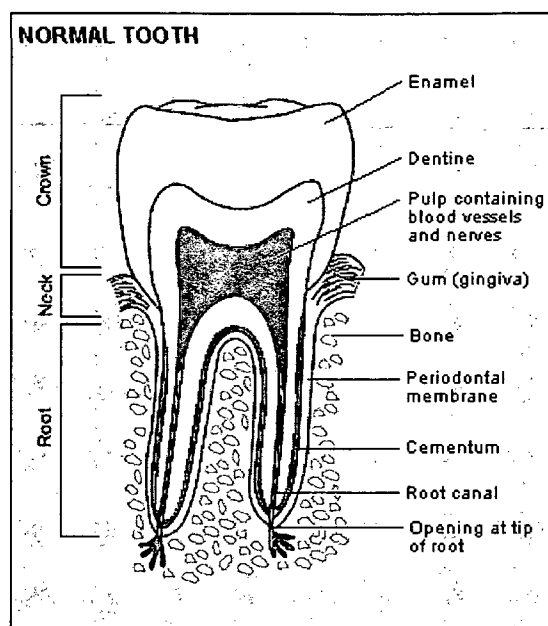


*Figure 22: Structure of human tooth.*

In summary, the inorganic matter of the tooth is represented mainly by the hydroxyapatite crystal, the organic matter consists of collagen fibers.

Bone main composite elements are:

#### Inorganic

50-60% Hydroxyapatite  
15-20% Water  
5% Carbonates  
1% Phosphates

#### Organic

20% Collagen  
1-2% Proteins

As it is seen from above the organic matter (collagen fibers) in the tooth and bone samples represents a considerable part of their composition. Collagen occurs in all multicellular animals and it belongs to the family of proteins. It is organized into insoluble fibers and is the main stress-bearing component of connective tissues such as bone, tooth, cartilage and the fibrous matrices of skin and blood vessels. The molecular mass of one molecule of collagen is  $\approx 285kD^*$ . The molecule length is  $\approx 3000\text{\AA}$  and it

consists of three polypeptide chains wound together in a tight triple helix. Collagen has an amino acid composition, almost one third of its residues are Gly; another 15 to 30% of its residues are Pro and 4-hydroxyproline (Hyp) (Figure 23). There is very little Cys or Trp present.

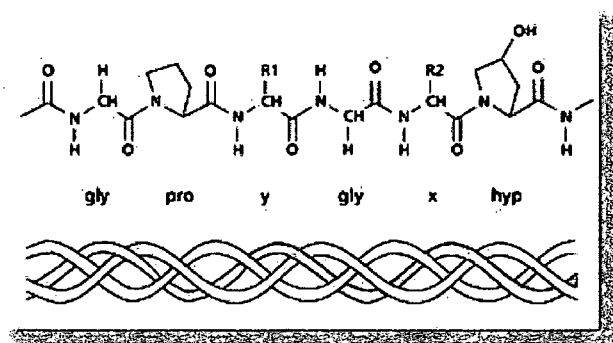


**Figure 23:** Example of collagen triple helix.

The primary structure of collagen has a frequent repetitive pattern, Gly-Pro-Hyp (or Lys or Hyl).

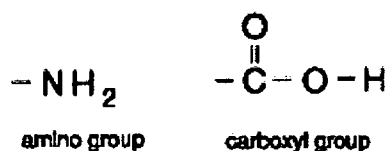
After the synthesis of the polypeptide chain, some of the amino acids residues became modified. Examples of such kind of modified amino residues are 4-hydroxyproline and 5-hydroxylysine, which are the main constituents of the molecule of collagen.

There exist different types of collagen, the most abundant are:

Type	Chain composition	Distribution
I	$[\alpha 1(I)]_2\alpha 2(I)$	Skin, bone, tendon, blood, vessels, cornea
II	$[\alpha 1(II)]_3$	Cartilage, intervertebral disk
III	$[\alpha 1(III)]_3$	Blood vessels, fetal skin

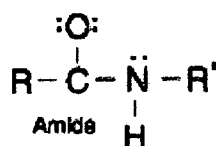
**Table 5:** Different types of collagen and its distribution in tissue.

The proteins consist of one or several peptide chains. The amino acid units in the protein molecule are connected through a peptide bond. The amino acids contain an amino group and a carboxyl group (*Figure 24*).



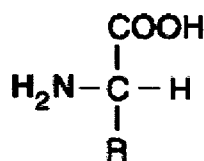
**Figure 24:** Example of amino group and carboxyl group.

They bond to each other in the form of an amide (*Figure 25*).



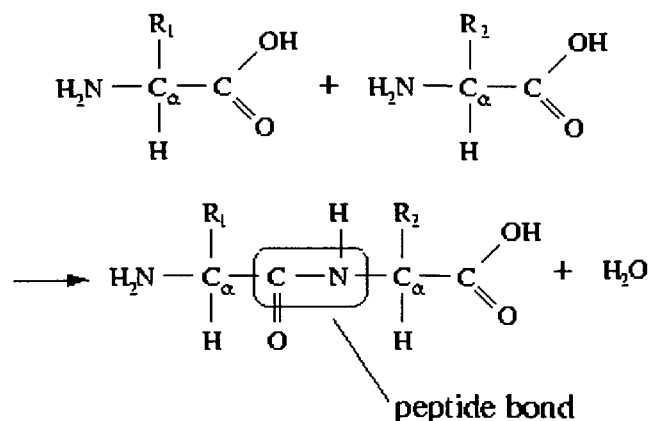
**Figure 25:** Amide bond; here the symbol *R* is a free radical, it is a general symbol to assign when the atom or molecule has an unpaired electron.

The general form of Amino acids is shown in *Figure 26*:



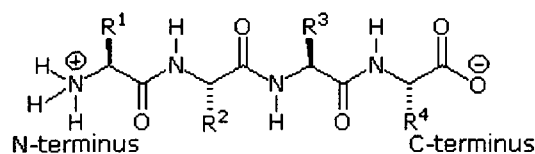
**Figure 26:** Basic form of amino acid.

The  $\alpha$ -amino acids polymerize through the elimination of water molecule (*Figure 27*).



**Figure 27:** Peptide bond linking two amino acids.

The resulting CO-NH linkage is called peptide bond. Proteins which are composed of several amino acids are called di-, tri- ... polypeptides.

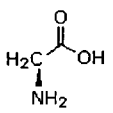
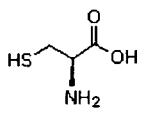
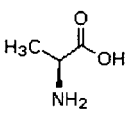
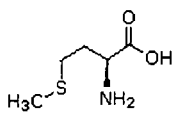
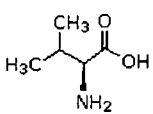
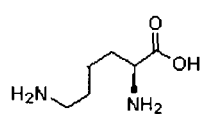
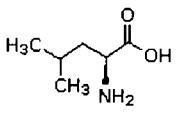
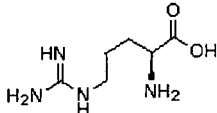
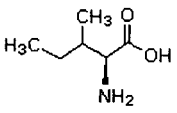
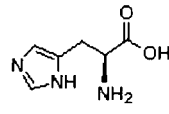
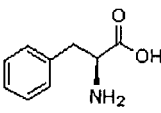
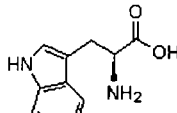
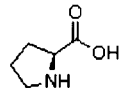
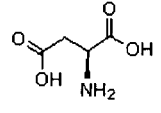
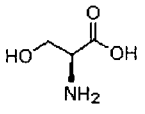
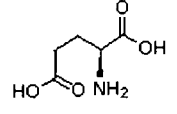
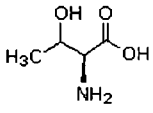
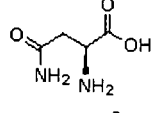
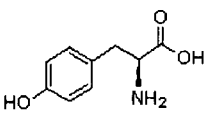
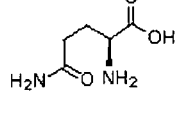


**Figure 28:** Example of polypeptide backbone.

One end of a polypeptide chain terminates in an amino acid residue which has a free –NH group, the other end terminates in amino acid residue with a free –CO group. These two groups are called respectively *N-terminal* and *C-terminal* residues (Figure 28).

The spectroscopic properties of the amino acids results in the ability of absorbing or emitting electromagnetic energy at various wavelengths. All amino acids do not absorb light in the visible spectrum. Furthermore, almost all amino acids (with exception of tryptophan, tyrosine and phenylalanine) absorb in the infrared range. The amino acids tryptophan, tyrosine and phenylalanine are absorbing in the UV.

All proteins are composed of 20 amino acids which can be distinguished by the R - functional group. Some of the “standard” amino acids are listed in (Table 6).

Name	Formula	Abbreviations	Name	Formula	Abbreviations
Glycine		Gly G	Cysteine		Cys C
Alanine		Ala A	Methionine		Met M
Valine		Val V	Lysine		Lys K
Leucine		Leu L	Arginine		Arg R
Isoleucine		Ile I	Histidine		His H
Phenylalanine		Phe F	Tryptophan		Trp W
Proline		Pro P	Aspartic Acid		Asp D
Serine		Ser S	Glutamic Acid		Glu E
Threonine		Thr T	Asparagine		Asn N
Tyrosine		Tyr Y	Glutamine		Gln Q

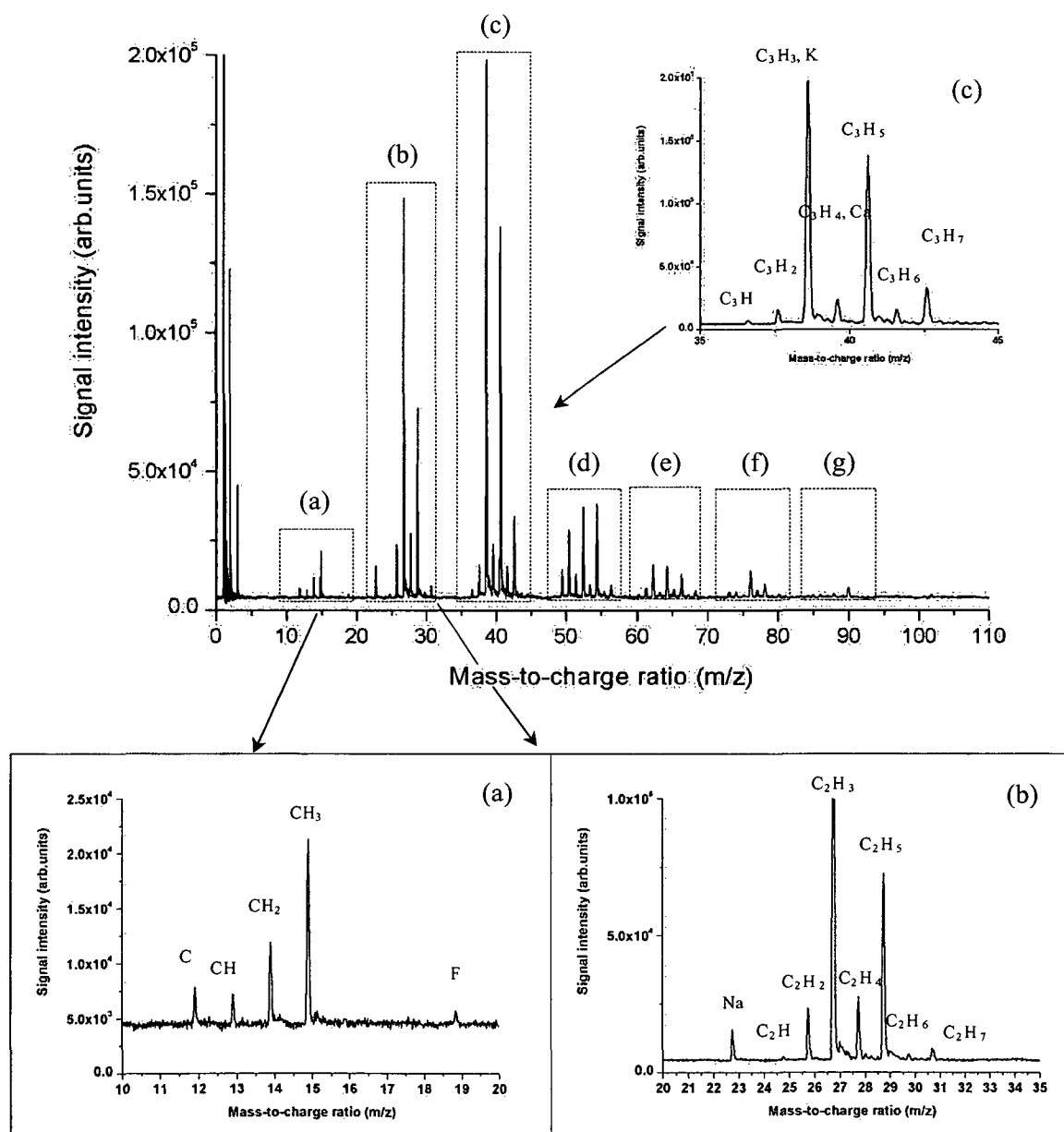
**Table 6:** Structural formulas of the 20 “standard” amino acids of Proteins.

## 3.2 Ultra-short laser ablation mass spectra

Here we examine the ablation mass spectra of bones and tooth with femtosecond laser pulses.

- *Femtosecond laser ablation mass spectra for bone sample.*

These were taken with typical laser ablation intensities of  $I = 5.1 \times 10^{13} \text{ W/cm}^2$ . The time-of-flight mass spectra for bone sample at  $\lambda = 800 \text{ nm}$ , pulse duration  $30 \text{ fs}$  are inserted below in Figure 29.



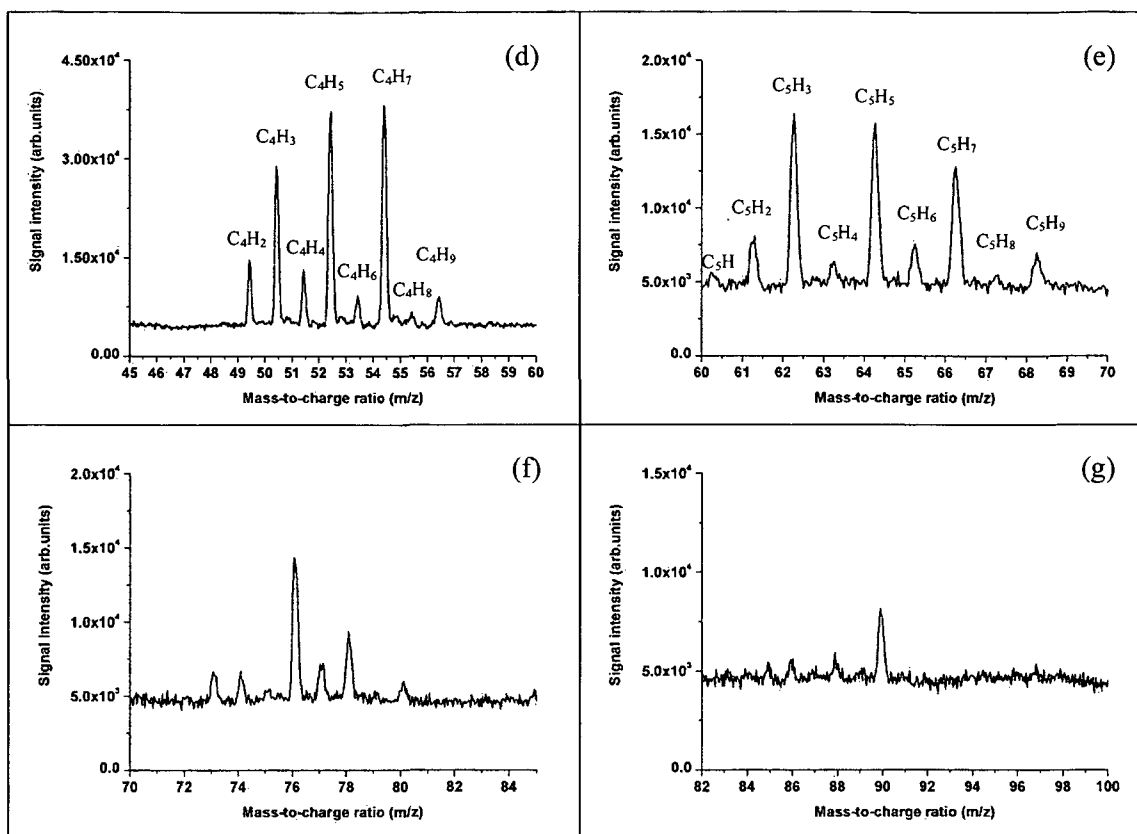


**Figure 29:** ToF mass spectra of laser ablated species of bone sample irradiated with 30fs laser pulses, at  $\lambda=800\text{nm}$  and laser ablation intensity  $I=5.1 \times 10^{13} \text{ W/cm}^2$ .

For ease of the identification each peak group has been expanded. In order to achieve reproducibility of the results, the laser was placed for every measurement on a virgin spot on the sample. From the analysis of all spectra a strong  $H^+$  peak is observed for several laser intensities. As it was outlined in paragraph 3.1.1 that the main composite material of bone is hydroxyapatite ( $\text{Ca}_{10}(\text{PO}_4)_6(\text{OH})_2$ ) and collagen, we are expecting in the obtained spectra to observe the appearance of Ca peak at  $m/z = 40$ , resulting from the interaction of the laser light with the present in the hydroxyapatite structural  $\text{OH}^-$  group (Figure 29c). This interaction breaks the  $\text{OH}^-$  bond releasing  $H^+$  ions and Ca ions. The peaks at  $m/z = 19$  and  $m/z = 23$  can be attributed to  $F^-$  and  $\text{Na}^+$ . Possible fragmentation channel at 30fs is expected to be observed from the breakage of the polypeptide chain of collagen. Furthermore the presence of the residues from the polypeptide chain is confirmed by the fragments which are assigned on (Figure 29b, c, d, e, f, and g) to  $\text{C}_m\text{H}_n$ .





Symbol	Molecular formula	Residue mass	Molecular weight
Alanine (Ala/ A)	$C_3H_7NO_2$	71.04	89.09
Arginine (Arg/ R)	$C_6H_{14}N_4O_2$	156.10	174.20
Asparagine (Asn/ N)	$C_4H_8N_2O_3$	114.04	132.12
Aspartic Acid (Asp/ D)	$C_4H_7NO_4$	115.03	133.10
Cysteine (Cys/ C)	$C_3H_7NO_2S$	103.01	121.15
Glutamine (Gln/ Q)	$C_5H_{10}N_2O_3$	129.04	146.15
Lysine (Lys)	$C_6H_{12}N_2O$	128.09	146.15
Glutamic Acid (Glu/ E)	$C_5H_9NO_4$	129.04	147.13
Glycine (Gly/ G)	$C_2H_5NO_2$	57.02	75.07
Histidine (His/ H)	$C_6H_9N_3O_2$	137.06	155.16
Isoleucine (Ile/ I)	$C_6H_{13}NO_2$	113.08	131.17
Leucine (Leu/ L)	$C_6H_{13}NO_2$	113.08	131.17
Methionine (Met/ M)	$C_5H_{11}NO_2S$	131.04	149.21
Phenylalanine (Phe/ F)	$C_9H_{11}NO_2$	147.07	165.19
Proline (Pro/ P)	$C_5H_9NO_2$	97.05	115.13
Serine (Ser/ S)	$C_3H_7NO_3$	87.03	105.09
Threonine (Thr/ T)	$C_4H_9NO_3$	101.05	119.12
Tryptophan (Trp/ W)	$C_{11}H_{12}N_2O_2$	186.08	204.23
Tyrosine (Tyr/ Y)	$C_9H_{11}NO_3$	163.06	181.19
Valine (Val/ V)	$C_5H_{11}NO_2$	99.07	117.15

**Table 7:** Molecular weight of 20 “standart” amino acids; column 1 contain 3-letter code and 1-letter code of abbreviation for the amino acids; residue mass – portion of a molecule that remains after it has lost its components; molecular weight – ratio of the particle mass to  $1/12^{\text{th}}$  the mass of  $^{12}\text{C}$  atom, dimensionless quantity.

To determine precisely the fragmentation channels it is necessary to know the ionization potentials of the examined species (Table 8). The majority of amino acids for successful ionization require absorption of at least 6 photons at 800nm wavelength. The ionization of Ca requires, corresponding to (Table 8), the absorption of at least 5 photons at 800nm,  $\text{C} \rightarrow 8$  photons,  $\text{Na} \rightarrow 4$  photons.

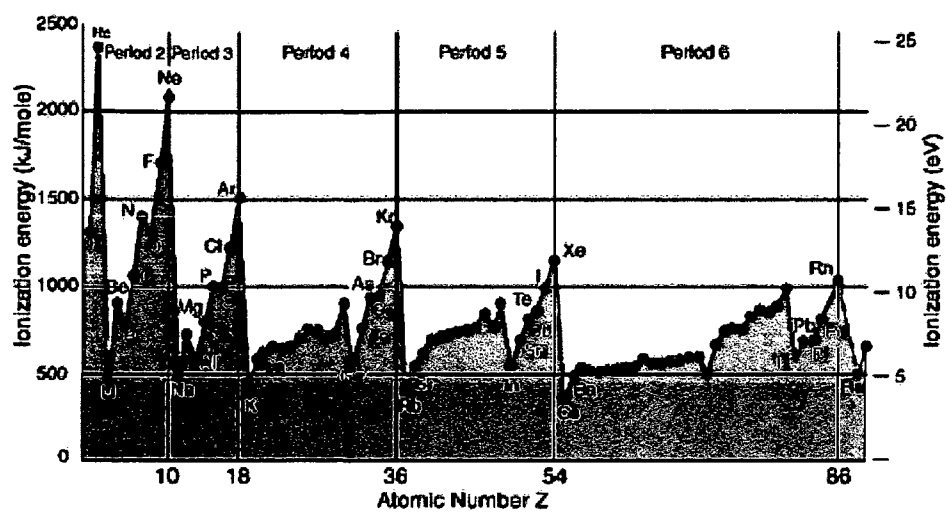
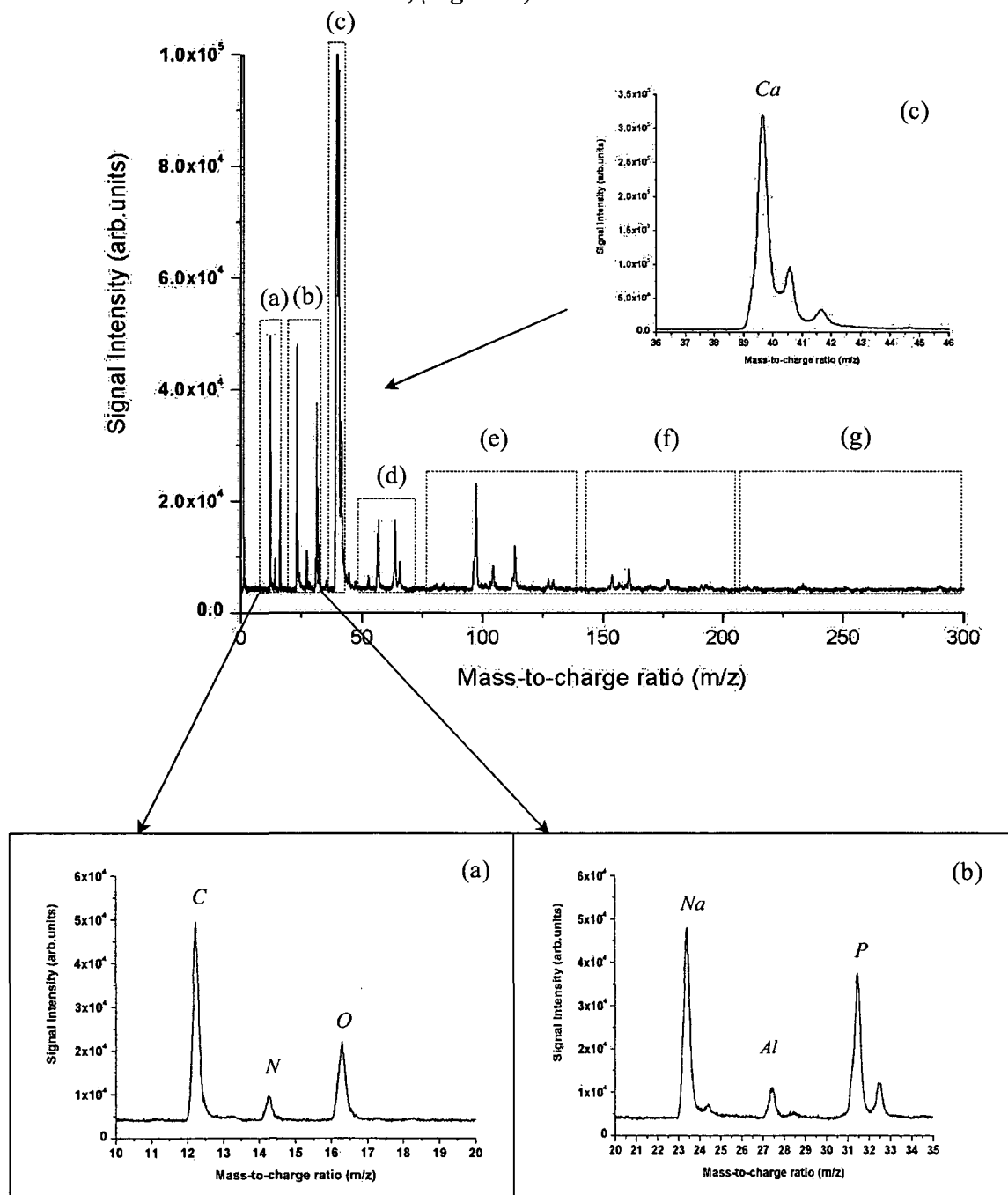
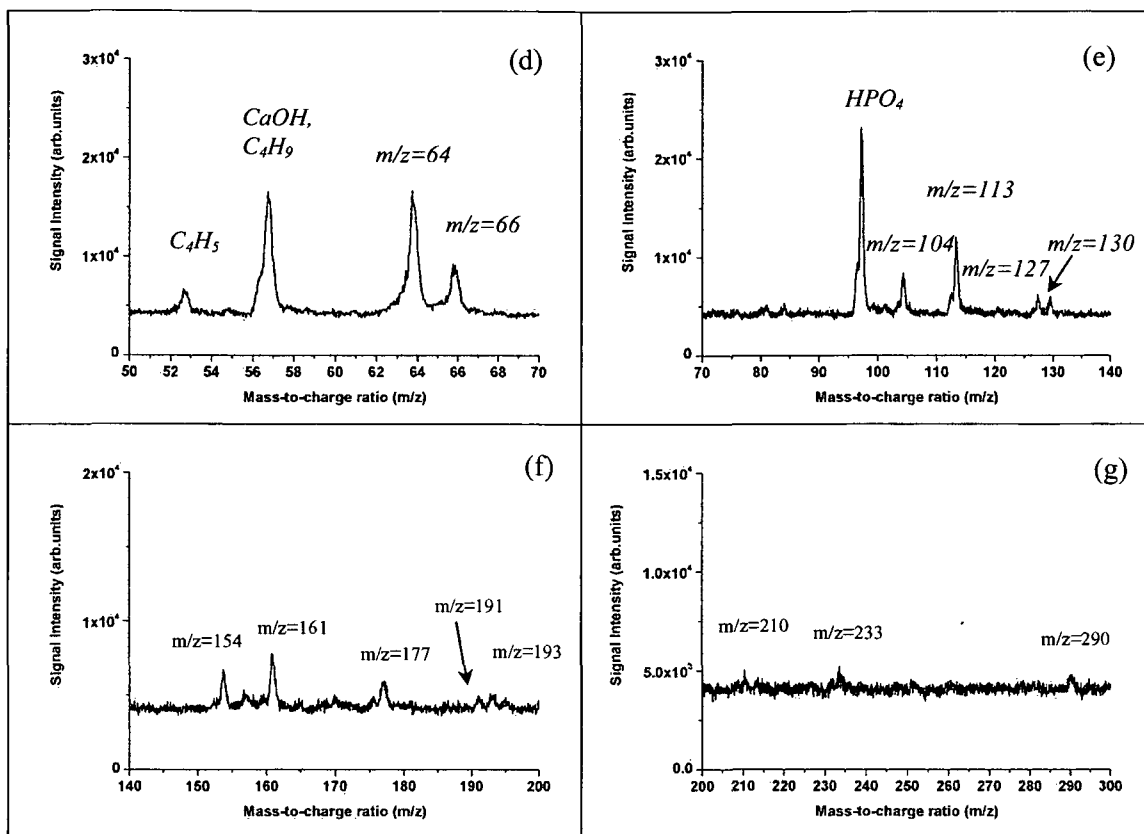


Table 8: Ionization potentials of chemical elements.

- Femtosecond laser ablation mass spectra for tooth sample.

Comparative studies were carried out in order to discover the difference between the behaviors of the laser ablated species from several biological samples. Time-of-flight spectra of human tooth were recorded at  $\lambda=800\text{nm}$ , pulse duration  $30\text{fs}$ , and typical laser intensities of  $I=5.1 \times 10^{13} \text{ W/cm}^2$ , (Figure 31).





**Figure 31:** ToF mass spectra of laser ablated species of tooth sample irradiated with 30fs laser pulses, at  $\lambda = 800\text{nm}$ , and laser ablation intensity  $I = 5.1 \times 10^{13} \text{ W/cm}^2$ .

A strong peak is observed at  $m/z = 40$  in (Figure 31c), indicating the presence of  $Ca$  ion. The regions around the  $Ca$  ion are expanded. Again in the tooth mass spectra as in the bone mass spectra, at  $m/z = 1$  a strong  $H^+$  can be noticed. The peak at  $m/z = 12$  can be attributed to  $C$  ion, at  $m/z = 14$  can be observed the  $N$  ion peak, at  $m/z = 16$  appears the  $O$  ion peak (Figure 31a). On (Figure 31b) can be very clearly distinguished  $Na^+$  and  $P$  ion peaks with the corresponding masses  $m/z = 23$  and  $m/z = 31$ . Furthermore can be observed at  $m/z = 27$  can be attributed to  $Al$  peak resulting from the present impurities in the chamber. The later peak positioned at  $m/z = 57$  can be assigned to  $CaOH$  ion, resulting from the degradation of the hydroxyapatite matrix (Figure 31d). An envelope of peaks at  $m/z = 64$  and  $66$  is evident, confirming the presence of fragments from the polypeptide chain. As it can be clearly seen on (Figures 31d, e, f, g) peaks at molecular masses  $m/z = 104, 113, 127, 130, 154, 161, 177, 191, 193, 210, 233, 290$  are also indicating the presence of fragments from the polypeptide chain with the exception of the

peak at  $m/z = 97$  which can be attributed to  $HPO_4^-$  group, the formation of which is due to the dissociation of the hydroxyapatite matrix.

The data presented here for bone and tooth samples are similar. As a general feature in both mass spectra can be observed high ion yield of  $C_mH_n$  fragments, with exception of the fact that as a contrast to the acquired bone mass spectra, the mass spectra of the tooth sample are suffering from suppressed fragmentation in evidence of which are the masses recorded at  $m/z > 90$ .

More recently a number of authors have performed *MALDI* photoionization measurements of tryptophan employing femtosecond lasers for post-ionization [jia96]. These studies have given a model for fragmentation pattern of tryptophan molecule. As a general observation the difference between the photoionization spectra with femtosecond and nanosecond laser consists mainly in the ionization efficiency. The base peak is expected to appear even at  $m/z = 204$  or  $130$  depending of the ionization fluence and wavelength. *MALDI* photoionization mass spectra at  $266nm$  exhibit fragments at  $m/z = 130, 131, 191$  and  $193$ . Characteristic for tryptophan is the prominent peak  $m/z = 130$  corresponding to the cleavage of the *C-C* bond of the amino acid component [jia 96], [holling97]. In our case it is evident the appearance of the peak at  $m/z = 130$ , and can be attributed to the tryptophan residue.

### 3.2.1 Laser ablation mass spectra at 193nm

- Nanosecond laser ablation mass spectra for bone sample.

To gain further insight into the fragmentation process we performed laser ablation experiments at  $\lambda=193\text{nm}$  on bone and tooth samples at typical laser ablation intensities of  $I=2.5 \cdot 10^8 \text{ W/cm}^2$ . The ablation mass spectrum of bone sample is introduced on Figure 32.

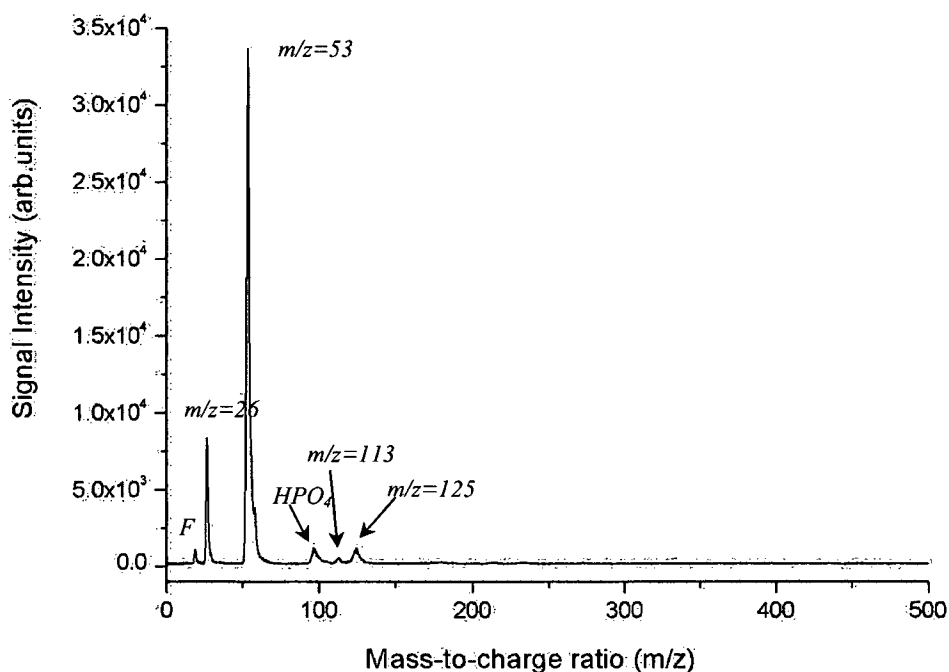


**Figure 32:** ToF mass spectra of laser ablated species of bone sample irradiated with 30ns laser pulses, at  $\lambda=193\text{nm}$  and laser ablation intensity  $I=2.5 \cdot 10^8 \text{ W/cm}^2$ .

The 193 nm spectra on (Figure 32) differ from the spectra presented in paragraph 3.2, (Figure 29) particularly in the degree of fragmentation, which appears to be more suppressed. The base peak in the spectrum appears at  $m/z = 53$ .

It was proposed that the peptide bond of the collagen molecule is chromophore at 193 nm wavelength due to its high molar absorption coefficient in comparison with other

collagen composites such as aliphatic amino acid residues (Figure 33). The first absorption band arises from the  $n \rightarrow \pi^*$  excitation in the amino group at 193nm.

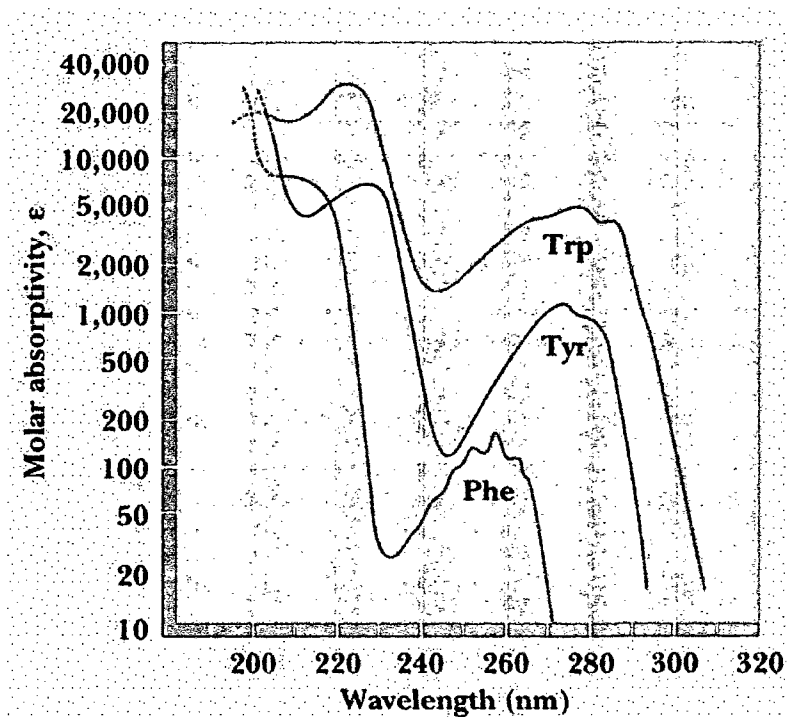


**Figure 33:** UV activity of aromatic amino acids; Phe, Tyr and Trp exhibit high absorption in the range of 240 to 300nm.

The  $\alpha$ -cleavage reaction is proposed to be the dominant reaction in dissociation of peptides [vors99], [sun]. This type of reaction proceeds with elimination of the carboxyl group from peptide. The nitrogen lone pair is donating an electron for the formation of a double bond between the C and N atoms. The cleaving of the bond is initiated from the second donation of an electron from the C-COOH bond. This reaction results in releasing carboxyl radical (Figure 34).

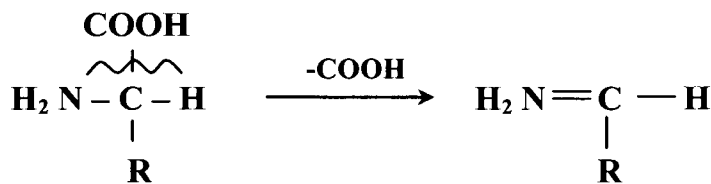


**Figure 34:**  $\alpha$ -cleaving mechanism of peptides.

Another channel of dissociation we can expect to occur through the subsequent fragmentation of amino acids via radical cleavage reaction. This type of cleavage is possible only if the amino acid is released from the surface without fragmentation. According to the ionization potential of the amino acid, removal of an electron from the radical group is possible. When the radicals collide with other molecules they react in way of pairing their unpaired electron. This can happen by extracting an electron from the functional group.

- *Nanosecond laser ablation mass spectra for tooth sample.*

The *UV* ablation spectrum of tooth sample exhibit specific fragmentation pattern, which differs from the spectrum of bone sample analyzed above.

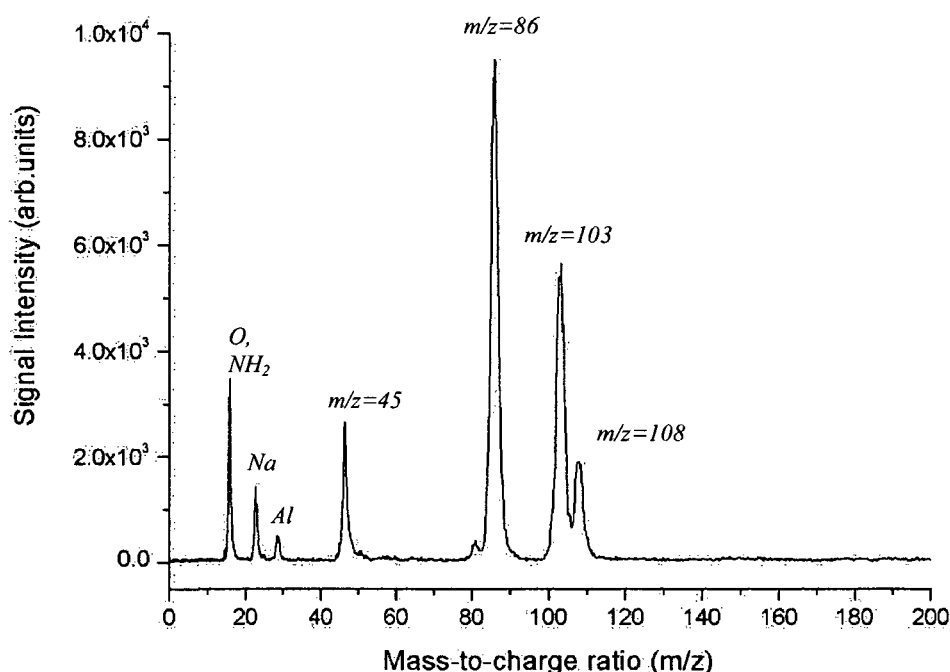


**Figure 35:** ToF mass spectra of laser ablated species of tooth sample irradiated with 30ns laser pulses at  $\lambda=193\text{nm}$  and laser ablation intensity  $I=2.5 \times 10^8 \text{ W / cm}^2$ .

The products of *UV* laser ablation are represented by a diversity of fragments arising from the collagen molecule. In order to establish which amino acids are affected in



collagen with 193nm laser radiation it is necessary to estimate the probability of photochemical damage ( $P_{193}$ ).

$$P_{193} = C_{AA} \times \epsilon_{193} \times \Phi_d, \quad (\text{Equation 50})$$

where  $C_{AA}$  is the content of the amino acid residue,  $\epsilon$  is the molar absorption coefficient and  $\Phi_d$  is the photodecomposition quantum yield. The probability of photochemical damage for the amino acids of human skin collagen is given in the table below.

Amino acid	$C_{AA}$ (%)	$P_{193}$
Gly	33	4.7
Pro	13	2.5
Ala	11	2.5
Hyp	9	1.3
Glu	7	<2.6
Arg	5	10.0
Asp	5	<0.2
Ser	4	1.2
Lys	3	4.8
Thr	2	0.8
Trp	2	37.6
Leu	2	0.6
Val	2	0.6
Phe	1	22.5
Ile	1	
Met	0.6	2.2
Hyl	0.6	
His	0.5	6.7
Tyr	0.3	13.5

**Table 9:** column 2-amino acid content in human skin collagen, column 3-probability of photochemical damage [from nik 99].

From the data presented in (Table 9) can be concluded that the primary target for photodecomposition at 193nm are the Tryptophan, Tyrosine, and Phenylalanine [nik99].

The fragmentation pattern exhibit fragments with  $m/z = 16$ , which we attribute to  $O$ ,  $m/z = 23 \rightarrow Na$ . At  $m/z = 27$  again is present a small peak from  $Al$  impurity which

disappears after. The mass spectrum on (Figure 35) exhibits a clear peak at  $m/z = 86$  which can be attributed to the fragment decarboxylated ion from the leucine amino acid. The  $m/z = 45$  can be assigned to the fragment  $\text{COOH}$ .

The general conclusion from the analysis of both spectra from bone and tooth sample at  $193\text{nm}$ , is that in both cases the presence of organic compounds are dominating the spectra. Furthermore, comparison of time-of-flight mass spectra for two biological samples reveals that fragments with higher molecular masses are dominating the spectra. Smaller amount of fragmentation is observed for the tooth mass spectra.

### 3.2.2 SIMS mass spectra

Comparison will be made of the mass spectra obtained with laser ablation and those obtained with  $9\text{KeV Xe}^+$  ion beam desorbed particles from biological samples. Results from the ToF measurement are shown in (Figure 36).

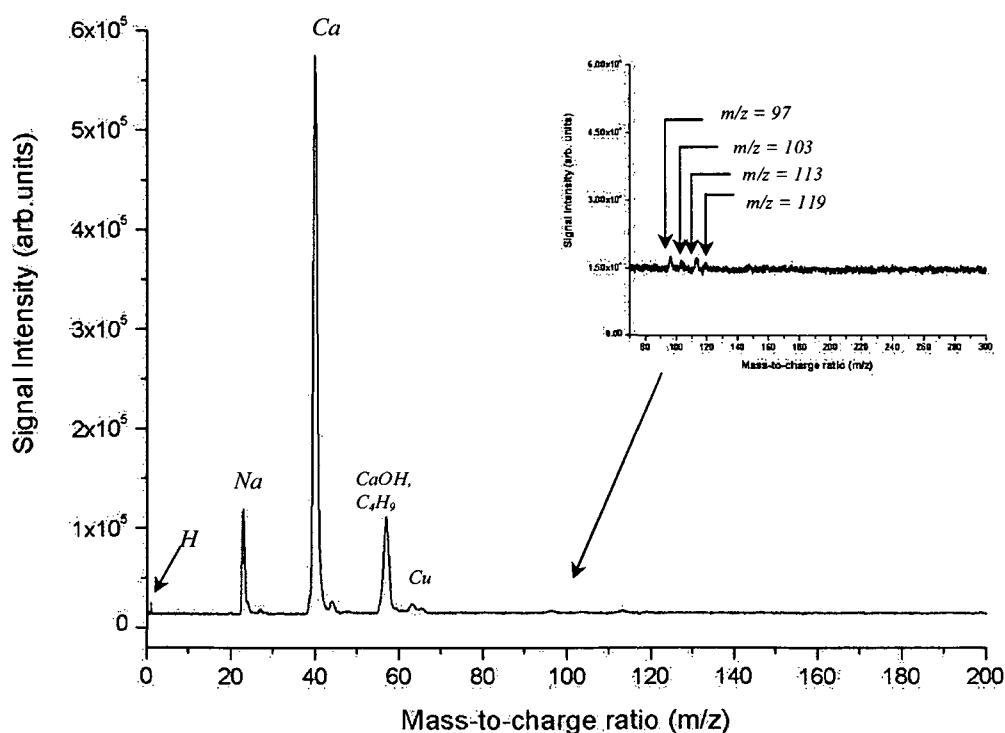


**Figure 36:** ToF SIMS mass spectra of bone sample produced by  $9\text{kV Xe}^+$  ions bombardment. The spectrum is averaged over 10000 spectra.

The SIMS mass spectra of bone sample exhibit dominating peak of  $\text{Ca}^+$  ion at  $m/z = 40$ , which is also observable at previously analyzed mass spectra. Low mass ions at  $m/z = 1, 23$  are present in the spectra. The peaks at  $m/z = 63, 65$  do not originate from the biological sample, they are attributed to  $\text{Cu}$ , this compound is used in the  $\text{UHV}$  chamber in order to prevent charging of the organic sample. Mass fragments which we attribute to peptide fragmentation appear at  $m/z = 97, 103, 113, 119$ .

On the next (Figure 37) an example of SIMS mass spectra acquired from tooth sample are shown.

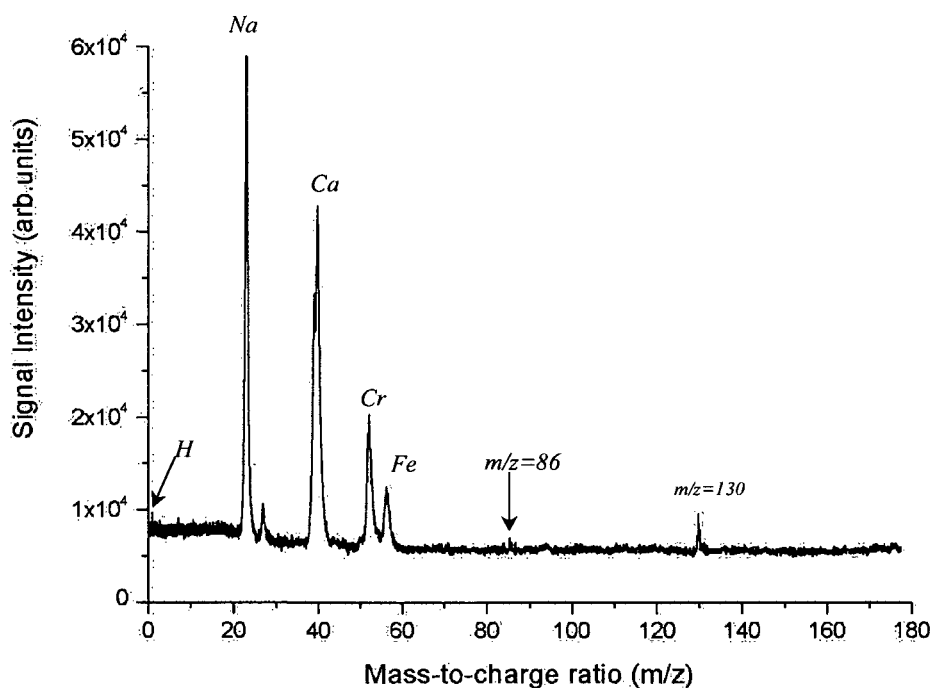


**Figure 37:** ToF SIMS mass spectra of bone sample produced by 9kV  $\text{Xe}^+$  ions bombardment. The spectrum is averaged over 10000 spectra.

Again in the low mass region are present ions of  $m/z = 1, 23, 40 \rightarrow \text{H}, \text{Na}, \text{Ca}$ . The masses which appear at  $m/z = 27, 52, 56$  are common in this spectra regardless of the target material. Mass fragments which can be attributed to the amino acid leucine are observed at  $m/z = 86$  and  $130$ .

It is interesting to compare the distribution of molecular fragments obtained with laser ablation at 800nm and 193nm to those with SIMS.

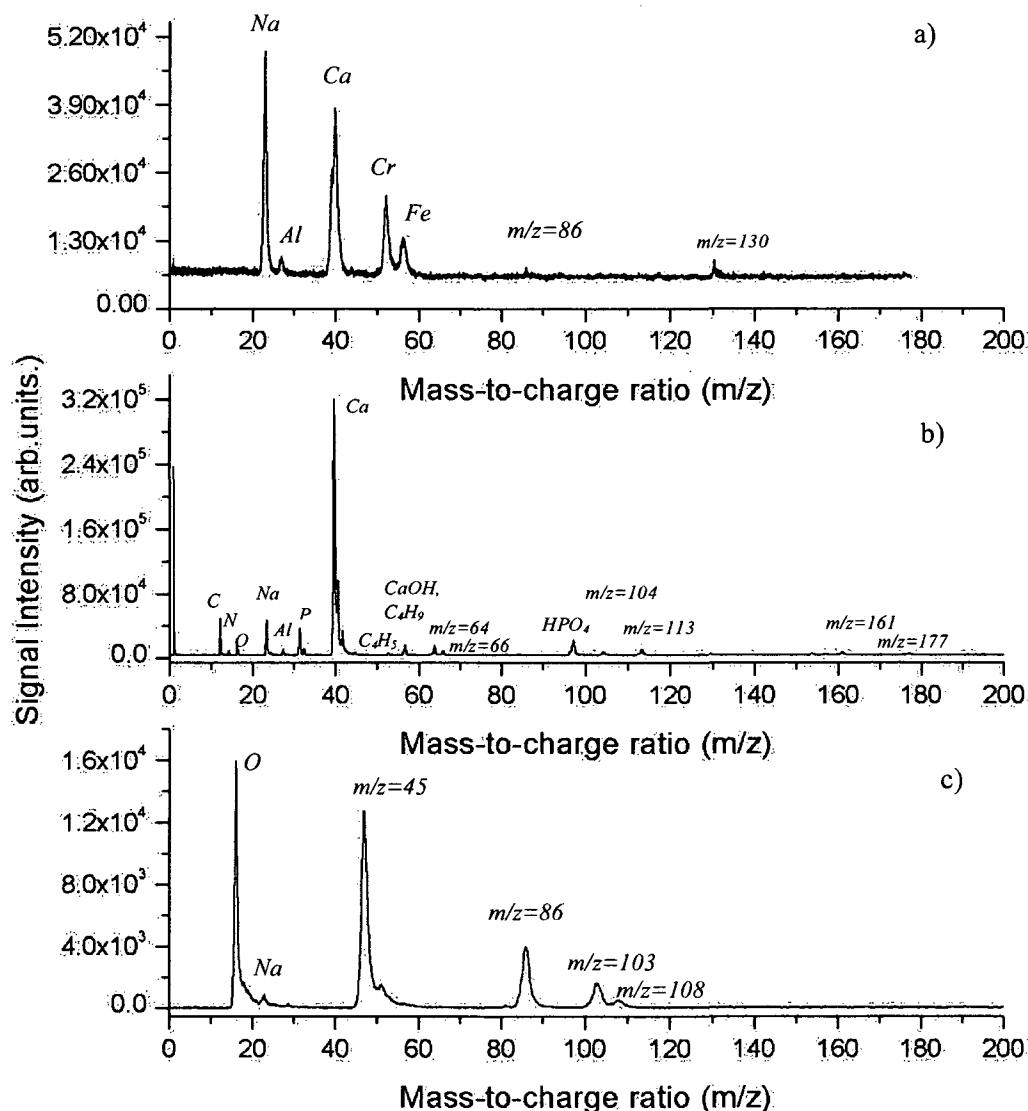


**Figure 38:** Comparison between laser ablation mass spectra of tooth sample and SIMS from tooth sample: a) SIMS; b) Femtosecond laser ablation mass spectra at  $\lambda=800\text{nm}$ , pulse duration 30fs and  $I=5.1 \times 10^{13} \text{ W/cm}^2$ ; c) Nanosecond laser ablation mass spectra at  $\lambda=193\text{nm}$ , pulse duration 30ns and  $I=2.5 \times 10^8 \text{ W/cm}^2$ .

As a result from the analysis of the Laser ablation mass spectra and *SIMS* mass spectra, can be concluded:

1. The laser ablation (800nm) ion spectra of bone and tooth sample shows a series of hydrocarbon peaks indicating the onset of considerable fragmentation. In comparison to this in the laser ablation (193nm) ion spectra and in the *SIMS* mass spectra of bone and tooth sample the degree of fragmentation is much lower, however the detection of higher mass fragments is negligible.

2. The fragmentation pattern, in the laser ablation at 800nm and in *SIMS* mass spectra for both samples, exhibit the  $Ca^+$  ion, this is not observable for the mass spectra obtained at 193nm. The  $Ca^+$  ion peak is surrounded in all spectra by a moiety of low mass ion peaks of *H, C, N, O, Na, P, K*, and low mass ion fragments such as *COOH, C<sub>n</sub>H<sub>m</sub>*. Mass fragments that are unique to the peptide chain are observed in the higher mass range.

3. Most prominent are the mass fragments appearing in the laser ablation mass spectra at 800nm of tooth sample at  $m/z > 130$  (observed in the laser ablation ion mass spectra of tooth sample) which indicates the ability of successful ablation of molecular moiety with suppressed fragmentation.

A more detailed analysis of the degree of fragmentation as a function of laser power density at 800nm and 193nm will be presented in the following paragraph.

### 3.3 Laser intensity dependence measurements

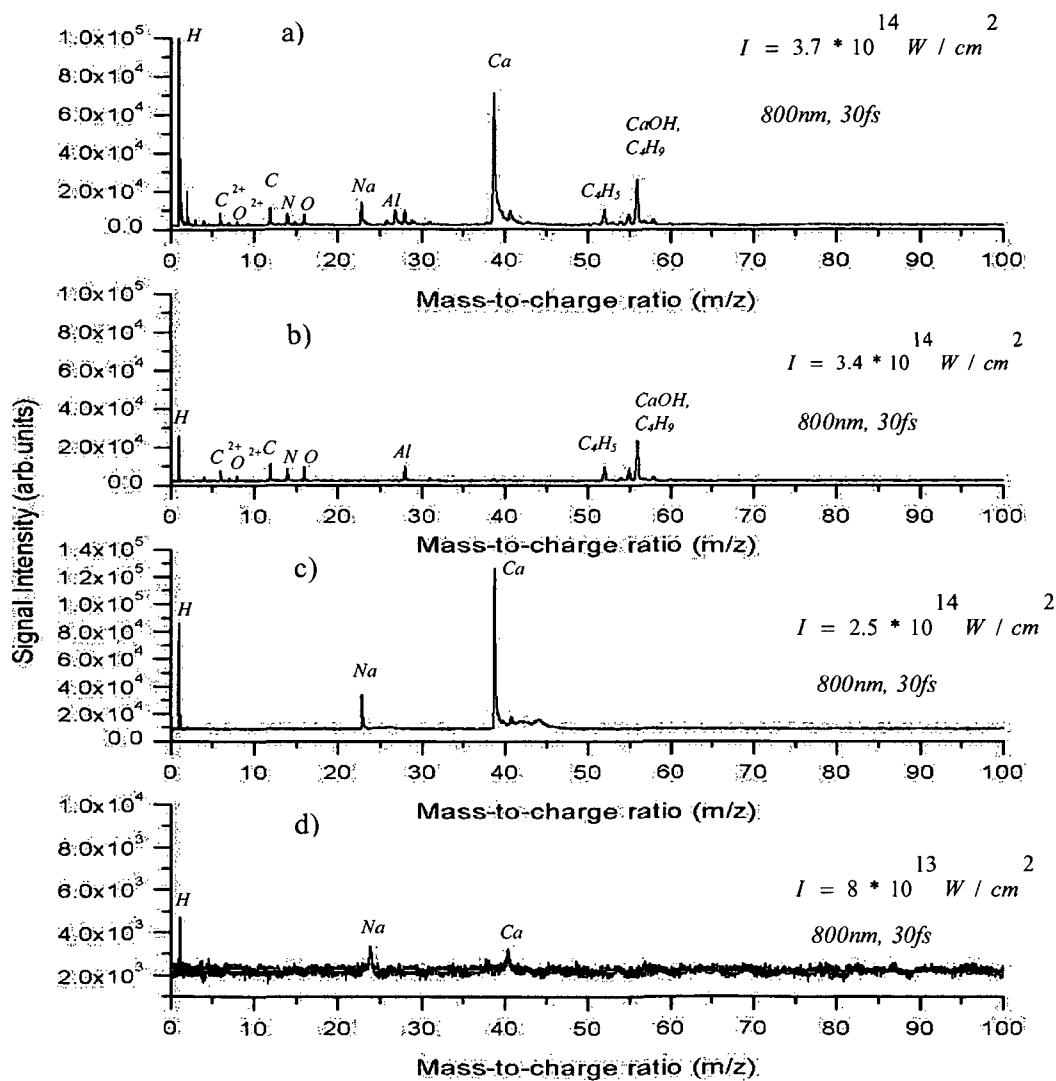
It is valuable to examine the effect of laser power density on fragmentation efficiency. For this we have examined the intensity of the  $m/z = 1, 12, 16, 23, 27, 31, 39, 40$  peaks for different ablation power densities at 800nm and 193nm wavelength.

In *Figure 39* the change of the mass spectra of ablated ions from bone sample by increasing laser power density is shown. For lower laser intensities ( $8 \cdot 10^{13} - 2.5 \cdot 10^{14} \text{ W/cm}^2$ ) the overall fragmentation pattern comprises only *H, Na* and *Ca* ion peaks (*Figure 39c, d*). In addition, the yield of atomic fragments was higher at low ablation intensity. As the ablation intensity increases ( $3.4 \cdot 10^{14} - 3.7 \cdot 10^{14} \text{ W/cm}^2$ ) a shift in ion abundance toward lower mass was typical, multiply charged species of *C, N*, and *O* ions ( $C^{2+}, C^{3+}, N^{2+}, N^{3+}, O^{2+}, O^{3+}$ ) have been observed (*Figure 39a, b*). At higher intensities the individual profiles of the  $C_nH_m$  groups are registered.

An optimum intensity for laser ablation is desirable to produce an amount of intact molecules with minimal internal excitation which can lead to dissociation. In this experiments optimum laser power densities for laser ablation were in the order of  $1.3 \cdot 10^{14} \text{ W/cm}^2$ .

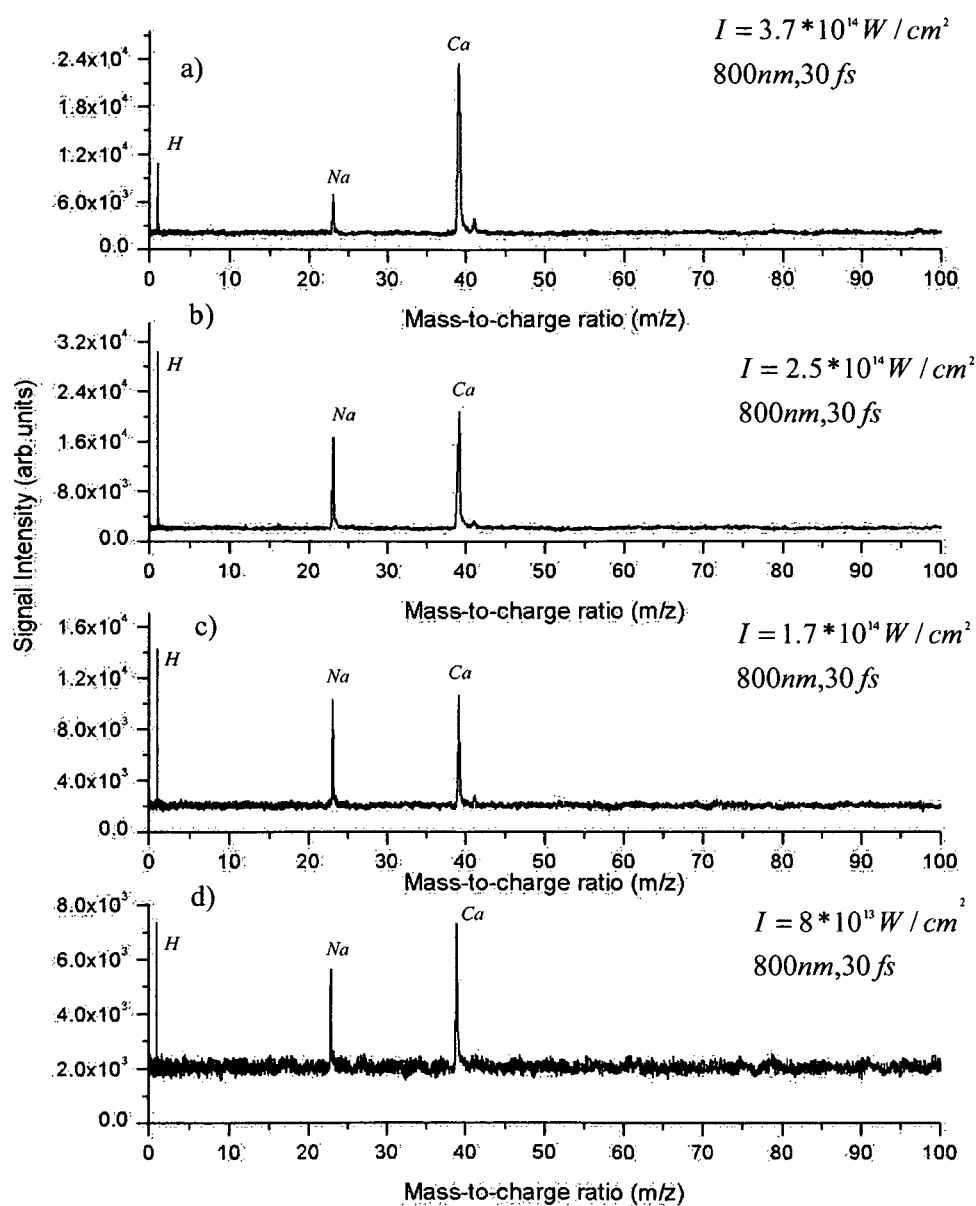
At this point have to be outlined that the fragmentation patterns depend strongly on the spot on the biological the sample which was irradiated. Due to the non-homogeneity in the distribution of the different compounds in the sample, was observed that the mass spectra exhibit differences in dependence from the ablation spot. This suggests that the ablation laser was positioned at some spots which exhibit a higher content of organic compound and as a result we detect different distribution of the mass fragments.

- *Femtosecond Laser intensity dependence for bone sample*



**Figure 39:** Comparison of ToF mass spectra of laser ablated species of bone sample over range of ablation intensities ( $10^{13} - 10^{14} \text{ W/cm}^2$ ) at  $\lambda = 800\text{nm}$ .

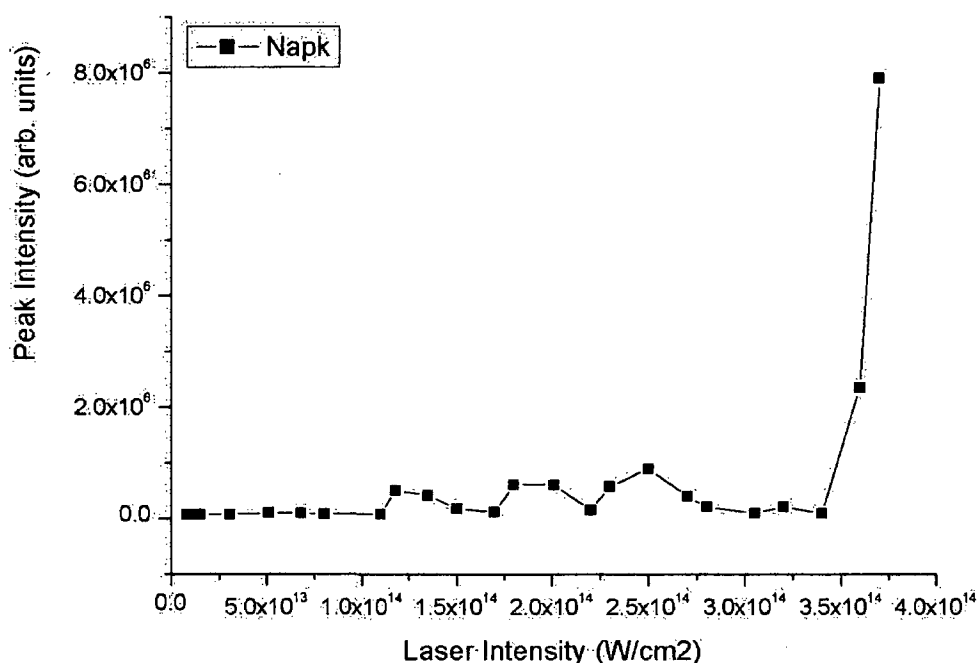
- Femtosecond laser intensity dependence for tooth sample.



**Figure 40:** Comparison of ToF mass spectra of laser ablated species of tooth sample over range of ablation intensities ( $10^{13} - 10^{14} \text{ W / cm}^2$ ) at  $\lambda=800\text{nm}$ .

In Figure 40 examples of laser ablation mass spectra for tooth at four different laser power densities are shown. As a contrast to the spectra on Figure 39, the data taken at 800nm from tooth sample do not exhibit an extensive fragmentation. The peaks at  $m/z=23$  and  $m/z=40$  are dominating the spectra over the whole range of intensities from  $8 \cdot 10^{13} \text{ W/cm}^2$  –  $3.7 \cdot 10^{14} \text{ W/cm}^2$ . For fs ablation, the ablation threshold of tooth sample is  $3.05 \cdot 10^{13} \text{ W/cm}^2$ . At the highest laser power density the peak intensity of  $m/z=40$  raises four times.

The ion signal for each species is obtained by integration of the corresponding ToF mass spectrum. On Figure 41, Figure 42, Figure 43, Figure 44 are presented the ablation signals from bone sample as a function of the laser intensity for low mass fragments. At each laser intensity a new spot on the sample was chosen and the signal was averaged over 5000 spectra. For 800nm, 30fs pulses the ablation threshold for bone sample is about  $5.3 \cdot 10^{13} \text{ W/cm}^2$ .





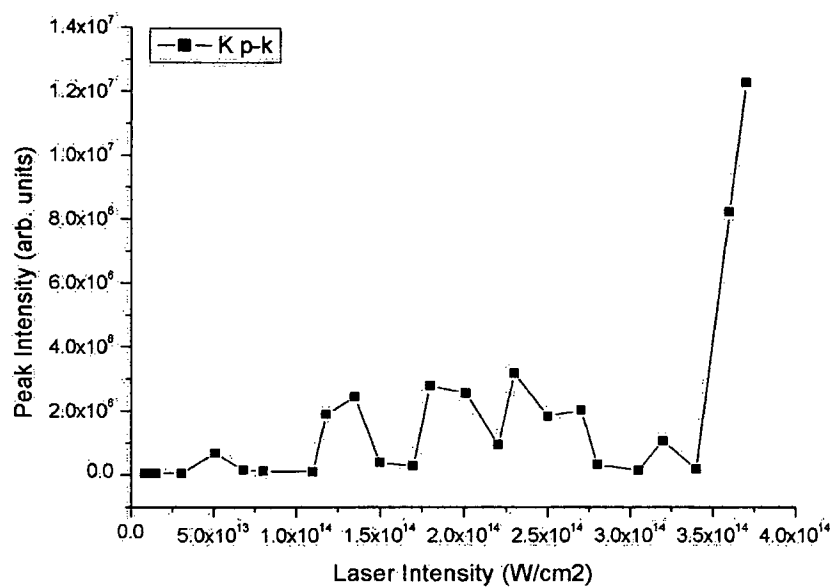


**Figure 42:** Intensity of K ion peak signal of bone sample at various laser power densities with  $\lambda=800\text{nm}$ , 30fs ablation.

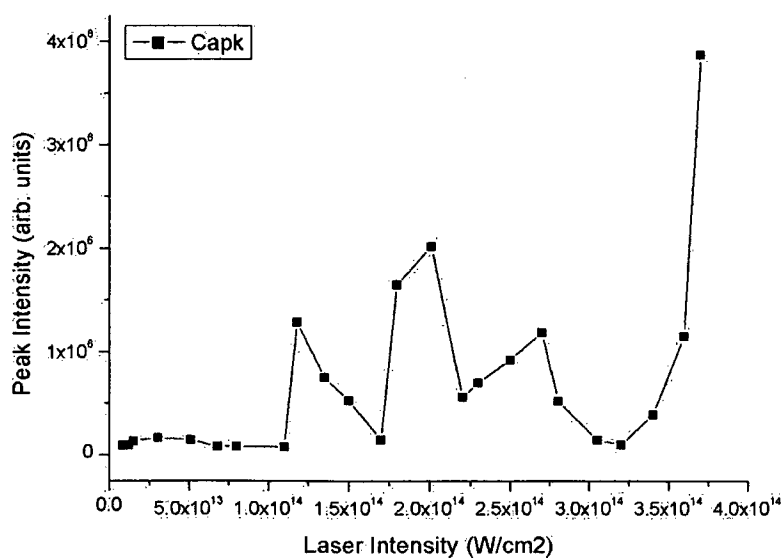


**Figure 43:** Intensity of Ca ion peak signal of bone sample at various laser power densities with  $\lambda=800\text{nm}$ , 30fs ablation.

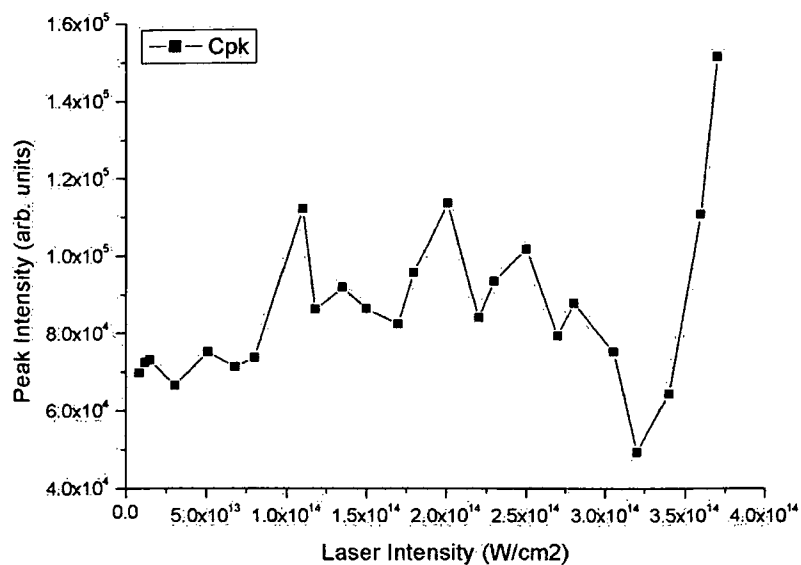


**Figure 44:** Intensity of C ion peak signal of bone sample at various laser power densities with  $\lambda=800\text{nm}$ , 30fs ablation.

It is observed that the intensity dependence is the same for individual peaks. At low laser power densities the signals increase slowly. The signals increase drastically when power densities above  $3 \times 10^{14} \text{ W/cm}^2$  are reached. At higher laser power densities the signal intensity reaches a maximum. It is observed that the K peak exhibits greater intensity dependence in correspondence to the other examined species.

Comparative studies were carried out on tooth and bone samples under ns irradiation over a range of laser ablation intensities. In Figure 45 the response of three most intense masses under irradiation with 193nm wavelength are compared.

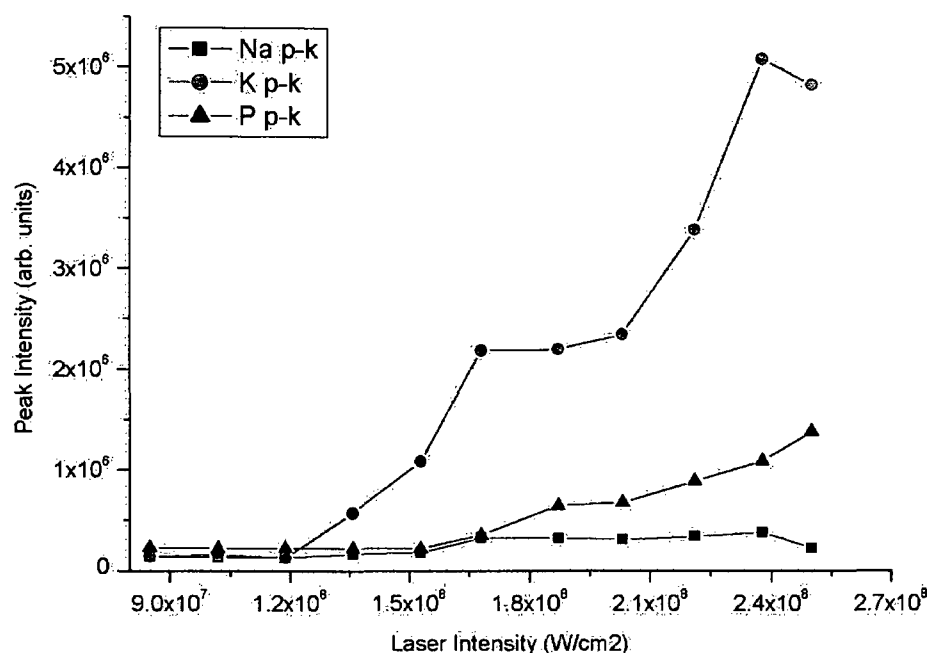


**Figure 45:** Dependence of peak intensity of laser ablated Na, K, and P ions of tooth sample vs. laser intensity at  $\lambda=193\text{nm}$ , pulse duration 30ns.

Accurately was measured the threshold intensity for ablation and was estimated that for 30 ns pulses the ablation threshold for tooth sample was found to be about  $\approx 1.2 \cdot 10^8 \text{ W/cm}^2$ . As can be seen on Figure 45 the effect of increasing of ablation laser intensity leads to overall increase of the ion intensity signal (observed for  $I > 1.5 \cdot 10^8 \text{ W/cm}^2$ ). Furthermore in Figure 45 (as in Figure 42) it is well observed a sharp increase in the K ion peak intensity signal. In contrast to Figure 41, where the signal intensity of Na ion peak was observed to increase suddenly at  $I > 3.4 \cdot 10^{14} \text{ W/cm}^2$ , the behavior in the ns range shows no sharp increase of Na signal over the whole range of laser intensities.

### 3.4 SNMS measurements

Current research comprises femtosecond laser ionization with an ion gun as a bombardment source for the analysis of organic molecules. Particle ejection was achieved using  $9\text{keV}$  accelerated  $\text{Xe}^+$  ions.

Accurate spatial and temporal alignment of the ion gun and laser pulses was critical for achieving maximal signal. The timing between the ion gun and laser pulses was controlled using delay generator (*LeCroy 4222*). Neutral species intersect the laser beam at a distance of  $2\text{mm}$  above the target surface.

First,  $800\text{nm}$  ionization patterns are presented for two types of biological targets (bone and tooth) in order to determine the origin of fragmentation. Next, the  $193\text{nm}$  results are presented to provide additional information about the fragmentation pattern.

*Figure 46a* shows a typical mass spectrum of sputtered ions from bone sample under  $9\text{keV}$   $\text{Xe}^+$  ion bombardment. The spectrum exhibits atomic ions at  $m/z = 23(\text{Na})$ ,  $40(\text{Ca})$  and  $44(^{44}\text{Ca})$  and also some molecular fragments at  $m/z = 56(\text{CaO})$ .

*Figure 46b* shows the  $800\text{nm}$  SNMS mass spectrum of bone samples. The spectrum yields structurally-specific and non-specific fragments. Besides the masses at  $m/z = 23(\text{Na})$ ,  $40(\text{Ca})$ ,  $44(^{44}\text{Ca})$  and  $56(\text{CaO})$  which appear on *Figure 46a*, the mass spectrum on *Figure 46b* shows signals at  $m/z = 20, 47, 49, 60, 82, 96, 103, 113, 120$ .

Multiply charged atomic ion was detected at  $m/z = 20$ , which can be attributed to  $\text{Ca}^{2+}$ . This is indicative of the onset of Coulomb explosion. In the case of femtosecond-induced spectra, multiply charged  $\text{Ca}$  atoms have been observed over a range of intensities under identical detection conditions *Figure 47*.

The phenomenon coulomb explosion is associated with high intensity regimes. At high intensities multiply charged molecular and atomic species are formed due to Coulomb repulsion. The result is explosion of the molecule and formation of stable ions. On *Figure 47* double charged atom of  $\text{Ca}$  is observed even at low intensities. As the intensity was increased,  $\text{Ca}^{2+}$  yield also increased.

- *SIMS/femtosecond laser ionization mass spectra for bone sample.*

The spectra were recorded at  $\lambda=800\text{nm}$ , pulse duration of  $30\text{fs}$  and with typical ionization laser intensities of  $I=2.2 \cdot 10^{14} \text{W/cm}^2$ .

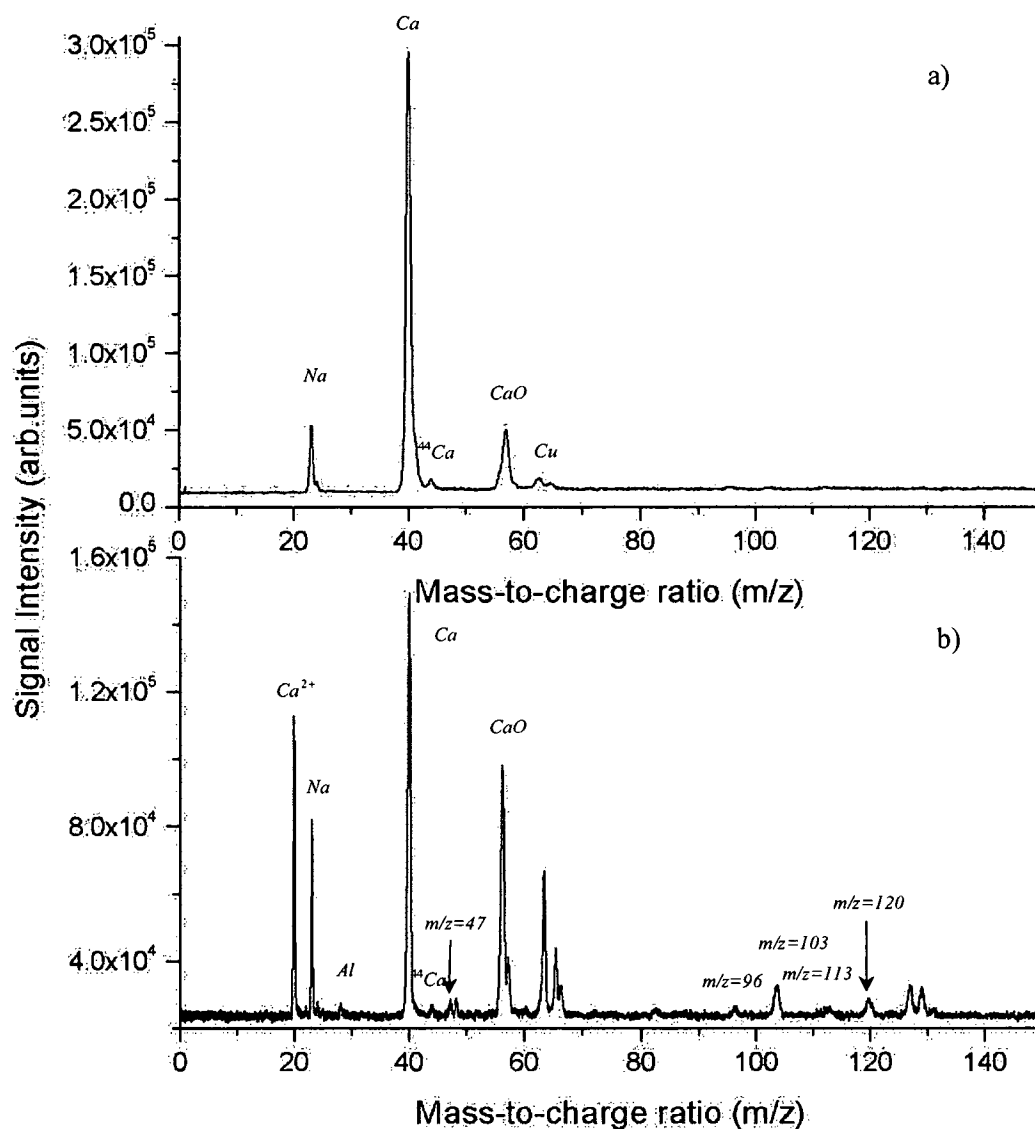


**Figure 46:** A comparison of ToF mass spectra of SIMS and post-ionization mass spectra: a) ToF mass spectrum of ejected particles of bone sample bombarded with 9keV  $\text{Xe}^+$  ions; b) ToF mass spectrum of post-ionized species with femtosecond laser ( $\lambda=800\text{nm}$ , 30fs,  $I=2.2 \cdot 10^{14} \text{W/cm}^2$ ).

With laser intensity of  $> 1.1 \cdot 10^{14} \text{W/cm}^2$  we measured increase in the amount of characteristic ions produced with postionisation over SIMS under identical ion sputtering conditions.

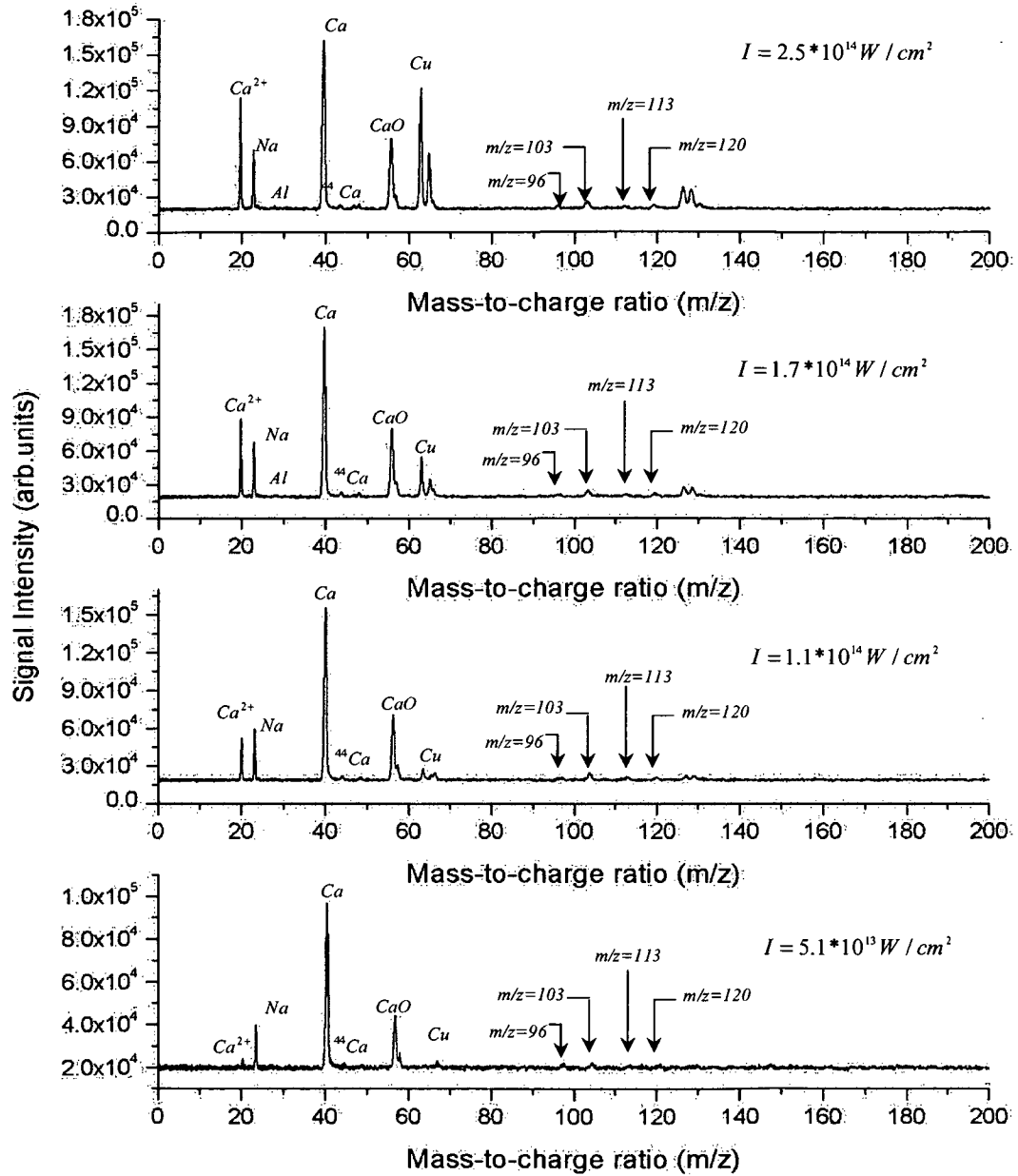


**Figure 47:** ToF mass spectra of bone sample produced by femtosecond post-ionization at  $\lambda=800\text{nm}$ , 30fs pulse duration over a range of post-ionization laser intensities ( $5.1 \times 10^{13} \text{ W/cm}^2 - 2.5 \times 10^{14} \text{ W/cm}^2$ ).

- SIMS/femtosecond laser ionization mass spectra for tooth sample.

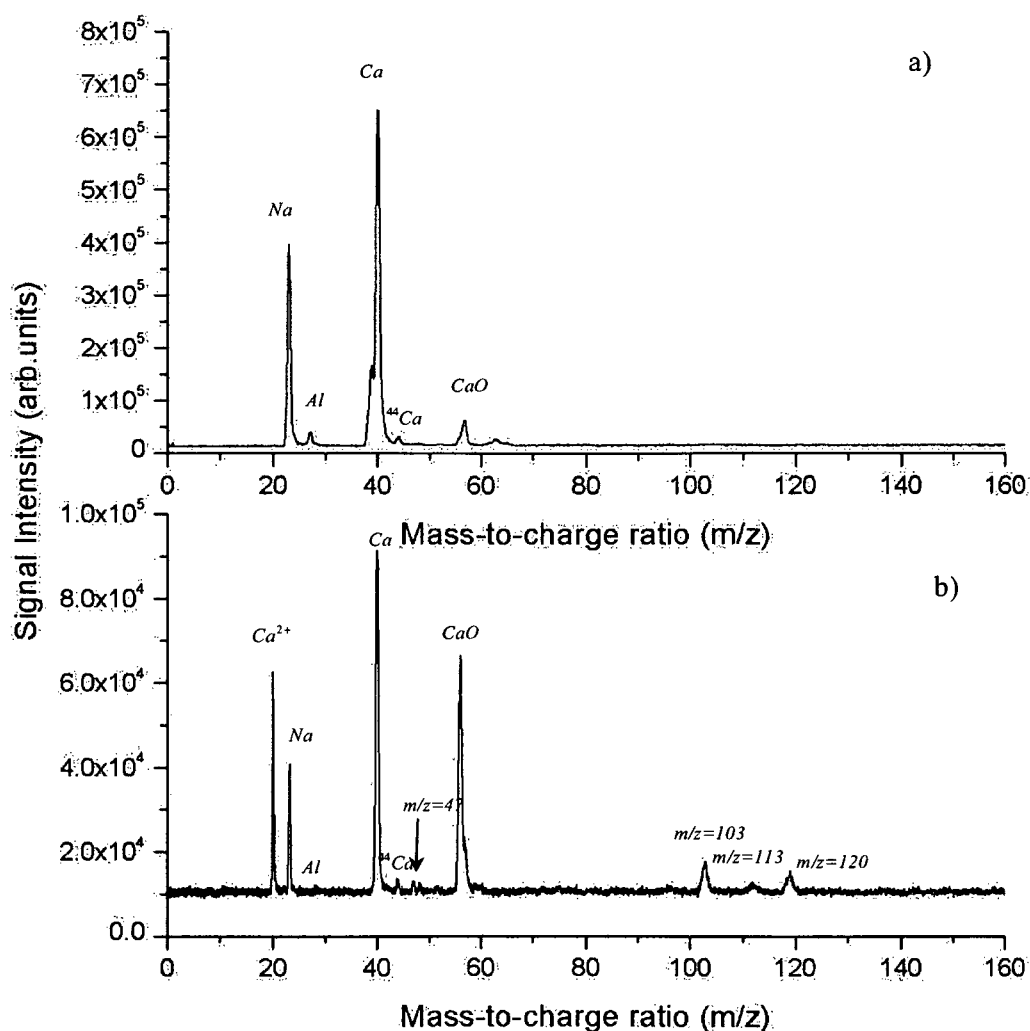


**Figure 48:** A comparison of ToF mass spectra of SIMS and post-ionization mass spectra: a) ToF mass spectrum of ejected species of tooth sample bombarded with 9keV  $\text{Xe}^+$  ions; b) ToF mass spectrum of post-ionized species of tooth sample with femtosecond laser ( $\lambda=800\text{nm}$ , 30fs.).

A comparison of ion yields between postionisation at 800nm and SIMS was made. Comparing the yield of  $\text{Ca}^+$  ions for SIMS to the ion yield for post-ionization we find 5-6 order of magnitude decrease in the signal, and appearance of  $\text{Ca}^{2+}$ . Furthermore there are

no molecular ions detected. The 193nm photoionization mass spectra of tooth and bone samples are shown in Figure 49.

- SIMS/nanosecond laser ionization mass spectra for tooth and bone sample.

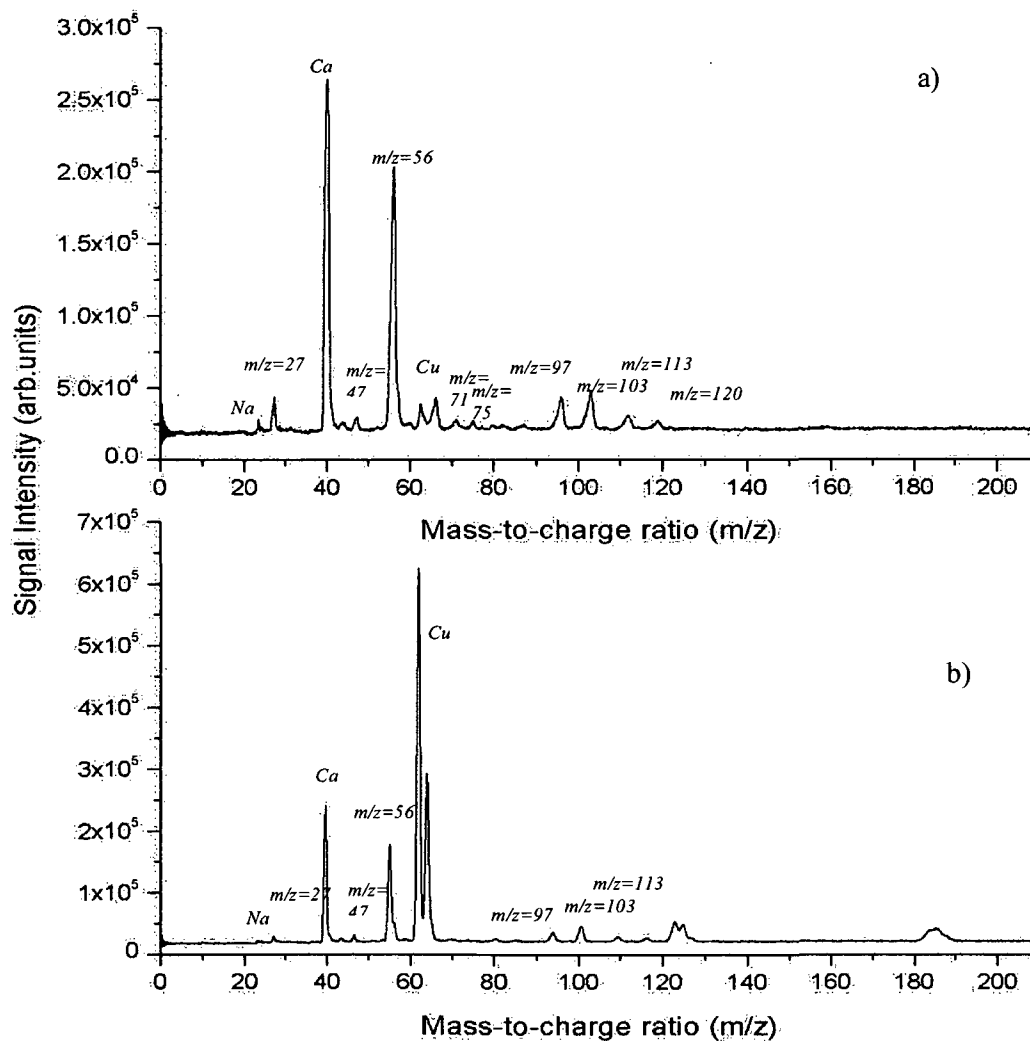


**Figure 49:** A comparison of nanosecond ToF ionization mass spectra of tooth and bone sample: a) ToF mass spectrum of post-ionized species of tooth sample with nanosecond laser at  $\lambda = 193\text{nm}$  and pulse duration of  $\approx 30\text{ns}$ ; b) ToF mass spectrum of post-ionized species of bone sample with nanosecond laser at  $\lambda = 193\text{nm}$  and pulse duration of  $\approx 30\text{ns}$  and  $I = 3.4 \times 10^8 \text{ W/cm}^2$ .



The majority of previous femtosecond laser ionization studies have been carried out on atomic, diatomic or small polyatomic molecules. It was difficult to examine the behavior of more complex molecules in the presence of intensive laser field due to their involatility and thermal lability. Several groups have reported their attempts to make femtosecond photoionization for several amino acids and peptides. Hollingsworth and co-workers have presented preliminary results on femto- and picosecond photoionization of a group of amino acids and chlorophyll – a. In their experiment they have used 50 fs pulses at 750 nm. For volatilisation of intact neutrals a nanosecond  $CO_2$  laser was used. They have obtained characteristic mass spectra for the amino acids glycine (Figure 50) and tryptophan (Figure 51).

The spectrum of glycine molecule exhibit a molecular ion peak at  $m/z=75$ , and at  $m/z=30, 45$  two peaks corresponding to  $H_2NCH_2$  and respectively  $COOH$  fragments. Again they observe cleavage of the C-C bond and formation of a decarboxylated amino acid ion. Furthermore for the aromatic amino acid tryptophan they observe formation of a molecular ion peak at  $m/z=204$  and at  $m/z=130$  the appearance of dehydroindole ion.

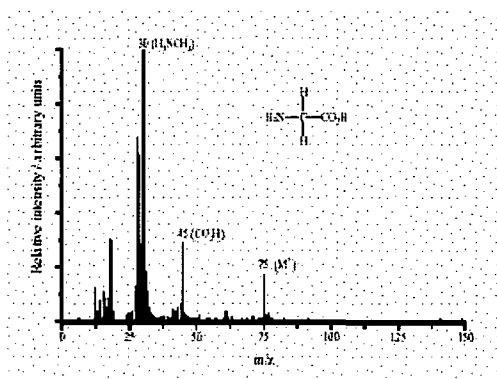


**Figure 50:** Femtosecond photoionization mass spectrum of lysine.

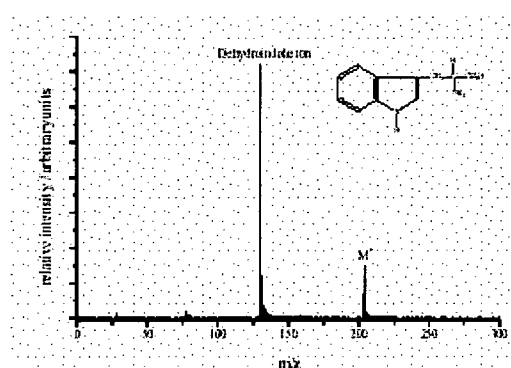


**Figure 51:** Femtosecond photoionization mass spectrum of tryptophan.

Vorsa and co-workers presented fs postionization data for the amino acid alanine at 267nm and 200nm. The fragmentation pattern which they observed in positive SIMS spectrum contain molecular ion at  $m/z=90$ . The postionization spectra show fragment at  $m/z=44$ , due to the loss of the carboxylic group, and little molecular ion.

Another group of N. Winograd has carried out extensive studies of 195, 260 nm femtosecond photoionisation of ion beam desorbed aliphatic and aromatic amino acids.

They observed that no molecular ions were formatted at either wavelength, for any of the amino acids. The proposed mechanism of fragmentation was the  $\alpha$ -cleavage reaction.

In the 195 nm photoionization mass spectra of aliphatic amino acids (glycine, alanine, valine, isoleucine), shows elimination of the carboxyl group. Characteristic is also the absence of the molecular ion.

The photoionization with 260 nm proceeds in a similar manner.

According to the examined femtosecond laser ablation mass spectra in the current thesis a molecular dissociation prior to ionization may occur under intense ablation conditions. The investigations of the mass spectrum of bone sample (Figure 29) have revealed high ion yields of structure specific fragments and the absence of molecular ions.

As a contrast the femtosecond ablation mass spectrum of tooth samples (Figure 31) shows considerably less fragmentation. Significant yields of structure specific fragment ions with masses up to  $m/z=290$  have been obtained.

Exposure to laser intensities above the dissociation threshold triggers molecular fragmentation during the ablation step. Optimum laser ablation intensity is desirable, for ablation of intact neutrals with minimal internal excitation that may lead to dissociation, prior to direct ionization. In our experiments it was suitable to work with laser intensities in the order of  $1.35 \cdot 10^{14} \text{ W/cm}^2$  to obtain optimal signal detection without the onset of considerable fragmentation.

Comparative studies using femtosecond pulses and nanosecond pulses have been carried out on laser ablation of hard biological tissue. As a general tendency in nanosecond ablation and in SIMS experiments the detection of higher mass molecular species is negligible in correspondence to femtosecond laser ablation spectra.

The understanding of interaction of intense laser pulses with polyatomic molecules is at a preliminary stage. In the ionization experiments performed in the current research the polyatomic molecules irradiated with  $\approx 30 \text{ fs}$  laser pulses, at wavelength 800nm do not exhibit an extensive fragmentation, and produce multiply charged ions. This behavior was observed by Ledingham and Hankin for deuterated benzene, carbon disulfide ( $\text{CS}_2$ ), 1, 3-butadiene, toluene. They observed that for laser intensities in the infrared in the range of  $5 \cdot 10^{13} - 10^{15} \text{ W/cm}^2$  the fragmentation for the above mentioned molecules is small, and multiply charged ions up to 3+ were detected. Low degree of fragmentation was shown also by De Witt and co-workers on aromatic molecules, they did not observed the formation of multiple charged ions since they were working in the lower intensity regime of  $4 \cdot 10^{13} \text{ W/cm}^2$ .

In particular in the intensity range  $10^{14} - 10^{16} \text{ W/cm}^2$  the strength of the generated electric field exceeds the binding molecular fields of the valence electrons. The energy may be channeled into nuclear degrees of freedom. In this regime of field ionization,

dissociation through Coulomb explosion of charged fragments is characteristic. The molecule starts to align with the electric field, elongate, and at optimal bond distance ionize rapidly, leading to Coulomb explosion. Due to the high laser intensity  $10^{14} - 10^{15} \text{ W/cm}^2$  multiple ionization is possible followed by substantial fragmentation. The Coulomb explosion can be described by two step model. The first step proceeds with ionization of the neutral molecule. When the first step is beyond the fragment ions start to mutually repel due to the Coulomb force. The result is loss of additional electrons when the internuclear distance approaches the critical distance  $R_c$  which is about two times larger than equilibrium internuclear distance  $R_e$ .

In order to have intact ionization, two dissociation mechanisms have to be circumvented, one is the absorption-dissociation-ionization (*ADI*), and the other one is absorption-ionization-dissociation (*AID*) mechanism (see § 1.4.1).

The *ADI* process can be overcome by increasing the laser intensity, and intact ionization develops on a time scale that is faster than the neutral dissociation time scale. When the laser pulse length is shorter than the lifetime of the dissociative state can happen that the up-pumping rate may become so high that the ionization level is reached. The rapid ionization will avoid intramolecular energy transfer which can lead to excitation or fragmentation of intermediate states. In the case of femtosecond excitation, the *ADI* is supposed that is suppressed and the ladder climbing mechanism is expected to be dominant as the pulse width decreases. It was observed that many molecules (aromatics) can fragment by *AID* scheme, other molecules like organometalics fragment via *ADI* scheme.

When using high-intensity pulses the process of MPI competes with field ionization. We apply to our conditions the qualitative criterion:

$$\gamma = \left[ \frac{IP}{(1.87 \cdot 10^{-13}) I \lambda^2} \right]^{\frac{1}{2}} \quad (\text{Equation 51})$$

Where *IP* is the ionization potential, *I* is laser power density,  $\lambda$  is wavelength in  $\mu\text{m}$ .

The ionization potentials for several amino acids are shown in *Table 10*.

Amino acid	IP
Gly	8.8
Ala	8.9
Val	8.7
Leu	8.5
Ile	8.7
Phe	8.5
Tyr	8.0
Trp	7.2

**Table 10:** Ionization energies for amino acids.

According to this criterion when  $\gamma \gg 1$ , *MPI* is the governing ionization mechanism. Field ionization occurs when  $\gamma \ll 1$ . For  $\gamma < 0.5$  tunnel ionization is believed to be operating ionization mechanism. In our case the calculation of the Keldysh parameter returns the value of 0.5, which places our experiment on the limit between the regime of tunnel ionization and barrier suppression ionization (*BSI*).

While the Coulomb potential barrier is suppressed below the ground electronic level, the electron is ionized. This is called barrier-suppression ionization. Barrier suppression model has been developed to predict the threshold intensity for onset of complete dissociation. The calculated threshold of  $I_{BS}$  for our experiment is:

$$I_{BS} = \frac{cI_p^4}{128\pi Z^2 e^6} = 4 * 10^9 \frac{I_p^4}{Z^2} = 1.6 * 10^{13} W/cm^2 \quad (\text{Equation 52})$$

where  $Z$  is the charge number of the produced ion.

If we concentrate our attention to the behavior of the *Ca* peak (*Figure 46*, *Figure 47*) at increasing laser intensities, the parent ion intensity decreases and doubly charged *Ca* ions appear. This phenomenon clearly shows the onset of a Coulomb explosion. In our case this process is triggered in the intensity range of  $5 * 10^{13} W/cm^2$  which is in correspondence with the aforementioned studies of Ledingham and Hankin. It was suggested that the formation of singly ionized species under intense laser radiation can occur at the leading edge of the pulse, for a Gaussian profile. The formation of multiply ionized species will start along the pulse profile.

For large molecules the mechanism of ionization has been discussed by De Witt and co-workers. It was indicated that for larger molecules structure based-tunneling ionization is dominant at intensity range of  $1 * 10^{13} W/cm^2$ . The near infra-red ionization process led to observation of intact molecular ions for all the studied molecules (benzene, naphthalene, phenanthrene and anthracene). Also they observed that the dissociation yield was increasing for increasing number of atoms. Moreover the mechanism of

coupling changed from multiphoton to field ionization as the spatial size of the molecule increases.

The bypass of a strong molecular fragmentation, leading to enhanced parent ion formation using femtosecond pulses have been observed for various types of molecules, however this fragmentation pathway is not always evident. Sometimes it is possible the detection of the parent ion to be absent and the spectra exhibits extensive lower mass fragmentation. Markevitch and co-workers [mark 01] have observed an exponential increase in the dissociation rate with increasing number of atoms; this was attributed to lower bond dissociation energies and higher rate of energy transfer. In our observations for femtosecond ionization we were not able to detect molecular ion formation for either of the biological probes. The spectra exhibit a low mass distribution of atomic or molecular ions. The reason for the aforementioned observations can be the particle ejection mechanism. Current ionization experiments were performed with ion bombardment, which can lead to heating. This can be overcome with laser ablation versus femtosecond ionization

Recently Smith and co-workers, performed experiments on a series of aromatic molecules (toluene, benzene, and naphthalene) in the intensity range of ( $10^{13} - 10^{14} \text{ W/cm}^2$ ) at two wavelengths  $375\text{nm}$  and  $750\text{nm}$ . They observed that the total saturation of the signal was achieved when the laser intensity reaches  $10^{14} \text{ W/cm}^2$ .

In the laser ablation experiments the results obtained for several organic and inorganic compounds (C, Ca, K, Na), see Figure 41, 42, 43, 44; shows that for all of the examined compounds the obtained laser intensity dependences at wavelength  $800\text{nm}$  shows a saturation for intensities higher than  $3.5 \cdot 10^{14} \text{ W/cm}^2$ . The three sets of data for inorganic species on Figure 41, 42, and 43 show very similar ionization efficiency. The measured threshold intensity in the order of  $3 \cdot 10^{13} \text{ W/cm}^2$  observed for femtosecond laser ablation is less comparing to the observation of other groups working with organic molecules; this implies the efficiency of femtosecond laser ablation process.

A parallel comparison of the  $193\text{nm}$  photoionization mass spectra (see Figure 49) obtained for tooth and bone sample to the photoionization mass spectra obtained at  $800\text{nm}$  (see Figure 46 and 48) shows a similarity in the fragmentation patterns for both wavelengths, however absence of multiply charged species shows a clear indication that at  $193\text{nm}$  no field ionization is taking place, moreover can be concluded that wavelength appear to be important in the case of organic molecules. Referring to the specific wavelength regime two types of excitations can be evoked.

#### 1. The case of UV excitation.

This type of excitation is characterized with electronic excitation which the laser evokes. Through this, the equilibrium between the internuclear electrostatic forces and the electronic cloud that keeps together the nuclei are destroyed. The resulting processes can be classified in two ways: fast, direct dissociation, or slow indirect predissociation.

Generally in UV excitation a single photon brings enough energy into the system to excite a valence electron, thus triggering photodissociation.

When the molecule is irradiated with very strong fields, is possible the absorption of several photons simultaneously, which number exceeds the minimum required for the fragmentation process to develop. This phenomenon is called above threshold ionization (*ATI*). The redistribution of the excitation energy in the molecule results in several subsequent possibilities for fragmentation. The laser control can be expressed by "softening" or "hardening" of the chemical bonds by influencing the internal force field of the molecule.

## 2. The case of *IR* excitation.

In the case of *IR* excitation the energy of a single *IR* photon is not enough to break a molecular bond. It can induce ro-vibrational excitation. The dissociation of the molecule can happen after absorption of several individual photons. Whether the molecule will dissociate after the absorption of several photons depends on whether the molecule can experience the necessary field intensity without ionization. The following interpretative scheme can be described. Supposing a presence of low frequency, quasistatic electromagnetic field, the ground state will experience large distortions due to radiatively induced interaction with the excited states. These will possess suppressing of its potential barrier, which leads to prediction of threshold intensity for the onset of a dissociation.

## *Summary*

I believe that the results presented in this thesis are a first promising approach through the better understanding of the interaction mechanism of ultra-short laser pulses with biological material.

However the absence of molecular ions in photoionization experiments has to be further pursued.

Further work is required in order to conclusively identify the operating ionization mechanism.

It would also be very interesting to extend the measurement by influencing the pulse duration. Additional studies can be conducted to investigate the optimum conditions for laser ablation of soft biological tissue.

As it was shown in the current thesis the mass pattern for biological tissue is very complex and complicated. However, it was well established that femtosecond ablation works well for ablation of complex biological molecule systems. It was possible with the presented method to introduce a simple and nondestructive way for obtaining tooth and bone tissue spectra. This work demonstrates sensitivity of the *ToF* technique and the great potential of the *LA/US-LSNMS* method in increasing the information content of biomolecular mass spectra. The obtained experimental results can be extended by exploring the dynamics of the ablation process by means of femtosecond photoionization versus femtosecond laser ablation. The necessity of establishing of correct and proper laser parameters in the process of laser ablation will be of a great importance for further application of ultra-short radiation in medicine and industry.

Tissue processing with ultra-short (femtosecond) pulses has already become very interesting topic. For example in dentistry ultra-short lasers are used for crack-free processing of enamel. The femtosecond lasers pulses are very well suited for high precision middle ear surgery, due to its low thermal and mechanical stress.

These examples show the rising application of ultra-short pulses in the medicine. Due to the demonstrated high accuracy and reproducibility of the surgical procedures with fs pulses, the potential of using fs laser sources as a low price, conventional tool for a lot of surgery applications have increased. There exists a large market where reliable, compact and economically priced fs systems, for medical use, are distributed.

Experiments are currently underway which incorporate acousto-optic pulse shaping device for generation of amplified shaped pulses with high average power. An acousto-optic wave diffracts individual frequencies in the pulses creating amplitude and phase modulated pulses. This gives the opportunity not only to study the basic laser induced processes in biology, physics and chemistry, but also to be controlled and optimized when ultra-short pulses with specific phase profiles and intensity are generated.

---

## *Abbreviations*

*TOF - time of flight*  
*PRK - phorefractive keratectomy*  
*ELT - excimer laser trabeculotomy*  
*ELANA - laser assisted nonocclusive anastomosis*  
*PDT - photodynamic therapy*  
*BSI - barrier suppression ionization*  
*ADI - absorption-dissociation-ionization*  
*AID - absorption-ionization-dissociation*  
*MPI - multi-photon ionization*  
*CPA - chirp pulse amplification*  
*UHV - ultra high vacuum*  
*US-LSNMS - ultra - short laser secondary neutral mass spectrometry*  
*SIMS - secondary ion mass spectrometry*  
*SNMS - secondary neutral mass spectrometry*  
*MCP - micro-channel-plate assembly*  
*GVD - group velocity dispersion*  
*PEM - pyro-electrical energy measuring device*  
*SPM - self-phase modulation*  
*MDC -mirror-dispersion-controlled*  
*GDD - group-delay-dispersion*  
*KLM - Kerr lens mode-locking*  
*ASE - amplified spontaneous emission*  
*FWHM - full width at a half maximum*  
*SPI - single photon ionization*  
*RMPI - resonant multiphoton ionization*  
*NRMPI - nonresonant multiphoton ionization*  
*MALDI - matrix-assisted laser desorption ionization*  
*ATD - above threshold ionization*



## ***Bibliography***

- vorsa99 V. Vorsa, Teiichiro Kono, Kenneth F. Willey, N. Winograd, *Phys. Chem. B* 103 (1999)
- sun99 S. Sun, V. Vorsa, N. Winograd (1999)
- lock99 N.P. Lockyer, J.C. Vickerman, *Int. Journal of Mass Spectrometry*, 197, (1999)
- dewitt95 M. J. DeWitt, R. Levis, *J. Chem. Phys.* 102, (1995)
- robs02 L. Robson, A. D. Tasker, K. W. D. Ledingham, P. McKenna, T. McCanny, C. Kosmidis, P. Tzallas, D. A. Jaroszynski, D. R. Jones, *Int. J. Mass Spectr.*, 220, (2002)
- radi99 P.P. Radi, P. Beaud, D. Franzke, H.-M. Frey, T. Gerber, B. Mischler, A.-P. Tzannis, *J. Chem. Phys.*, 111, No. 2, (1999)
- korte99 F. Korte, S. Nolte, B. N. Chichkov, T. Bauer, G. Kamlage, T. Wagner, C. Fallnich, H. Welling, *Appl. Phys.*, A69, (1999)
- korte00 F. Korte, S. Adams, A. Egbert, C. Fallnich, A. Ostendorf, S. Nolte, M. Will, J.-P. Ruske, B. N. Chichkov, A. Tunnermann, *Optics express*, 41, Vol. 7, No. 2
- osten03 A. Ostendorf, G. Kamlage, B. N. Chichkov, *Riken Review* No. 50, (2003)
- linde99 D. v. d. Linde, K. Sokolowski-Tinten, *Appl. Surf. Science*, 154-155, (1999)
- hen99 M. Henyk, R. Mitzer, D. Wolfframm, J. Reif, *Appl. Surf. Science* (2000)
- hert01 I. V. Hert, R. Stoian, D. Ashkenasi, A. Rosenfeld, E. B. Campbell, *Riken Review*, No. 32, (2001)
- fan01 C.-H. Fan, J. P. Longtin, *Appl. Optics*, Vol. 40, No. 18, (2001)
- lenz99 M. Lenzner, F. Krausz, J. Kruger, W. Kautek, *Appl. Surf. Science* (2000)
- sun00 J. Sun, J. P. Longtin, P. M. Norris, *Int. Mechanical Engineering Congress and Exposition* (2000)
- schmidt02 V. Schmidt, W. Husinsky, G. Betz, *Appl. Surf. Science*, 7991, (2002)
- hus 96 W. Husinsky, G. Betz, *Thin Solid Films*, 272, (1996)

- hus 93 W. Husinsky, G. Nicolussi, G. Betz, *Beam Interactions with Materials & Atoms*, (1993)
- wurz 90 P. Wurz, W. Husinsky, G. Betz, *Appl. Phys. A52*, (1991)
- lewis00 J. K. Lewis, J. Wei, G. Siuzdak, *Encyclopedia of Analytical Chemistry*, (2000)
- medzih00 K. F. Medzihradszky, J. M. Campbell, M. A. Baldwin, A. M. Falick, P. Juhasz, M. L. Vestal, A. L. Burlingame, *Anal. Chem.*, 72, (2000)
- schiller00 J. Schiller, K. Arnold, R. A. Meyers, *Encyclopedia of Analytical Chemistry* (2000)
- sarver00 A. Sarver, N. K. Scheffler, M. D. Shetlar, B. W. Gibson, *American for Mass Spectrometry*, (2000)
- counter03 A. E. Countermann, M. S. Thompson, D. E. Clemmer, *Journal of Chemical Education*, Vol. 80, No. 2, (2003)
- aeber 00 R. Aebersold, D. R. Goodlett, *Chem. Rev.* , 101, (2001)
- jia 96 W. J. Jia, K. W. D. Ledingham, C. T. J. Scott, C. Kosmidis, R. P. Singhal, *Rapid Communications in Mass Spectrometry*, Vol. 10, (1996)
- holling97 A. Hollingsworth, R. J. J. Maier, P. R. R. Lagridge-Smith, A. J. Langley, P. F. Tadey, *CLF Annual Report* (1997)
- nik99 D. N. Nikogosyan, H. Goerner, *IEEE J. Of selected topics in Quantum Electronics*, Vol. 5, No. 4, (1999)
- vorsa98 V. Vorsa, K. F. Willey, T. Kono, N. Winograd, *American Institute of Physics* (1998)
- levis99 R. J. Levis, M. J. DeWitt, *J. Phys. Chem. A*, Vol. 103, No. 33 (1999)
- dewitt95 M. J. DeWitt, R. J. Levis, *J. Chem. Phys.*, 102, (1995)
- dewitt98 M. J. DeWitt, R. J. Levis, *J. Chem. Phys.*, Vol. 108, No. 18, (1998)
- dewitt99 M. J. DeWitt, R. J. Levis, *J. Chem. Phys.*, Vol. 110, No.23, (1999)
- leding97 K. W. D. Ledingham, R. P. Singhal, D. J. Smith, T. McCanny, P. Graham, H. S. Kilic, W. X. Peng, S. Lwang, A. J. Langley, P. F. Taday, C. Kosmidis, *CLF Annual Report*, (1997)

- kosmidis98 C. Kosmidis, P. Tzallas, K. W. D. Ledingham, T. McCanny, R. P. Singhal, P. F. Taday, A. J. Langley, CLF Annual Report, (1998)*
- hank99 S. M. Hankin, X. Fang, K. W. D. Ledingham, R. P. Singhal, T. McCanny, L. Robson, A. D. Tasker, C. Kosmidis, P. Tzallas, A. J. Langley, P. F. Taday, E. Divall, CLF Annual Report, (1999)*
- robs99 L. Robson, A. D. Tasker, S. M. Hankin, K. W. D. Ledingham, R. P. Singhal, X. Fang, T. McCanny, A. J. Langley, P. F. Taday, C. Kosmidis, P. Tzallas, CLF Annual Report, (1999)*
- task00 A. D. Tasker, , L. Robson, S. M. Hankin, K. W. D. Ledingham, , R. P. Singhal, X. Fang, T. McCanny, C. Kosmidis, P. Tzallas, A. J. Langley, P. F. Taday, E. Divall, CLF Annual Report, (2000)*
- hank02 S. M. Hankin, P. F. Taday, L. Robson, K. W. D. Ledingham, X. Fang, P. McKenna, T. McCanny, R. P. Singhal, C. Kosmidis, P. Tzallas, D. A. Jaroszynski, D. R. Jones, R. C. Isaac, S. Jamison, Rappid Commun. Mass. Spectrom., (2002)*
- furusawa99 K. Furusawa, K. Takahashi, H. Kumagai, K. Midorikawa, M. Obara, Appl. Phys. A, (1999)*
- vallee01 F. Vallee, C. R. Acad. Sci. Paris, t. 2, (2001)*
- weller99 S.-S. Wellershoff, J. Hohlfeld, J. Guedde, E. Matthias, Appl. Phys. A, 69, (1999)*
- chichkov96 B. N. Chichkov, C. Momma, S. Nolte, F. v. Alvensleben, A. Tuennermann, Appl. Phys. A, 63, (1996)*
- momma97 C. Momma, S. Nolte, B. N. Chichkov, F. v. Alvensleben, A. Tuennermann, Appl. Surf. Science, 109/110, (1997)*
- gamaly02 E. G. Gamaly, A. V. Rode, V. T. Tikhonchuk, B. Luther-Davies, Appl. Surf. Science, (2002)*
- jand96 J. Jandeleit, G. Urbasch, H. D. Hoffmann, H.-G. Treusch, E. W. Kreutz, Appl. Phys. A, 63, (1996)*
- hirayama02 Y. Hirayama, M. Obara, Appl. Surf. Science, (2002)*
- atan01 P. A. Atanasov, N. N. Nedialkov, S. E. Imamova, A. Ruf, H. Huegel, F. Dausinger, P. Berger, Appl. Surf. Science, (2001)*

- semerok99 A. Semerok, C. Chaleard, V. Detalle, J.-L. Lacour, P. Mauchien, P. Meynadier, C. Nouvellon, B. Salle, P. Palianov, M. Perdrix, G. Petite, *Appl. Surf. Science*, 138-139, (1999)
- stoian00 R. Stoian, H. Varel, A. Rosenfeld, D. Ashkenasi, R. Kelly, E. E. B. Cambell, *Appl. Surf. Science*, 165, (2000)
- stoian00 R. Stoian, D. Ashkenasi, A. Rosenfeld, , E. E. B. Cambell, *Physical ReviewB*, Vol. 62, No. 19, (2000)
- lin95 W.-C. Lin, M. Motamedi, A. J. Welch, *Appl. Optics*, Vol. 34, No. 34, (1995)
- ivanov03 B. Ivanov, A. M. Hakimian, G. M. Peavy, R. F. Haglund, *Appl. Surf. Science*, 208-209, (2003)
- serb02 J. Serbin, T. Bauer, C. Fallnich, A. Kasenbacher, W. H. Arnold, *Appl. Surf. Science*, 8101, (2002)
- krueg99 J. Krueger, W. Kautek, H. Newesly, *Appl. Phys. A*, 69, (1999)
- fisch97 J. P. Fischer, T. Juhasz, J. F. Bille, *Appl. Phys. A*, 64, (1997)
- courrol03 L. C. Courrol, D. M. Zezell, R. E. Samad, L. Gomes, *Journal of Luminiscence*, 102-103, (2003)
- willms96 L. Willms, A. Herschel, M. H. Niemz, T. Pioch, *Lasers in Medical Science*, (1996)
- mark01 A. N. Markevitch, N. P. Moore, R. J. Levis, *Chem. Phys.*, (2001)
- rode02 A. V. Rode, E. Gamaly, and B. Luther-Davis, B.T. Taylor, J. Dawes, A. Chan, R.M. Lowe, P. Hannaford, *J. of Appl. Physics*, 92, No. 4, (2002)
- lubat02 Holger Lubatschowski, Alexander Heisterkamp, Fabian Will Ajo I. Singh, Jesper Serbin, Andreas Ostendorf, Omid Kermani, Ralf Heerman, Herbert Welling, Wolfgang Ertmer, *RIKEN Rev.*, No. 50, (2003)
- rudolph99 P. Rudolph, J. Bonse, J. Kruger, W. Kautek, *J. Appl. Phys. A* 69, (1999)
- brummel94 C.L. Brummel, K.F. Willey, J.C. Vickerman, N. Winograd, *Int. J. of Mass Spectrometry and Ion Processes*, 143, (1995)
- ren03 Haizhen Ren, Ri Ma, Jianxin Chen, Xia Li, Hong Yang, Qihuang Gong, *J. of Physics B*, 36, (2003)
- lenzner97 M. Lenzner, J. Kruger, S. Sartania, Z. Cheng, Ch. Spielmann, G. Mourou, W. Kautek, F. Krausz, *Phys. Review Letters*, 80, No. 18, (1998)

*lang96 B.Lang, A.Vierheilig, E.Wiedenmann, H.Buchenau, G.Gerber, Z.Phys.D 40, (1997)*

*guaglia02 L.Guaglia, M.Brewczyk, C.Cornaggia, Phys.Rev.,65, (2002)*

*scrinzi98 Armin Scrinzi, Michael Geissler, Thomas Brabec, Phys.Rev.Letters, 83, No.4, (1998)*

*hishikawa98 Akiyoshi Hishikawa, Atsushi Iwamae, Kennosuke Hoshina, Mitsuhiko Kono, Kaoru Yamanouchi, Chem.Pys.Letters, 282, (1998)*

*ganichev96 S.D.Ganichev, I.N.Yassievich, W.Prettl, Semicond.Sci.Technol., 11, (1996)*

---

## *Acknowledgments*

This thesis was realized at the Institute for General Physics, of the Technical University of Vienna.

First of all I would like to thank my supervisor a. o. Prof. Dr Wolfgang Husinsky for giving me enough guidance and support during the last three and a half years, for everything I have learned and achieved, and for the many fruitful discussions, especially during writing of my thesis.

Special thanks go to my colleagues for their help with the laser system and many helpful suggestions, discussions and friendly working atmosphere.

Furthermore I would like to thank to all my colleagues in the electronic laboratory and especially to Paul Berlinger, for helping me to solve all electronically problems arising during the research.

To my colleagues from the mechanical workshop I am thankful for their assistance at all times.

I would like to acknowledge the financial support of the Austrian Science Foundation FWF.

Finally, I would also like to thank my family, whose encouragement, moral support and endless love helped me get through the difficult times. To my husband I am especially thankful for his infinite patience and support which helped me to complete this work.

## *CURRICULUM VITAE*

1. Name:	Daskalova
2. First names:	Albena Tacheva
3. Date of birth:	27/04/1975
4. Nationality:	Bulgarian
5. Education:	High education
5.1 Secondary school: 1990 - 1993	21 secondary school Sofia, profile chemistry and biology.
5.2 Higher: 1993 - 1998	Master of Science, Physicist Sofia University, "St. Kliment Ohridsky", specialty- "Optics and Spectroscopy".
1998 - 1999	Diploma Thesis, Institute of General Physics, Technical University Vienna Topic: Application and analysis of Femtosecond laser radiation for Laser – post – Ionization – Spectroscopy
1996-1997	The British Council, Sofia
6. Language skills: (mark 1 to 5 for competence*)	
Language	Reading                      Speaking                      Writing
English	5                      5                      5
Russian	5                      5                      5
German	4                      4                      4
*1. low, *5. excellent.	
7. Computer literacy:	Kaleidagrap, Origin, LabView, Matematica
8. Professional experience	Research Associate, department- Physics and Molecular Dynamics, Institute of General Physics, Technical University Vienna.
2000 - ....	

---

9. Publications, Presentations and Posters:

9.1 Presentation:

A. Daskalova, W. Husinsky. "Yield and Energy Distribution of sputtered Ag-Clusters measured with Ultra-short Laser Post-Ionization". (PITSA, 2000, Karlsruhe, Germany).

9.2 Poster:

A. Daskalova, W. Husinsky, G. Betz. "Ablation of biological tissue by femtosecond radiation: emission of ionic and neutral species and application". (COLA, 2001, Tsukuba, Japan)

9.3 Publication:

Bulgarian national newspaper "Duma" number 014, January the 18<sup>th</sup> 2003  
"Lasers, the future of precise surgery"